



A comparative study on transient vibration suppression of magnetic nonlinear vibration absorbers with different arrangements

Muxuan Guo · Lihua Tang · Hongyan Wang · Haipeng Liu · Shiqiao Gao

Received: 13 March 2023 / Accepted: 4 July 2023 / Published online: 24 July 2023
© The Author(s) 2023

Abstract Nonlinear vibration absorbers (NVA) using magnets feature ease of implementation and outstanding tunability and have attracted much interest in vibration suppression in recent years. Through configuration design and optimization, magnetic NVA can exhibit different nonlinear characteristics such as monostability, bistability and tristability. This work performs a comprehensive comparative study on the transient vibration suppression performances of the NVAs with four different magnet arrangements based on the cantilever beam design, including the NVA with two repulsive magnets (2RMNVA), two attractive magnets (2AMNVA), three repulsive magnets (3RMNVA) and three attractive magnets (3AMNVA). Based on the dipole–dipole model of magnets, the dynamic model of the system containing different magnetic NVAs is established for numerical

simulation and the key parameters of each NVA are optimized under different excitation levels. The influence of parameters on different magnetic NVAs is investigated. Based on the optimization configurations, the rate of the energy dissipation from the primary structure by different magnetic NVAs is compared by wavelet transform analysis. The results show that due to the largest oscillations of crossing outmost wells, the optimized 3RMNVA and 3AMNVA are the preferred configurations for magnetic NVA under different excitation levels. Meanwhile, through the verification and comparison with reported designs, the effectiveness of the optimization method and the optimized NVAs in this paper are confirmed. This work provides the approach and guidelines to design the effective NVA to suppress transient vibrations.

M. Guo · L. Tang (✉)
Department of Mechanical and Mechatronics
Engineering, The University of Auckland, 5-7 Grafton
Road, Auckland 1010, New Zealand
e-mail: l.tang@auckland.ac.nz

H. Wang
College of Mechatronic Engineering, Qiqihar University,
Qiqihar 161006, China

H. Liu (✉) · S. Gao
State Key Laboratory of Explosion Science and
Technology, Beijing Institute of Technology,
Beijing 100081, China
e-mail: lhp@bit.edu.cn

Keywords Nonlinear vibration absorber · Magnet arrangement · Vibration suppression · Transient vibration

1 Introduction

In many scenarios, vibrations have the negative impact on the reliability of the building structures and the performance of mechanical systems. To suppress vibrations, various strategies and devices have been

explored in the literature. Vibration absorbers are one of the most common approaches for vibration suppression, which can be generally categorized into linear vibration absorbers (LVAs) and nonlinear vibration absorbers (NVAs). To ensure that the energy of the primary structure can be transferred to and absorbed by the LVA, the natural frequency of the LVA need to be tuned to the vicinity of the external excitation frequency [1–3]. However, in practical engineering, the external excitation frequency often varies and deviates from the initially tuned frequency, and the performance of the LVA deteriorates. Compared with LVA, NVA does not possess a specific natural frequency, providing a wider vibration suppression bandwidth [4–6].

Nonlinear energy sink (NES) [7–9] is one representative NVA, which can realize targeted energy transfer (TET) to transfer the energy from the primary structure to the NES unidirectionally and irreversibly. A NES usually comprises a mass, a linear viscous damper, and a nonlinear spring with zero linear stiffness and strong nonlinear stiffness. To realize such a nonlinearity of NES, a variety of methods have been attempted. Silva et al. [10] connected a circuit composed of a negative capacitance shunt and a cubic nonlinear capacitance realized by an operational amplifier in series to a piezoelectric cantilever beam to establish a piezoelectric NES. Experimental and simulation results showed that the piezoelectric NES could achieve vibration attenuation in a wide frequency range. Yao et al. [11] used the buckled beam to realize the bistable stiffness in the horizontal and vertical directions to establish the bistable NES and applied it to a rotor system. Their experiment and simulation showed that the vibration suppression effect of the buckled beam bistable NES is strong with a wide bandwidth. Wang et al. [12] used the track structure to form a nonlinear restoring force with peak characteristics and negative stiffness to establish a bistable NES. Their experiment showed that the track bistable NES, as a vibration suppression device, has strong robustness to the change of primary structure properties and excitation energy level. Zou et al. [13] proposed a device consisting of pre-compressed spring, a bearing and a racetrack to customize the nonlinear force of the structure, which can be used to design the energy harvester, vibration isolator and NES. Dekemele et al. [14] demonstrated that the track structure could be used to form a periodically extended

cubic stiffness of the NES, providing a wider vibration suppression bandwidth than the conventional NES. Geng and Ding [15] and Li et al. [16] used two inclined linear springs to establish NES with cubic stiffness through geometric relationship, and added piecewise linear stiffness and vibro-impact to NES respectively, so that the established NES has good vibration suppression efficiency. Pennisi [17] investigated a vibro-impact NES coupled to a linear oscillator to prove its dynamic behavior including targeted energy transfer. Gourc et al. [18] also embedded a vibro-impact NES to the lathe tool to achieve a significant amplitude reduction by successive resonance capture.

In addition to the aforementioned methods (piezoelectric shunt circuit, buckled beam, track structure, inclined linear spring and vibro-impact), recently, magnetic force was introduced in the design of NES due to its ease of implementation and adjustment. AL-Shudeifat [19] used two pairs of aligned asymmetric permanent magnet to form an asymmetric NES force to enhance the shock mitigation performance. Fang et al. [20] used three attractive magnets and a cantilever beam to establish a bistable NES. Experimental results demonstrated that the TET efficiency of this bistable NES is high and robust under a wide range of impacts. Chen et al. [21] used four pairs of repulsive magnets to form a non-contact and smooth bistable restoring force of NES to achieve strong vibration suppression performance. Zhang et al. [22] used a fixed–fixed composite beam with two piezoelectric bimorphs and a pair of repulsive magnets to form a NES to realize both effective vibration suppression and broadband electrical output for energy harvesting. Rezaei et al. [23–25] used a piezoelectric cantilever beam to establish a bistable vibration absorber with two repulsive magnets and a tristable vibration absorber with three repulsive magnets. The simulation results showed that the established vibration absorbers can effectively suppress vibration and harvest energy. Fang et al. [26] improved the models of Rezaei et al. [23–25] by changing the fixed magnet to a tip magnet attached to a piezoelectric cantilever beam, resulting in a tuned NES with better vibration suppression performance as compared to typical bistable NES under small excitations. Benacchio et al. [27] proposed an NVA with seven ring magnets, which can be tuned as a nonlinear tuned vibration absorber (NLTVA), NES or bistable absorber through the adjustment of magnet

distances. The model for the absorber has been derived through a multipole expansion of the magnetic field and verified by experiment. Chen et al. [28] used triple cylindrical permanent magnets and an acrylic tube to establish a novel Triple-magnet Magnetic Suspension Dynamic Vibration Absorber (TMSDVA) to address the issues of existing NESs such as complex structure, high cost and difficulty in miniaturization. The simulation and experimental results showed that TMSDVA can effectively accomplish targeted energy transfer and energy dissipation to reduce the primary structure vibration.

Though a few attempts have been made to achieve effective vibration suppression using magnetic NVA, currently, there is still a lack of comparative study on the transient vibration suppression performances of NVAs with different magnet arrangements based on the cantilever beam design. This paper aims to compare the transient vibration suppression performances of four configurations of magnetic NVAs under different excitation levels. It is worth noting that, though some references termed an oscillator (such as a cantilever beam) with magnet(s) as NES, there is still no universal definition for it [23–26]. Therefore, these absorbers are collectively referred to as magnetic NVA throughout this paper. In Sect. 2, the mechanical model of the system is established, and the magnetic force models of different magnetic NVAs are derived based on the dipole–dipole model. In Sect. 3, the key parameters of different magnetic NVAs under three excitation levels are optimized through exhaustion method and their influences are analyzed. With the optimized parameters, the transient vibration suppression performances of different magnetic NVAs are compared. In Sect. 4, the exhaustion method is applied to the reported designs to verify its effectiveness. Meanwhile, the reported designs are attached to the primary structure in this paper and optimized. Through comparison, the effectiveness of the optimized NVA in this paper are confirmed. Discussion on the performances of the optimized magnetic NVAs and design guideline of magnetic NVAs under different excitation levels are provided in Sect. 5. Conclusive remarks are provided in Sect. 6.

2 Mathematical model

2.1 NVAs with different magnet arrangements

The concerned system concludes a primary structure and a magnetic NVA, as shown in Fig. 1. The primary structure consists of a block with two supporting steel plates. The NVA is supported by the block of the primary structure, comprising a cantilever beam with a tip magnet. The tip magnet on the absorber beam interacts with the external fixed magnet(s), making the beam subject to nonlinear restoring force. By adjusting the stiffness of the absorber beam and the distance(s) between magnets, the nonlinear force subjected to NVA can be adjusted, resulting in different vibration suppression phenomena.

The NVAs with different magnet arrangements are shown in Fig. 2. The first type of NVA with an external magnet that repels the tip magnet of the absorber beam is termed two repulsive magnets NVA (2RMNVA); the second type of NVA with an external magnet that attracts the tip magnet of the absorber beam is termed two attractive magnets NVA (2AMNVA); Similarly, the third and fourth types of NVAs with two external magnets that repel and attract the tip magnet of the absorber beam are termed 3RMNVA and 3AMNVA, respectively. In Fig. 2, L is the distance from the clamped end of the absorber beam to the center of tip magnet, D_m is the diameter of the magnet, a is the length of the magnet, d_x is the horizontal magnet separation distance, and d_y is the half value of vertical magnet separation distance. It is worth noting that the circular tip magnet on the absorber beam is the same as the external magnet(s).

2.2 Dynamic model

The system composed of the NVA and primary structure can be simplified into a two degree of freedom (2DOF) system, as shown in Fig. 3. The governing equations for such a system are:

$$\begin{cases} m_p \ddot{y}_p + c_p \dot{y}_p + k_p y_p - c_a \dot{y}_a - k_a y_a + F_y = 0 \\ m_a (\ddot{y}_a + \ddot{y}_p) + c_a \dot{y}_a + k_a y_a - F_y = 0 \end{cases} \quad (1)$$

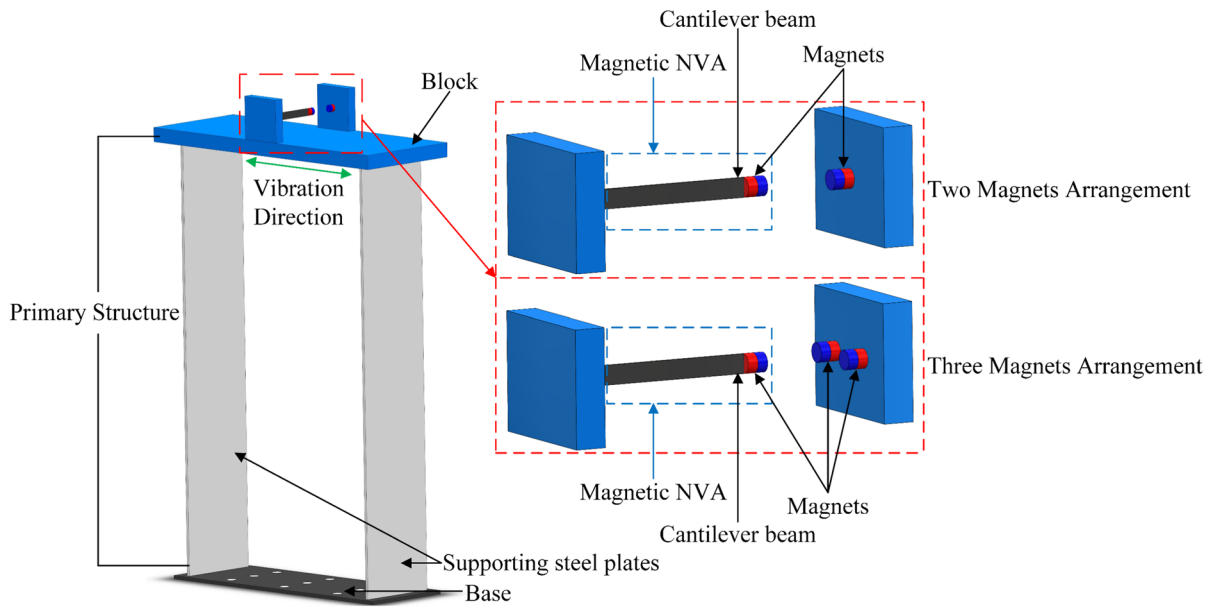
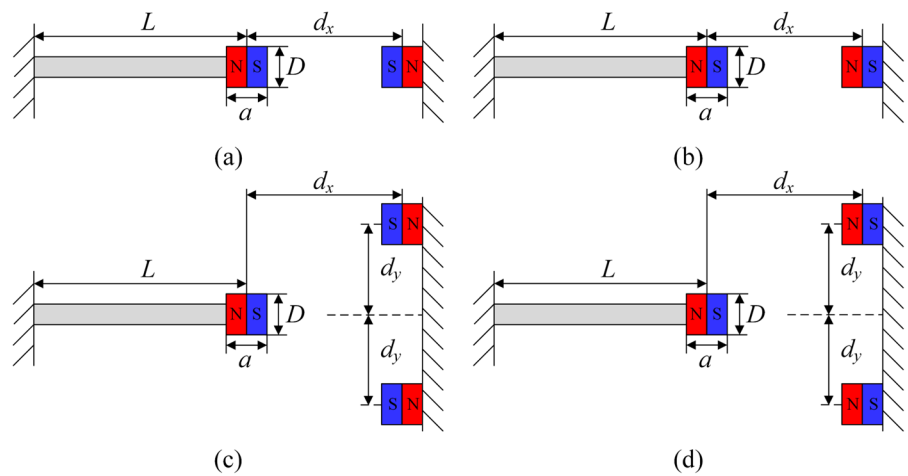


Fig. 1 Conceptual schematic of the primary structure and magnetic NVA

Fig. 2 NVA with different magnet arrangements



where m_p and m_a are the masses of the primary structure and the magnetic NVA, respectively. c_p and c_a are the damping coefficients of the primary structure and the magnetic NVA, respectively. k_p and k_a are the linear stiffnesses of the primary structure and the NVA without magnets, respectively. y_p is the displacement of the primary structure. y_a is the

displacement of the NVA relative to the primary structure. F_y is the nonlinear magnetic force between magnets in the vibration direction.

The vibration suppression behavior of the magnetic NVA can be analyzed through solving the governing equations numerically. Equation (1) is written in the state space form as follows:

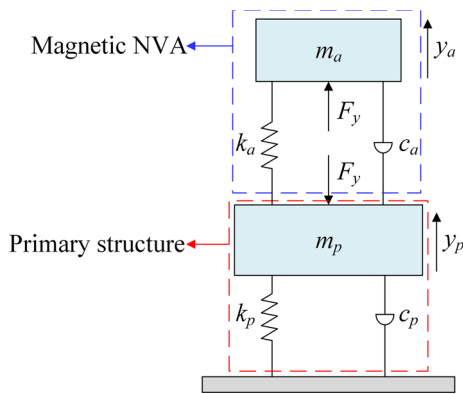


Fig. 3 Lumped parameter 2DOF model of the system with the magnetic NVA

$$\mathbf{q} = \begin{pmatrix} y_p \\ \dot{y}_p \\ y_a \\ \dot{y}_a \end{pmatrix} = \begin{pmatrix} q_1 \\ q_2 \\ q_3 \\ q_4 \end{pmatrix},$$

$$\dot{\mathbf{q}} = \begin{pmatrix} q_2 \\ \frac{1}{m_p}(-F_y - c_p q_2 - k_p q_1 + c_a q_4 + k_a q_3) \\ q_4 \\ \frac{1}{m_a}(F_y - c_a q_4 - k_a q_3) \\ -\frac{1}{m_p}(-F_y - c_p q_2 - k_p q_1 + c_a q_4 + k_a q_3) \end{pmatrix} \quad (2)$$

In the case of transient excitation, the initial conditions are set to be $(q_p \ 0 \ q_a \ 0)$. q_p is the initial displacement of the primary structure, q_a is the initial displacement of the NVA relative to the primary structure. It is worth noting that q_a needs to be set at a stable equilibrium position. However, in the case of bistability, the stable equilibrium position of the NVA is not at $q_a = 0$ and it needs to be adjusted accordingly. In this paper, the ode45 function in MATLAB is used for numerical simulation to obtain the displacements

Table 1 System parameters of the primary structure and the magnetic NVA

Parameter	Value
Mass of the primary structure m_p	0.715 kg
Stiffness of the primary structure k_p	4115.2 N/m
Damping ratio of the primary structure ζ_p	0.011
Mass of the magnetic NVA m_a	0.00651 kg
Damping ratio of the magnetic NVA ζ_a	0.019
Distance from the clamped end of the absorber beam to the center of tip magnet L	0.083 m
Magnets length a	0.010 m
Magnets diameter D_m	0.010 m

and velocities of the primary structure and NVA. The parameters of the primary structure and NVA are obtained from references [29, 30] and shown in Table 1.

2.3 Magnetic force model

The magnetic force models have been studied by many researchers [31–33]. Among these magnetic force models, dipole–dipole model is widely used to calculate the nonlinear interaction force between two magnets, and has more accurate results than magnetizing current model when the magnet separation distance is small [34]. Fang et al. [26] and Zhou et al. [29] regarded the vibration of cantilever beam as small angle vibration to calculate the magnetic force between two piezoelectric beams with tip magnets by using the dipole–dipole model. In this section, the interaction force F_y between the absorber beam with tip magnet and the external fixed magnet(s) is calculated by the dipole–dipole model. The detailed magnetic force model statements and comparison results between the ANSYS and the dipole–dipole model are given in Appendix A.

2.3.1 Magnetic force model for 2RMNVA/2AMNVA

A pair of magnets in 2RMNVA/2AMNVA and primary structure are regarded as magnetic dipoles

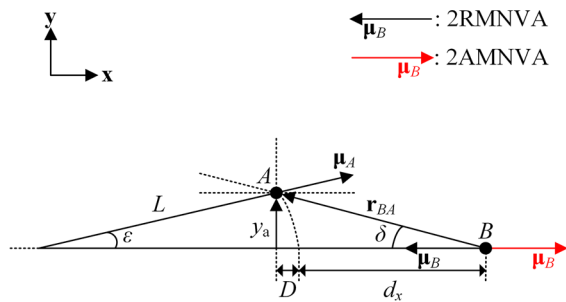


Fig. 4 Geometric configuration of two magnetic dipoles of 2RMNVA/2AMNVA

(A and B). The geometric configuration of the two magnetic dipoles is shown in Fig. 4.

The potential energy of nonlinear interaction between two magnetic dipoles is:

$$U_a = \frac{\mu_0}{4\pi} \nabla \left(\frac{\boldsymbol{\mu}_B \cdot \mathbf{r}_{BA}}{r_{BA}^3} \right) \cdot \boldsymbol{\mu}_A \quad (3)$$

where $\mu_0 = 4\pi \times 10^{-7}$ T·m/A is the vacuum permeability, $\boldsymbol{\mu}_A$ and $\boldsymbol{\mu}_B$ are respectively the magnetic moments of dipoles A and B, and \mathbf{r}_{BA} is the vector pointing from B to A. By taking the gradient of Eq. (3), the force applied by dipole B to dipole A is:

$$\begin{aligned} \mathbf{F} &= -\nabla U_a \\ &= \frac{3\mu_0\mu_A\mu_B}{4\pi r_{BA}^4} \left[\hat{\mathbf{r}}_{BA}(\hat{\boldsymbol{\mu}}_A \cdot \hat{\boldsymbol{\mu}}_B) + \hat{\boldsymbol{\mu}}_B(\hat{\boldsymbol{\mu}}_A \cdot \hat{\mathbf{r}}_{BA}) + \hat{\boldsymbol{\mu}}_A(\hat{\boldsymbol{\mu}}_B \cdot \hat{\mathbf{r}}_{BA}) - \right. \\ &\quad \left. 5\hat{\mathbf{r}}_{BA}(\hat{\boldsymbol{\mu}}_A \cdot \hat{\mathbf{r}}_{BA})(\hat{\boldsymbol{\mu}}_B \cdot \hat{\mathbf{r}}_{BA}) \right] \end{aligned} \quad (4)$$

where μ_A , μ_B and r_{BA} are respectively the modules of $\boldsymbol{\mu}_A$, $\boldsymbol{\mu}_B$ and \mathbf{r}_{BA} , and $\hat{\boldsymbol{\mu}}_A$, $\hat{\boldsymbol{\mu}}_B$ and $\hat{\mathbf{r}}_{BA}$ are respectively the unit vectors of $\boldsymbol{\mu}_A$, $\boldsymbol{\mu}_B$ and \mathbf{r}_{BA} as follows:

$$\mu_A = \mu_B = MV \quad (5)$$

$$r_{BA} = \sqrt{(d_x + D)^2 + y_a^2} \quad (6)$$

where M is the vector sum of all microscopic magnetic moments within the ferromagnetic material, V is the volume of magnet, and D is the change of the y -direction distance between the two magnetic dipoles. The formula for M is as follows:

$$M = B_r / \mu_0 \quad (7)$$

where $B_r = 1.26$ T is the residual flux density. Set the angle between $\boldsymbol{\mu}_A$ and y -direction to be ε and the angle between $\boldsymbol{\mu}_B$ and \mathbf{r}_{BA} to be δ , we have:

$$\sin \varepsilon = y_a / L \quad (8)$$

$$\tan \delta = y_a / (d_x + D) \quad (9)$$

$$D = L(1 - \cos \varepsilon) \quad (10)$$

From the geometric relationship (Fig. 4), the expressions of F_y of 2RMNVA and 2AMNVA are respectively:

$$\begin{aligned} F_y &= \mathbf{F} \cdot \mathbf{y} = \frac{3\mu_0\mu_A\mu_B}{4\pi r_{BA}^4} \\ &\quad [-\cos \varepsilon \sin \delta + \cos \delta \sin \varepsilon + 5 \cos(\delta + \varepsilon) \cos \delta \sin \delta] \end{aligned} \quad (11)$$

$$\begin{aligned} F_y &= \mathbf{F} \cdot \mathbf{y} = \frac{3\mu_0\mu_A\mu_B}{4\pi r_{BA}^4} \\ &\quad [\cos \varepsilon \sin \delta - \cos \delta \sin \varepsilon - 5 \cos(\delta + \varepsilon) \cos \delta \sin \delta] \end{aligned} \quad (12)$$

where \mathbf{y} is the unit vector in the y -direction.

Figure 5 plots the magnetic forces and potential energies of 2RMNVA and 2AMNVA at different horizontal magnet distance d_x . As can be seen from Fig. 5a and b, with the increase of d_x , the amplitude of magnetic force decreases, and the 2RMNVA transitions from bistable to monostable. Also, from Fig. 5c and d, we can see that with the increase of d_x , the amplitude of magnetic force decreases and 2AMNVA remains monostable all the time due to the attraction of the two magnets.

2.3.2 Magnetic force model for 3RMNVA/3AMNVA

Three magnets in 3RMNVA/3AMNVA and primary structure are regarded as magnetic dipoles (A, B, and C). The geometric configuration of the three magnetic dipoles is shown in Fig. 6.

The force applied by dipole B and dipole C to dipole A is:

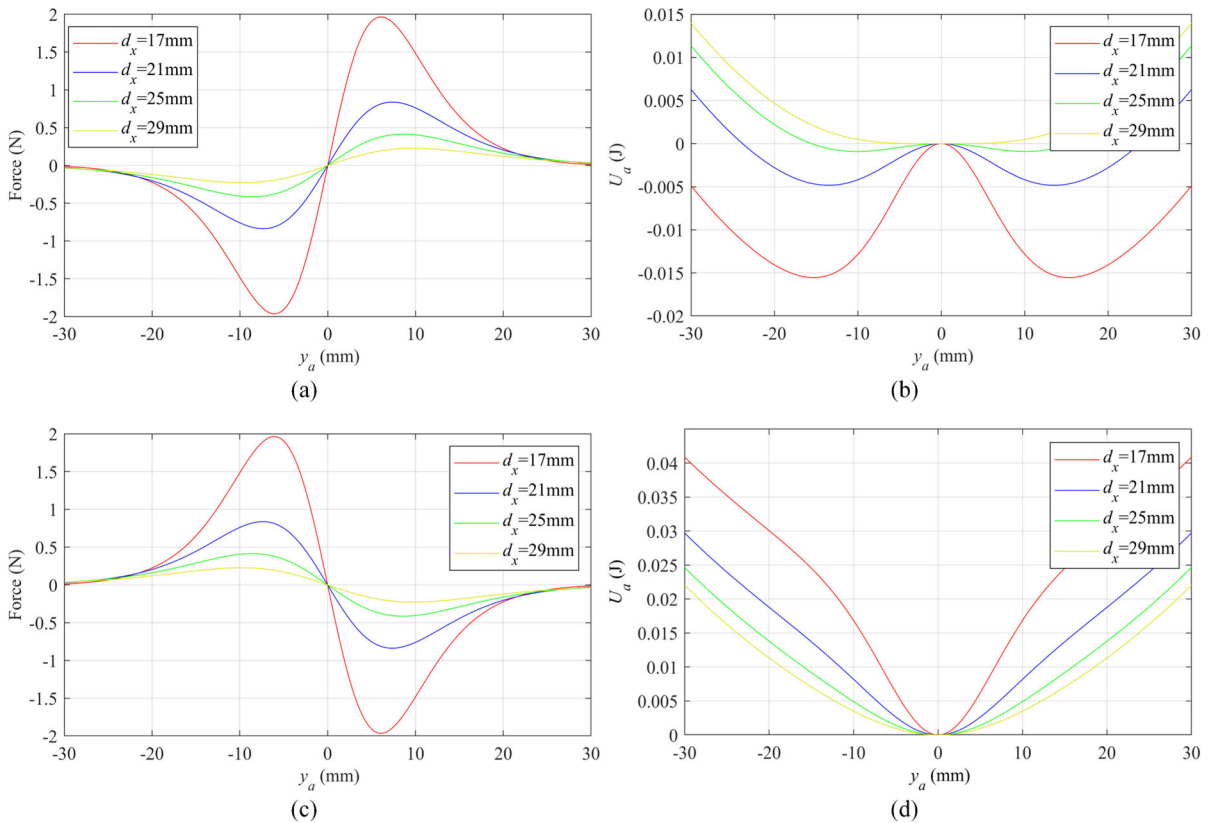


Fig. 5 **a** magnetic force and **b** potential energy of 2RMNVA ($k_a = 40$ N/m), and **c** magnetic force and **d** potential energy of 2AMNVA ($k_a = 40$ N/m) for different d_x

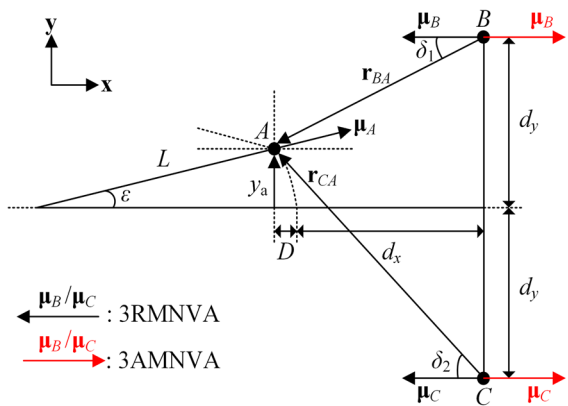


Fig. 6 Geometric configuration of three magnetic dipoles of 3RMNVA/3AMNVA

$$\begin{aligned}
 \mathbf{F} = -\nabla U_a = & \frac{3\mu_0\mu_A\mu_B}{4\pi r_{BA}^4} \left[\hat{\mathbf{r}}_{BA}(\hat{\mu}_A \cdot \hat{\mu}_B) + \hat{\mu}_B(\hat{\mu}_A \cdot \hat{\mathbf{r}}_{BA}) + \hat{\mu}_A(\hat{\mu}_B \cdot \hat{\mathbf{r}}_{BA}) - \right. \\
 & \left. 5\hat{\mathbf{r}}_{BA}(\hat{\mu}_A \cdot \hat{\mathbf{r}}_{BA})(\hat{\mu}_B \cdot \hat{\mathbf{r}}_{BA}) \right] \\
 & + \frac{3\mu_0\mu_A\mu_C}{4\pi r_{CA}^4} \left[\hat{\mathbf{r}}_{CA}(\hat{\mu}_A \cdot \hat{\mu}_C) + \hat{\mu}_C(\hat{\mu}_A \cdot \hat{\mathbf{r}}_{CA}) + \hat{\mu}_A(\hat{\mu}_C \cdot \hat{\mathbf{r}}_{CA}) - \right. \\
 & \left. 5\hat{\mathbf{r}}_{CA}(\hat{\mu}_A \cdot \hat{\mathbf{r}}_{CA})(\hat{\mu}_B \cdot \hat{\mathbf{r}}_{CA}) \right] \quad (13)
 \end{aligned}$$

where μ_C and r_{CA} are respectively the modules of μ_C and r_{CA} , $\hat{\mu}_C$ and $\hat{\mathbf{r}}_{CA}$ are respectively the unit vectors of μ_C and r_{CA} as follows:

$$\mu_C = MV \quad (14)$$

$$r_{BA} = \sqrt{(d_x + D)^2 + (d_y - y_a)^2} \quad (15)$$

$$r_{CA} = \sqrt{(d_x + D)^2 + (d_y + y_a)^2} \quad (16)$$

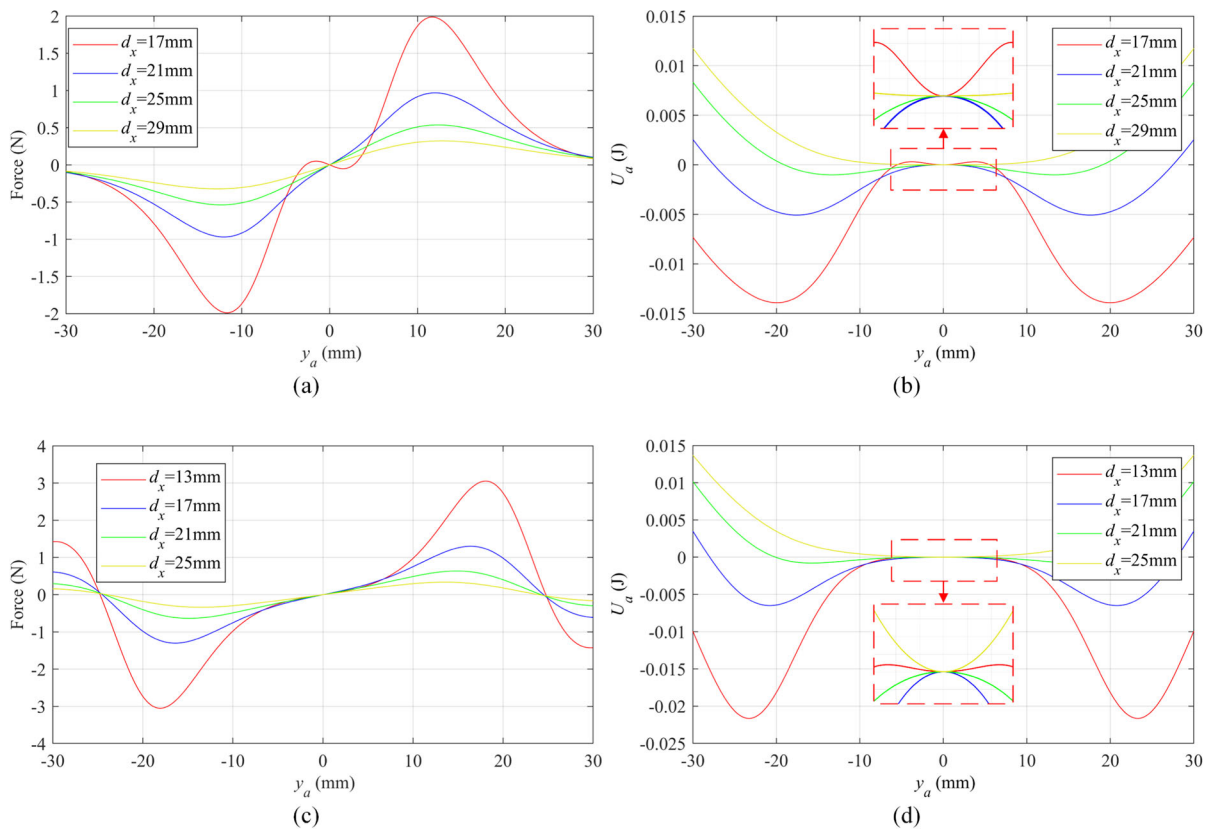


Fig. 7 **a** magnetic force and **b** potential energy of 3RMNVA ($k_a = 40$ N/m, $d_y = 0.007$ m), and **c** magnetic force and **d** potential energy of 3AMNVA ($k_a = 40$ N/m, $d_y = 0.026$ m) for different d_x

Set the angle between μ_B and r_{BA} to be δ_1 and the angle between μ_C and r_{CA} to be δ_2 , we have:

$$\tan \delta_1 = (d_y - y_a) / (d_x + D) \tag{17}$$

$$\tan \delta_2 = (d_y + y_a) / (d_x + D) \tag{18}$$

Based on the geometric relationship (Fig. 6), the expressions of F_y of 3RMNVA and 3AMNVA are respectively:

$$F_y = \mathbf{F} \cdot \mathbf{y} = \frac{3\mu_0\mu_A\mu_B}{4\pi r_{BA}^4} [\cos \varepsilon \sin \delta_1 + \cos \delta_1 \sin \varepsilon - 5 \cos(\delta_1 - \varepsilon) \cos \delta_1 \sin \delta_1] + \frac{3\mu_0\mu_A\mu_C}{4\pi r_{CA}^4} [-\cos \varepsilon \sin \delta_2 + \cos \delta_2 \sin \varepsilon + 5 \cos(\delta_2 + \varepsilon) \cos \delta_2 \sin \delta_2] \tag{19}$$

$$F_y = \mathbf{F} \cdot \mathbf{y} = \frac{3\mu_0\mu_A\mu_B}{4\pi r_{BA}^4} [-\cos \varepsilon \sin \delta_1 - \cos \delta_1 \sin \varepsilon + 5 \cos(\varepsilon - \delta_1) \cos \delta_1 \sin \delta_1] + \frac{3\mu_0\mu_A\mu_C}{4\pi r_{CA}^4} [\cos \varepsilon \sin \delta_2 - \cos \delta_2 \sin \varepsilon - 5 \cos(\delta_2 + \varepsilon) \cos \delta_2 \sin \delta_2] \tag{20}$$

Figure 7 plots the magnetic forces and potential energies of 3RMNVA and 3AMNVA at different horizontal magnet distance d_x . As can be seen from Fig. 7a, with the increase of d_x , the amplitude of magnetic force decreases overall. As noted in Fig. 7c, the amplitude of magnetic force decreases with the increase of d_x . Besides, both 3RMNVA and 3AMNVA transit from tristable to bistable and then to monostable state with the increase of d_x (Fig. 7b, d).

3 Optimization and analysis

In this section, the vibration suppression performances of NVAs with different magnet arrangements and LVA are compared. For fair comparison, the important system parameters are selected for optimization for each arrangement. Since the damping ratio of the system in practice is often difficult to change [35], the horizontal magnet separation distance d_x , the half value of vertical magnet separation distance d_y and the stiffness of the cantilever beam k_a are selected as the optimization parameters. To quantify the vibration suppression performance of the vibration absorbers, the integral of the energy of the primary structure in a certain period of time is taken as the metric [36, 37], and the optimization problem is expressed as follows:

$$\begin{aligned}
 P = \min_{k_a, d_x, (d_y)} \int_0^t E_p(t) dt = \min_{k_a, d_x, (d_y)} & \\
 \int_0^t \left(\frac{1}{2} m_p \dot{y}_p^2(t) + \frac{1}{2} k_p y_p^2(t) \right) dt & \quad (21) \\
 d_{x_min} \leq d_x \leq d_{x_max} & \\
 d_{y_min} \leq d_y \leq d_{y_max} & \\
 k_{a_min} \leq k_a \leq k_{a_max} &
 \end{aligned}$$

A lower value of P indicates the better vibration suppression outcome of the NVA. The upper limit of time is selected to be 6 s to calculate the P value in all the following simulations.

The total energy of the primary structure with the optimized magnetic NVA can also be used to display the performance of magnetic NVAs:

$$E_{Total} = \frac{1}{2} m_p \dot{y}_p^2(t) + \frac{1}{2} k_p y_p^2(t) + \frac{1}{2} m_a \left(\dot{y}_p^2(t) + \dot{y}_a^2(t) \right) + U_a \quad (22)$$

where U_a is the potential energy of magnetic NVAs.

Based on Eq. (21), the optimal parameters of the vibration absorbers are obtained by exhaustion method. The flow chart of the exhaustion method is shown in Fig. 8.

The lower and upper bounds to search optimal configurations of NVAs are shown in Table 2 [26].

3.1 Low-level excitation

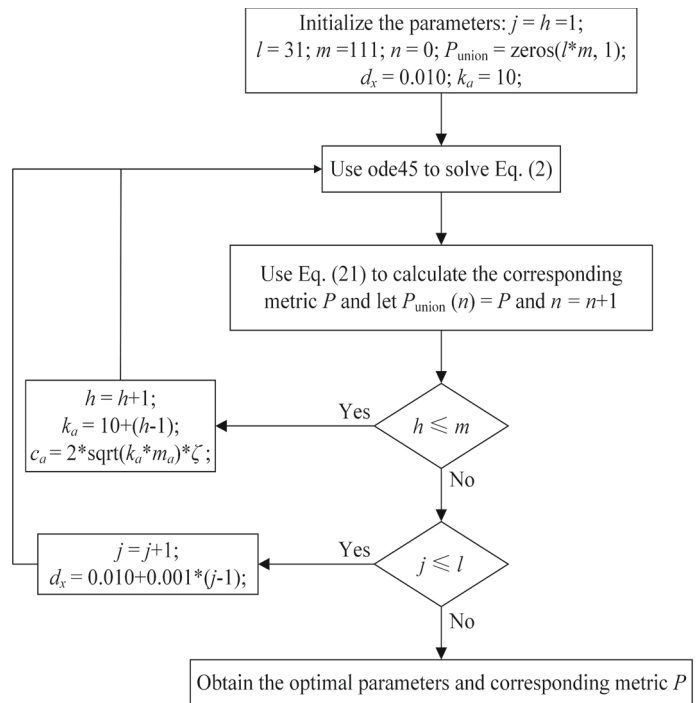
Under the condition of low-level excitation, the initial displacement of the primary structure is set as $q_p = 2$ mm.

The optimization results of 2RMNVA are shown in Fig. 9. When d_x is smaller than 0.021, the vibration suppression performance of 2RMNVA is poor. When d_x is about 0.022, there is a strong vibration suppression area (dark blue area) existing in the interval [107, 111] of k_a and the optimum point is obtained in this area. In general, when d_x is greater than 0.024, with the increase of d_x , the preferred k_a gradually decreases (blue area). Based on the optimization results, the optimal parameters, stable equilibrium and metric of 2RMNVA are $d_x = 0.022$ m, $k_a = 109$ N/m, $q_a = 0.00611$ m and $P = 0.0016$. As shown in Fig. 9b, the optimal 2RMNVA is a weak bistable structure.

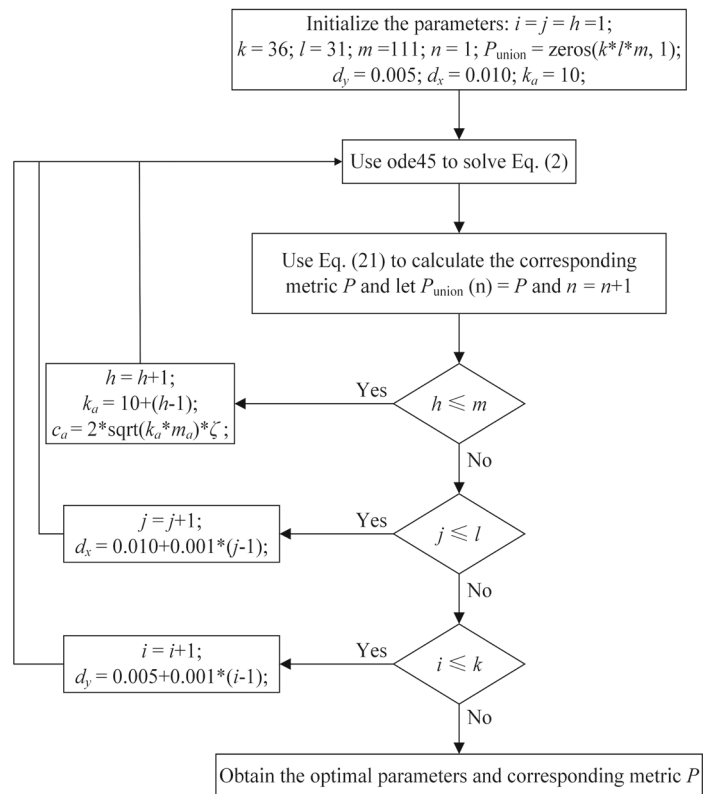
The optimization results of 2AMNVA are shown in Fig. 10. When d_x is smaller than 0.028, the vibration suppression performance of 2AMNVA is poor. When d_x is greater than 0.028, with the increase of d_x , the preferred k_a gradually increases (blue area). Based on the optimization results, the optimal parameters, stable equilibrium and metric of 2AMNVA are $d_x = 0.040$ m, $k_a = 31$ N/m, $q_a = 0$ m and $P = 0.0022$. Because the optimal d_x takes the value at the upper bound, the influence of nonlinear magnetic force is weak. It is shown in Fig. 10b that the restoring force of the optimal 2AMNVA tends to be linear, which indicates that the optimal 2AMNVA is close to a LVA.

The optimization results of 3RMNVA are shown in Fig. 11. The optimal parameters, stable equilibrium and metric of 3RMNVA are $d_x = 0.024$ m, $d_y = 0.007$ m, $k_a = 98$ N/m, $q_a = 0$ m and $P = 0.0017$. The optimal 3RMNVA is a monostable structure (Fig. 11b).

Fig. 8 Exhaustion method flow chart: **a** Magnetic NVA with two magnets and **b** Magnetic NVA with three magnets



(a)



(b)

We can take a close look at the optimization results in different intervals of d_x . It is observed in Fig. 12 that when d_x is in the interval [0.010, 0.020), the strong vibration suppression area (dark blue area) predominantly exists at the high value of d_y . With the increase

of d_y , the preferred k_a gradually increases (Fig. 12a). When d_x is in the interval [0.020, 0.027), the strong vibration suppression area appears at the low value of d_y (e.g., the slice plot in Fig. 12b) and the optimum point is obtained in this domain (Fig. 11a). When d_x is in the interval [0.027, 0.035), with the increase of d_y , the preferred k_a first decreases and then increases gently (Fig. 12c). When d_x is in the interval [0.035, 0.040], with the increase of d_y , the preferred k_a gradually decreases and stabilizes at about 34N/m (Fig. 12d).

Table 2 Lower and upper bounds for searching optimal parameters of magnetic NVAs

Optimization bounds	Value
$[d_{x_min}, d_{x_max}]$	[0.010, 0.040] m
$[d_{y_min}, d_{y_max}]$	[0.005, 0.040] m
$[k_{a_min}, k_{a_max}]$	[10, 120] N/m

The optimization results of 3AMNVA are shown in Fig. 13. The optimal parameters, stable equilibrium and metric of 3AMNVA are $d_x = 0.022$ m,

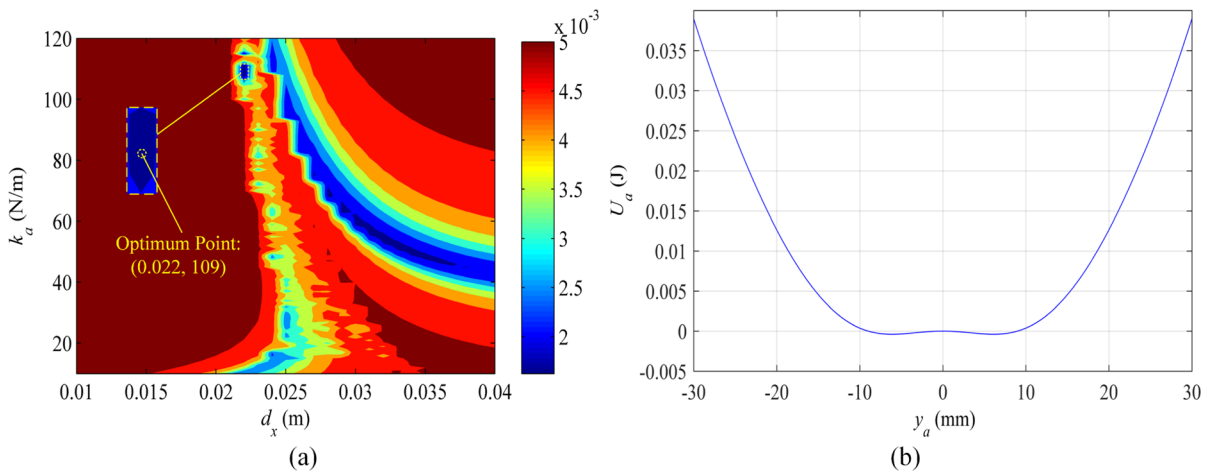


Fig. 9 Optimization results under $q_p = 2$ mm and potential energy of 2RMNVA: **a** contour of P value of 2RMNVA, **b** potential energy of the optimal 2RMNVA

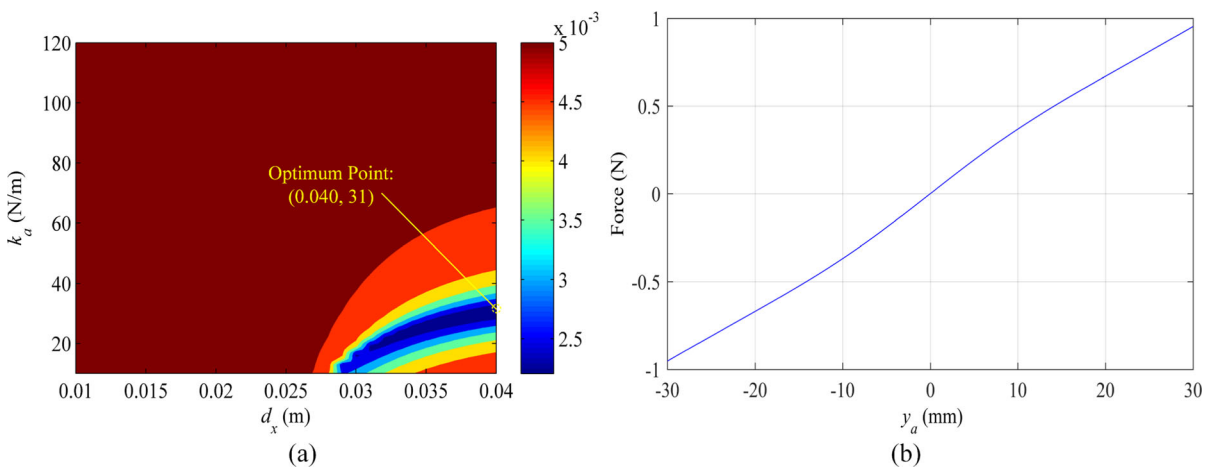


Fig. 10 Optimization results under $q_p = 2$ mm and potential energy of 2AMNVA: **a** contour of P value of 2AMNVA, **b** restoring force of the optimal 2AMNVA

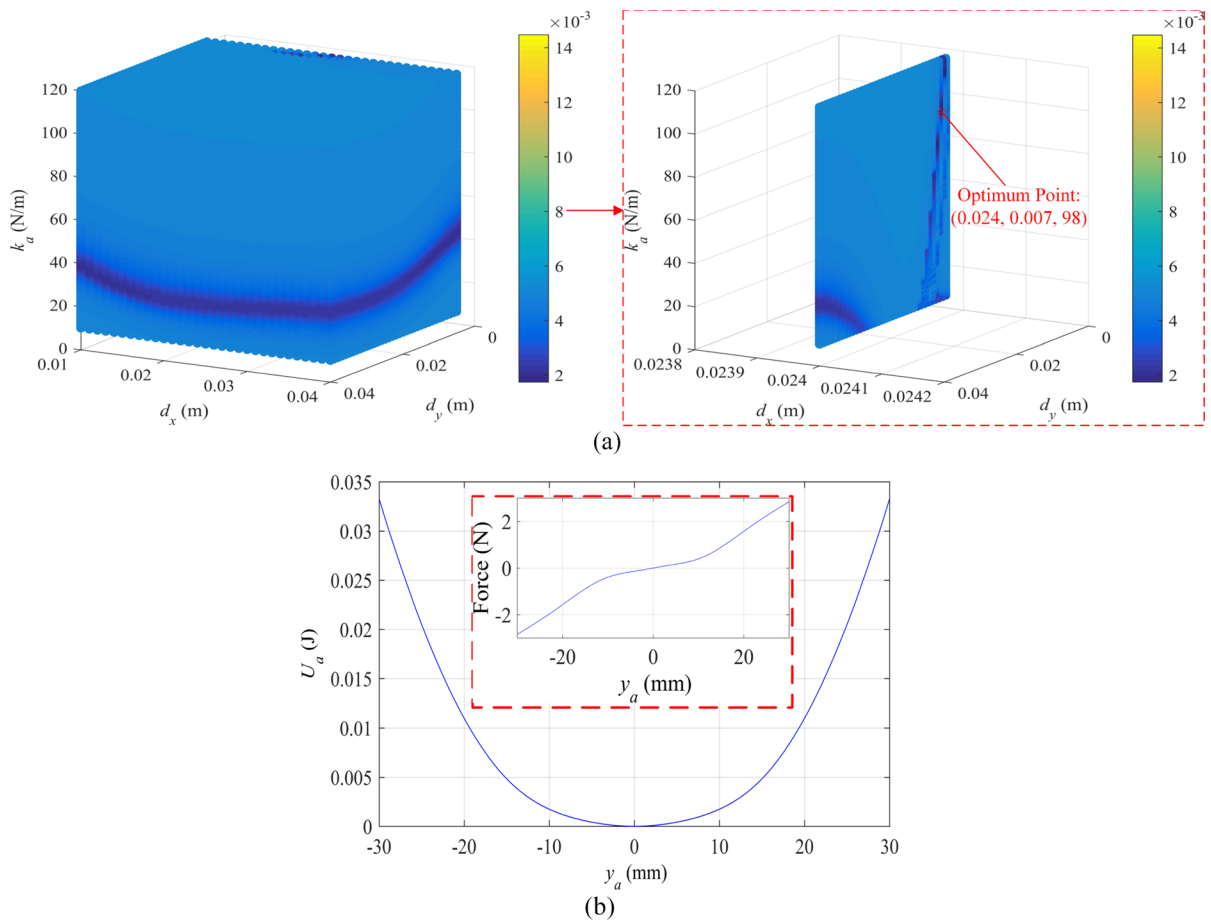


Fig. 11 Optimization results under $q_p = 2$ mm and potential energy/restoring force of 3RMNVA: **a** contour of P value of 3RMNVA, **b** potential energy and restoring force of the optimal 3RMNVA

$d_y = 0.014$ m, $k_a = 62$ N/m, $q_a = 0.00672$ m and $P = 0.0017$. The optimal 3AMNVA is a weak bistable structure (Fig. 13b).

The detailed results in different intervals of d_x are shown in Fig. 14. It is noted that when d_x is in the interval $[0.010, 0.016)$, the strong vibration suppression area (dark blue area) predominantly exists at the high value of d_y and with the increase of d_y , the preferred k_a gradually decreases (Fig. 14a). When d_x is in the interval $[0.016, 0.024)$, the strong vibration suppression area appears at the low value of d_y (e.g., the slice plot in Fig. 14b) and the optimum point is obtained in this domain (Fig. 13a). When d_x is in the

interval $[0.024, 0.031)$, with the increase of d_y , the preferred k_a increases and then decreases (Fig. 14c). When d_x is in the interval $[0.031, 0.040)$, with the increase of d_y , the preferred k_a gradually increases and stabilizes at about 40 N/m (Fig. 14d).

Figure 15 shows the comparison of transient responses of the optimal NVAs with different magnet arrangements and LVA under the low-level excitation ($q_p = 2$ mm). After the initial disturbance, the primary structure exhibit decaying oscillation about its own natural frequency 12.07 Hz. Since the natural frequency of LVA needs to be close to the vibration frequency, for the optimal LVA, the optimized

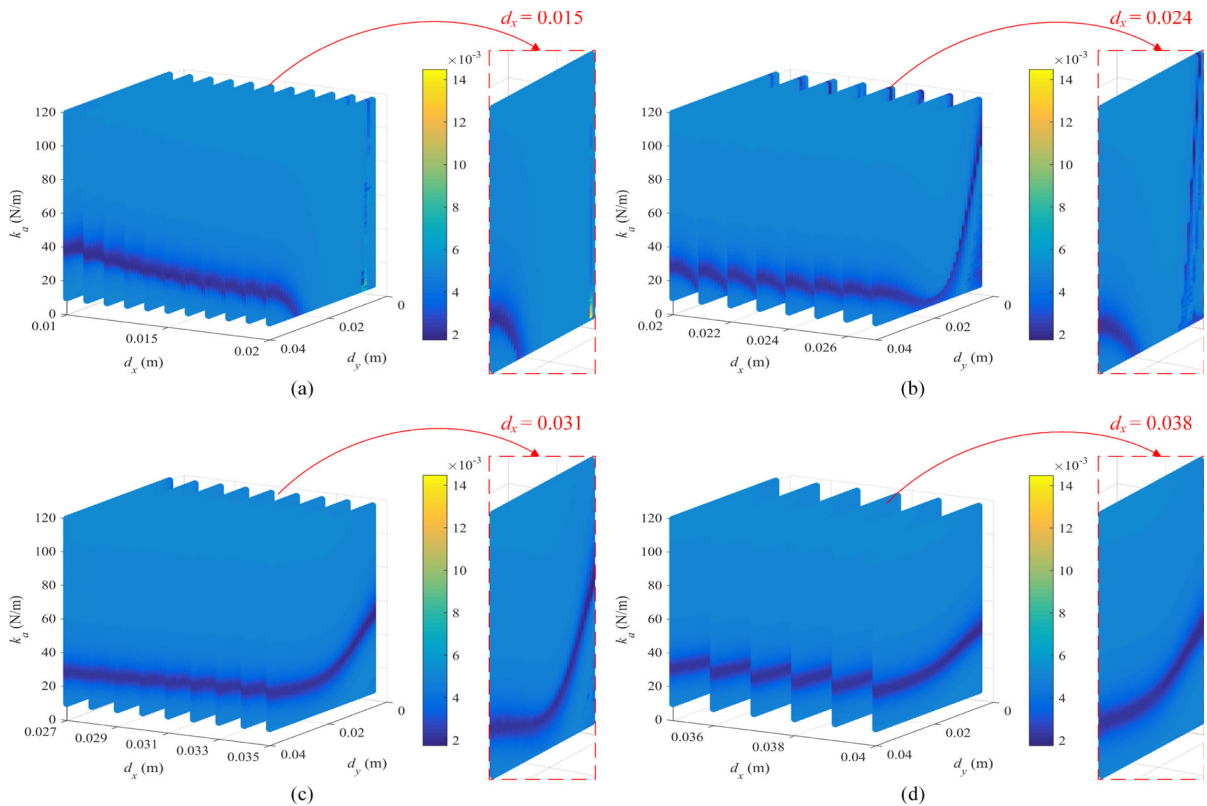


Fig. 12 Contour of P value of 3RMNVA under $q_p = 2$ mm: $d_x \in$ **a** [0.010, 0.020], **b** [0.020, 0.027], **c** [0.027, 0.035] and **d** [0.035, 0.040]

stiffness is 37 N/m and the natural frequency is 12 Hz [1–3]. As shown in Fig. 15a and d, 2RMNVA has the best vibration suppression performance. Also, from the total energy curve (Fig. 15c), it can be found that the total energy of the primary structure and optimized 2RMNVA decrease more quickly than others due to the vibration suppression performance of 2RMNVA. Finally, the total energy of primary structure and optimized 2RMNVA/3AMNVA stays at the negative potential position because 2RMNVA/3AMNVA stabilizes at the lowest point of potential well (Fig. 9b and 13b). As shown in Fig. 15b, 2RMNVA and 3AMNVA first experience strong cross-well oscillations, and then gradually stabilizes at a certain non-zero stable equilibrium position, leading to their good vibration suppression performance. In Refs. [23–26],

the enhanced effects of cross-well oscillations on vibration suppression are also observed.

The wavelet transform (WT) spectra of the displacements of the primary structure and the optimal magnetic NVAs under $q_p = 2$ mm are shown in Fig. 16. It is noted that the dominant frequencies of the primary structure and the optimal magnetic NVAs are both around 12 Hz, indicating that the primary structure and the optimal magnetic NVAs are in the 1:1 resonance around a frequency close to the natural frequency of the primary structure. By comparing Fig. 16a, c e and g, it is noted that the primary structure with the 2RMNVA has the fastest rate to dissipate the energy of the primary structure, and the 2AMNVA has the worst performance.

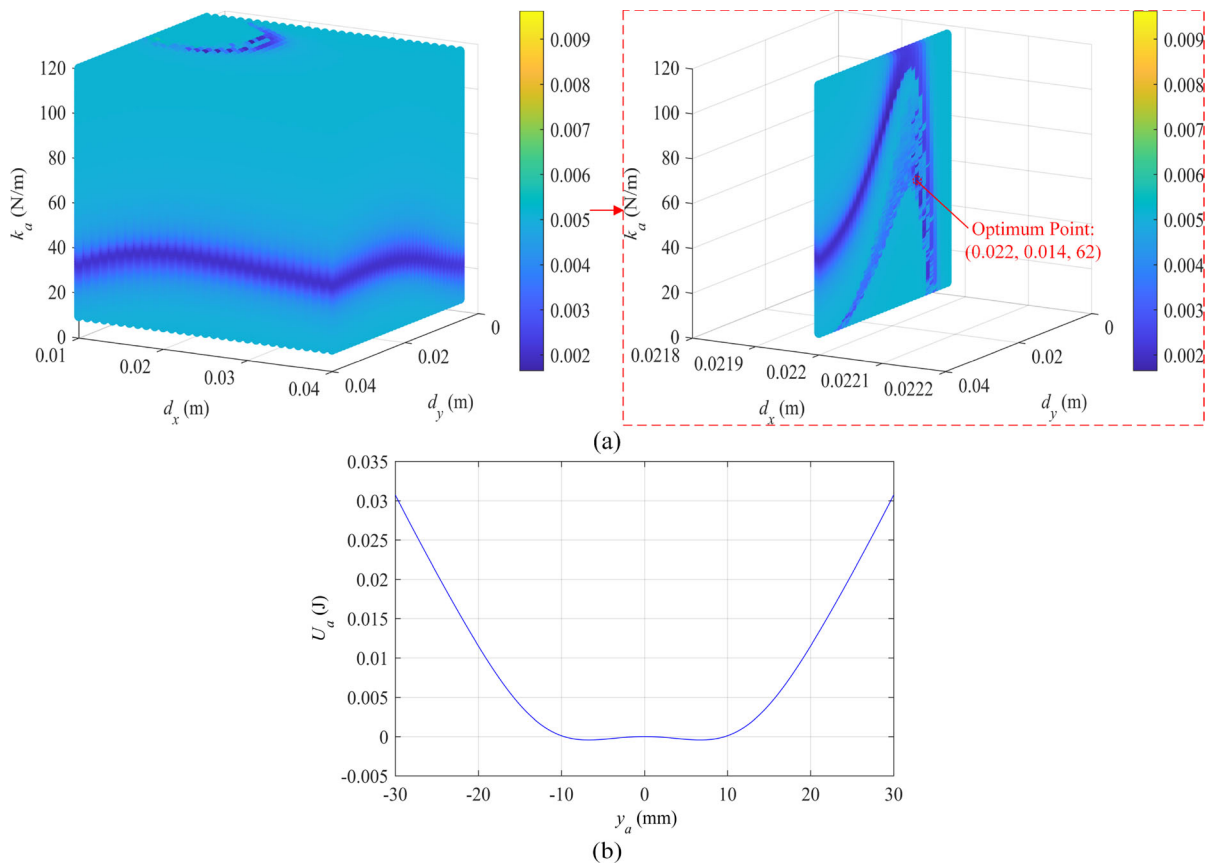


Fig. 13 Optimization results under $q_p = 2$ mm and potential energy of 3AMNVA: **a** contour of P value of 3AMNVA, **b** potential energy of the optimal 3AMNVA

3.2 Intermediate-level excitation

Under the condition of intermediate-level excitation, the initial displacement of the primary structure is set as $q_p = 6$ mm.

The optimization results of 2RMNVA are shown in Fig. 17. When d_x is smaller than 0.021, the vibration suppression performance of 2RMNVA is poor. When d_x is greater than 0.024, the preferred k_a under different values of d_x gradually stabilizes at about 39 N/m (dark blue area). Based on the optimization results, the optimal parameters, stable equilibrium and metric of 2RMNVA are $d_x = 0.036$ m, $k_a = 40$ N/m, $q_a = 0$ m and $P = 0.0182$. As shown in Fig. 17b, the optimal 2RMNVA is a weak monostable structure.

The optimization results of 2AMNVA are shown in Fig. 18. When d_x is smaller than 0.026, the vibration suppression performance of 2AMNVA is poor. When d_x is greater than 0.027, the preferred k_a with the increase of d_x gradually stabilizes at about 35 N/m (dark blue area). Based on the optimization results, the optimal parameters, stable equilibrium and metric of 2AMNVA are $d_x = 0.040$ m, $k_a = 35$ N/m, $q_a = 0$ m and $P = 0.0194$. The value of d_x and the restoring force of the optimal 2AMNVA (Fig. 18b) indicates that the optimal 2AMNVA is close to a LVA.

The optimization results of 3RMNVA are shown in Fig. 19. It is noted that in Fig. 19a, most of the domain in the design space is yellow, indicating that the

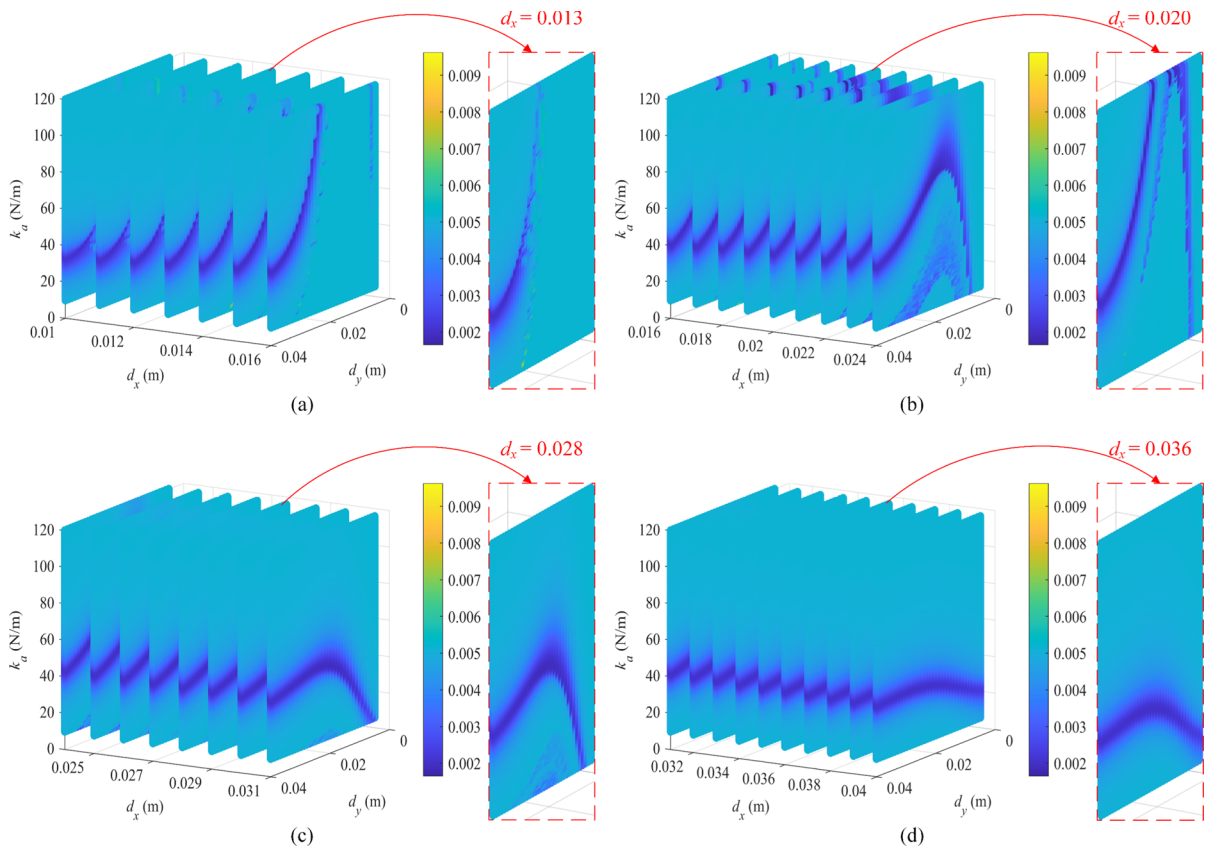


Fig. 14 Contour of P value of 3AMNVA under $q_p = 2$ mm: $d_x \in$ **a** [0.010, 0.016], **b** [0.016, 0.024], **c** [0.024, 0.031] and **d** [0.031, 0.040]

vibration suppression performance of the 3RMNVAs is generally poor. Based on the optimization results, the optimal parameters, stable equilibrium and metric of 3RMNVA are $d_x = 0.016$ m, $d_y = 0.007$ m, $k_a = 51$ N/m, $q_a = 0$ m and $P = 0.0149$. As shown in Fig. 19b, the optimal 3RMNVA is a tristable structure.

From the detailed optimization results (Fig. 20), it is noted that when d_x is in the interval [0.010, 0.013], the effective vibration suppression area (blue area) predominantly exists at the high value of d_y (Fig. 20a). When d_x is in the interval [0.013, 0.034), the effective vibration suppression area appears at the low value of d_y (e.g., the slice plot in Fig. 20b) and the optimum point is obtained in this domain (Fig. 19a). Gradually the effective vibration suppression area spreads across

different values of d_y , and merges with the increase of d_x (Fig. 20b, c). When d_x is in the interval [0.034, 0.040], the preferred k_a stabilizes at about 36 N/m (Fig. 20d).

The optimization results of 3AMNVA are shown in Fig. 21. It is noted that in most of the domain in the design space, the vibration suppression performance of the 3AMNVAs is poor. The optimal parameters, stable equilibrium and metric of 3AMNVA are $d_x = 0.010$ m, $d_y = 0.027$ m, $k_a = 50$ N/m, $q_a = 0$ m and $P = 0.0140$. As shown in Fig. 21b, the optimal 3AMNVA is a tristable structure.

From the detailed optimization results (Fig. 22), it is noted that when d_x is in the interval [0.010, 0.016], the effective vibration suppression area (blue area)

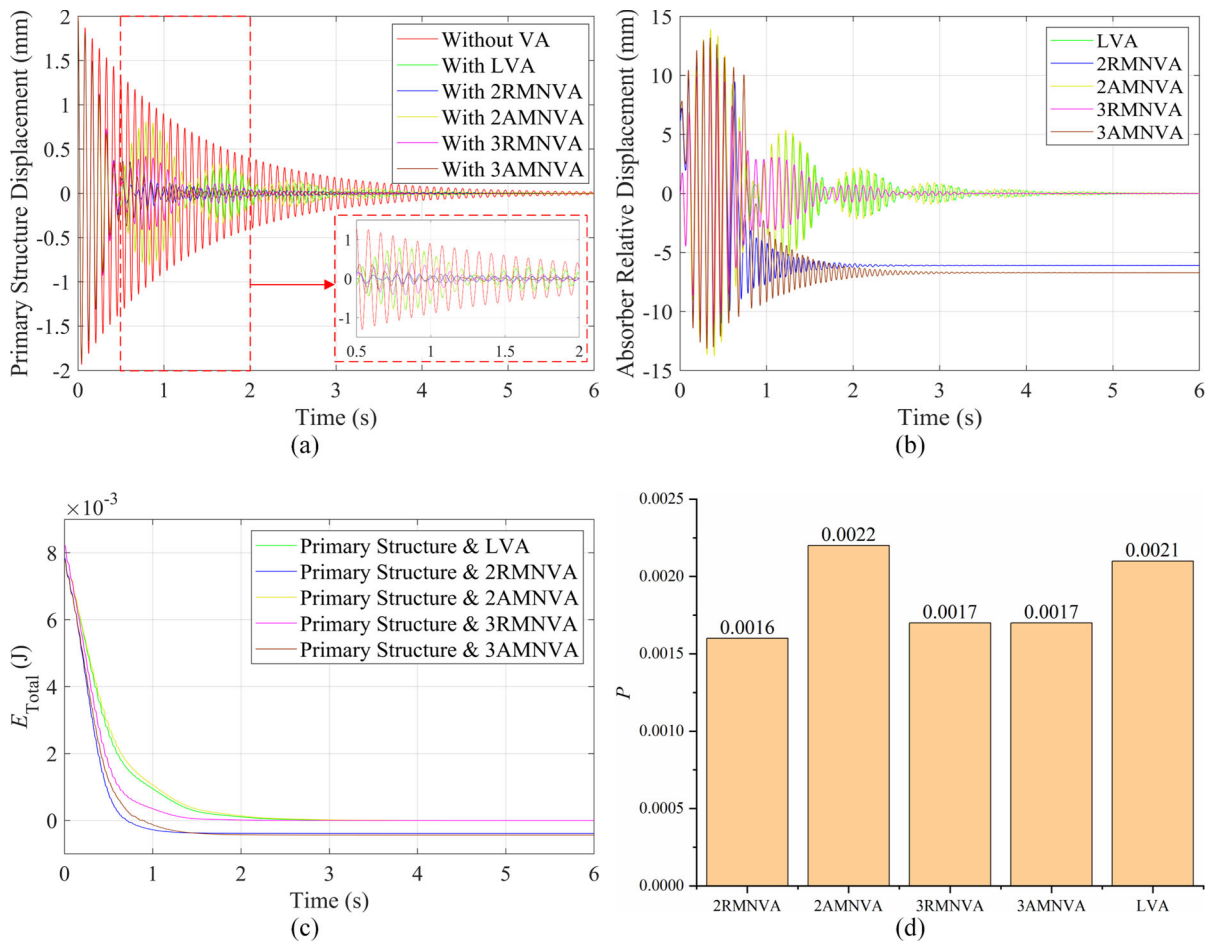


Fig. 15 **a** Displacement of primary structure with optimal LVA and different magnetic NVAs, **b** displacements of optimal LVA and different magnetic NVAs relative to the primary structure,

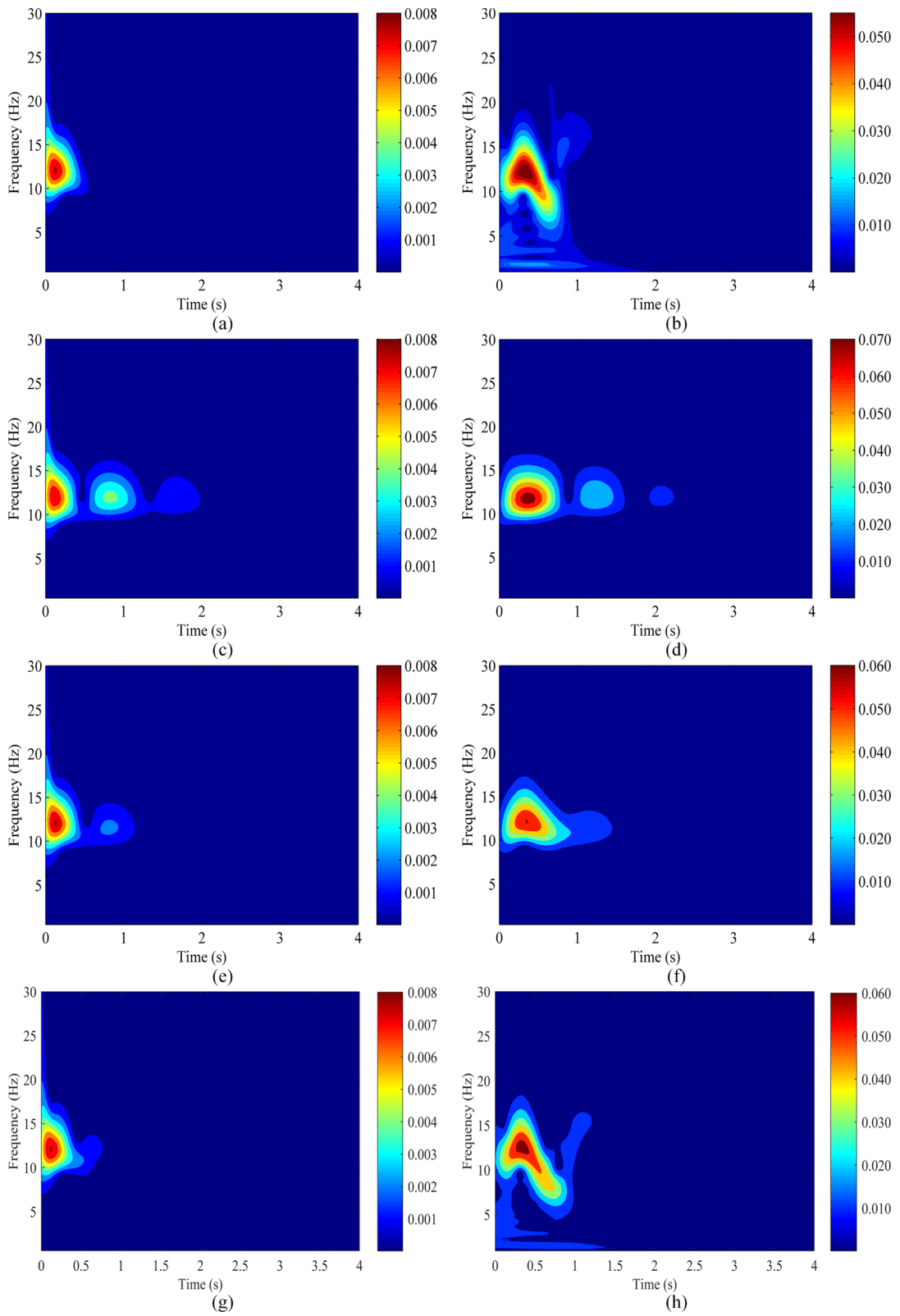
c total energy of primary structure with optimal magnetic NVAs and **d** P of optimal LVA and different magnetic NVAs under $q_p = 2$ mm

predominantly exists at the high value of d_y (Fig. 22a) and the optimum point is obtained in this domain (Fig. 21a). When d_x increases in the interval [0.016, 0.034), the effective vibration suppression area appears at the low value of d_y (e.g., the slice plot in Fig. 22b), spreads across the different values of d_y and merges (Fig. 22b, c). When d_x is in the interval [0.034, 0.040), the preferred k_a stabilizes at about 38 N/m (Fig. 22d).

According to the above analysis of optimization results of NVAs with different magnetic

arrangements, it can be found that for all magnetic NVAs, when d_x is greater than a certain value (usually close to the bound of d_x), the preferred k_a under different values of d_x (2RMNVA and 2AMNVA) and d_y (3RMNVA and 3AMNVA) stabilizes around a constant value.

Figure 23 shows the comparison of vibration suppression performance of the optimal NVAs with different magnet arrangements and LVA under the intermediate-level excitation ($q_p = 6$ mm). As shown in Fig. 23a and d, 3AMNVA has the best vibration



◀ **Fig. 16** WT spectra of displacement of primary structure with four optimal magnetic NVAs and the optimal magnetic NVAs under $q_p = 2$ mm: **a, b** 2RMNVA, **c, d** 2AMNVA, **e, f** 3RMNVA, **g, h** 3AMNVA

suppression performance. Also, from the total energy curve (Fig. 23c), it can be found that the total energy of the primary structure and optimized 3AMNVA decrease more quickly than others due to the vibration suppression performance of 3AMNVA. Finally, the total energy of primary structure and optimized 3RMNVA stays at the negative potential position because 3RMNVA stabilizes at the lowest point of

potential well (Fig. 19b). As shown in Fig. 23b, 3RMNVA and 3AMNVA first experience strong cross-well oscillations, and then gradually stabilizes at an equilibrium position, which is conducive their vibration suppression performance.

The wavelet transform (WT) spectra of the displacements of the primary structure and the optimal magnetic NVAs under $q_p = 6$ mm are shown in Fig. 24. It is noted that the dominant frequency of the primary structure and the optimal magnetic NVAs are both around 12 Hz, indicating that the primary structure and the optimal magnetic NVAs are in the 1:1 resonance around a frequency close to the natural frequency of the primary structure. By comparing

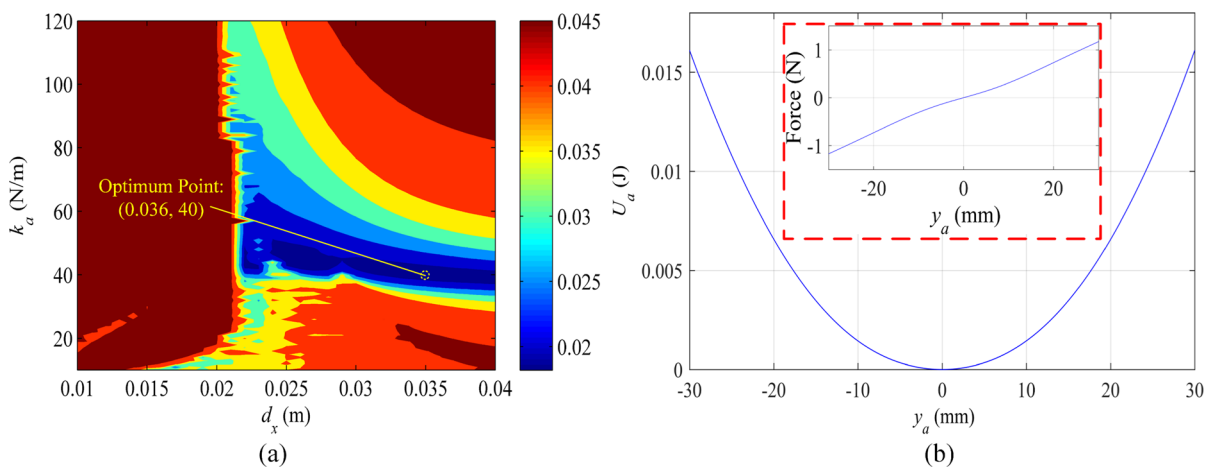


Fig. 17 Optimization results under $q_p = 6$ mm and potential energy/restoring force of 2RMNVA: **a** contour of P value of 2RMNVA, **b** potential energy and restoring force of the optimal 2RMNVA

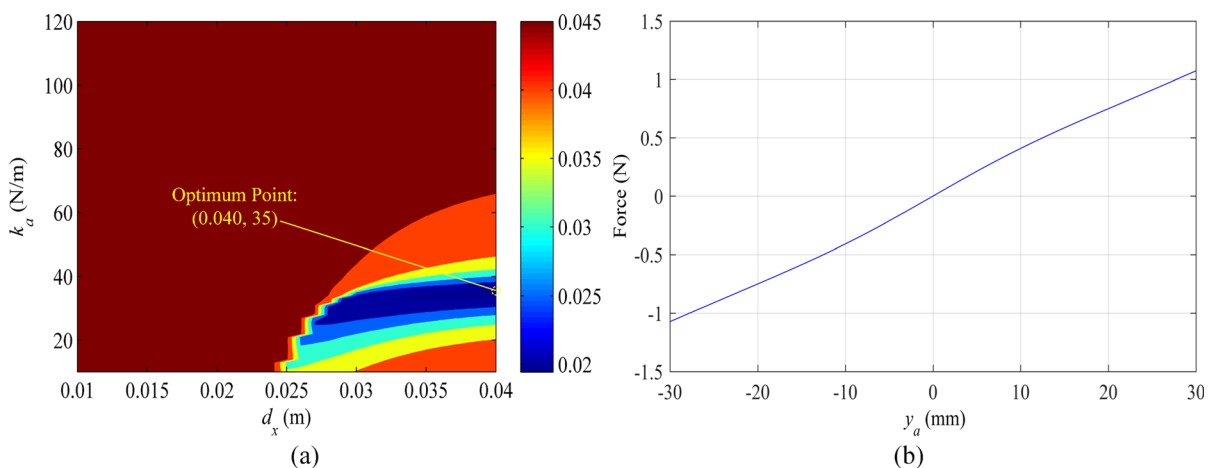


Fig. 18 Optimization results under $q_p = 6$ mm and restoring force of 2AMNVA: **a** contour of P value of 2AMNVA, **b** restoring force of the optimal 2AMNVA

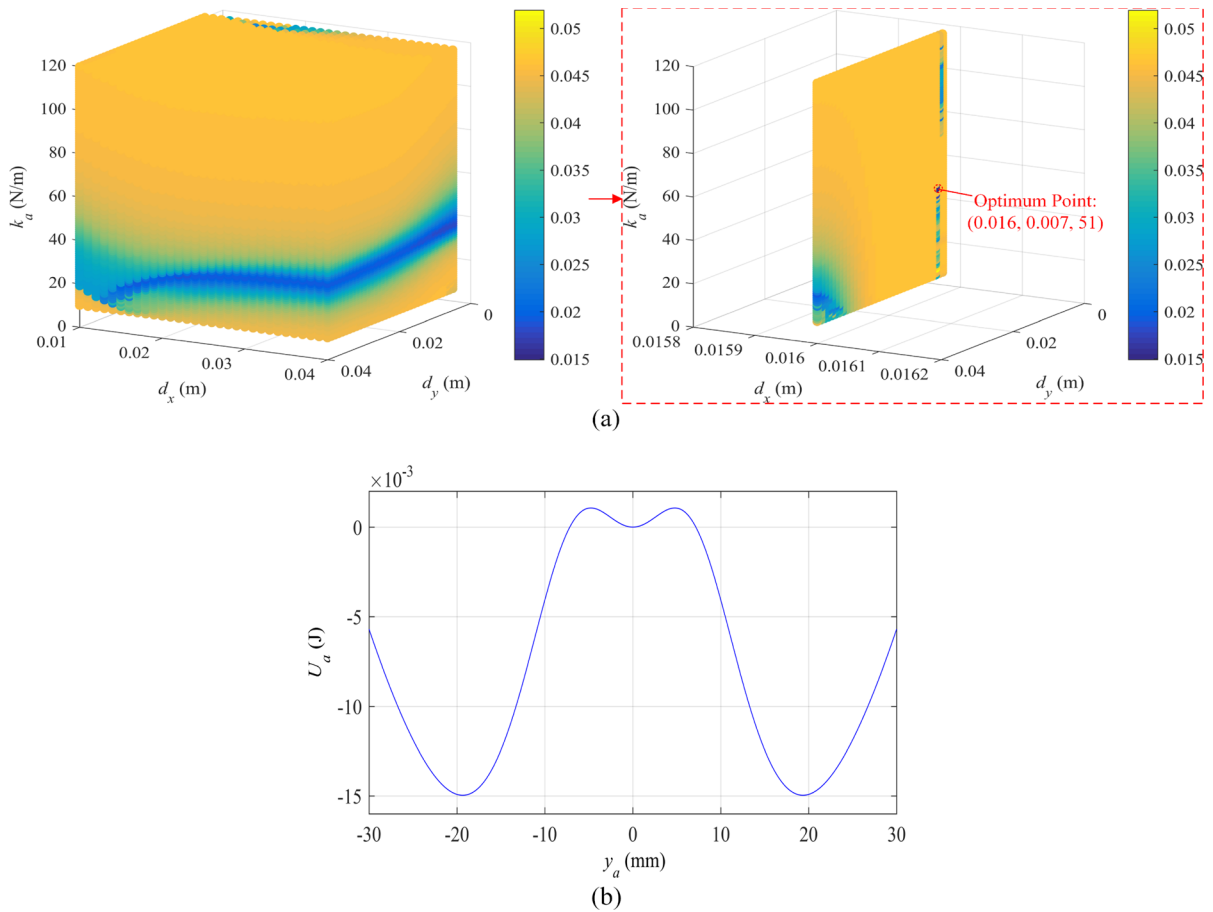


Fig. 19 Optimization results under $q_p = 6$ mm and potential energy of 3RMNVA: **a** contour of P value of 3RMNVA, **b** potential energy of the optimal 3RMNVA

Fig. 24a, c, e and g, it is noted that within the initial 0.8 s vibration, the primary structure with 3AMNVA has the fastest energy dissipation rate (can be noted by comparing the shades at 0.8 s), and both 2RMNVA and 2AMNVA have much worse performance.

3.3 High-level excitation

Under the condition of high-level excitation, the initial displacement of the primary structure is set as $q_p = 12$ mm.

The optimization results of 2RMNVA are shown in Fig. 25. When d_x is smaller than 0.020, the vibration suppression performance of 2RMNVA is poor. When

d_x is greater than 0.020, the preferred k_a under different values of d_x stabilize at about 38 N/m. Based on the optimization results, the optimal parameters, stable equilibrium and metric of 2RMNVA are $d_x = 0.022$ m, $k_a = 39$ N/m, $q_a = 0.01298$ m and $P = 0.0702$. As shown in Fig. 25b, the optimal 2RMNVA is a bistable structure.

The optimization results of 2AMNVA are shown in Fig. 26. When d_x is smaller than 0.024, the vibration suppression performance of 2AMNVA is poor. When d_x is greater than 0.024, the preferred k_a under different values of d_x stabilize at about 36 N/m. Based on the optimization results, the optimal parameters, stable equilibrium and metric of 2AMNVA are

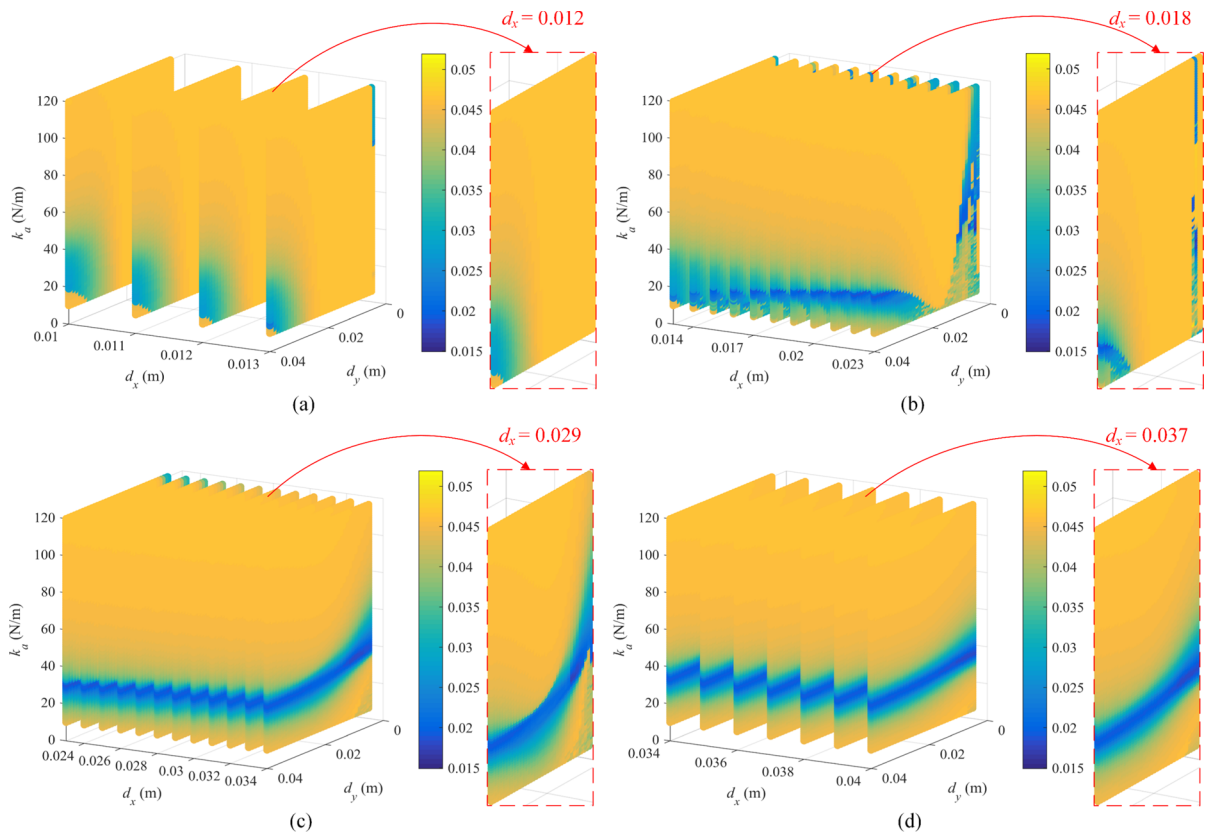


Fig. 20 Contour of P value of 3RMNVA under $q_p = 6$ mm: $d_x \in$ **a** [0.010, 0.013], **b** [0.013, 0.023], **c** [0.023, 0.034], **d** [0.034, 0.040]

$d_x = 0.039$ m, $k_a = 36$ N/m, $q_a = 0$ m and $P = 0.0771$. The value of d_x and the restoring force of the optimal 2AMNVA (Fig. 26b) indicates that the optimal 2AMNVA is close to a LVA.

The optimization results of 3RMNVA are shown in Fig. 27. It is noted that the vibration suppression performance of the 3RMNVAs in most of the domain in the design space are poor. The optimal parameters, stable equilibrium and metric of the 3RMNVA are $d_x = 0.018$ m, $d_y = 0.009$ m, $k_a = 40$ N/m, $q_a = 0$ m and $P = 0.0656$. As shown in Fig. 27b, the optimal 3RMNVA is a tristable structure.

The trend of the variation of vibration suppression performance of the 3RMNVA is similar to that under the intermediate-level excitation. As seen in Fig. 28, when d_x is in the interval [0.010, 0.012), the vibration suppression is only effective at the high value of d_y

(blue area in Fig. 28a). When d_x increases in the interval [0.012, 0.033), the effective vibration suppression area appears at the low value of d_y (e.g., the slice plot in Fig. 28b), spreads across the different values of d_y and merges (Fig. 28b, c). Meanwhile, the optimum point is obtained in this domain (Fig. 27a). When d_x is in the interval [0.033, 0.040], for different values of d_y , the preferred k_a stabilizes at about 36 N/m (Fig. 28d).

The optimization results of 3AMNVA are shown in Fig. 29. It is noted that the vibration suppression performance of the 3AMNVAs in most of the domain in the design space are poor. Based on the optimization results, the optimal parameters, stable equilibrium and metric of 3AMNVA are $d_x = 0.013$ m, $d_y = 0.026$ m, $k_a = 39$ N/m, $q_a = 0$ m and $P = 0.0661$. As shown in Fig. 29c, the optimal 3AMNVA is a tristable structure.

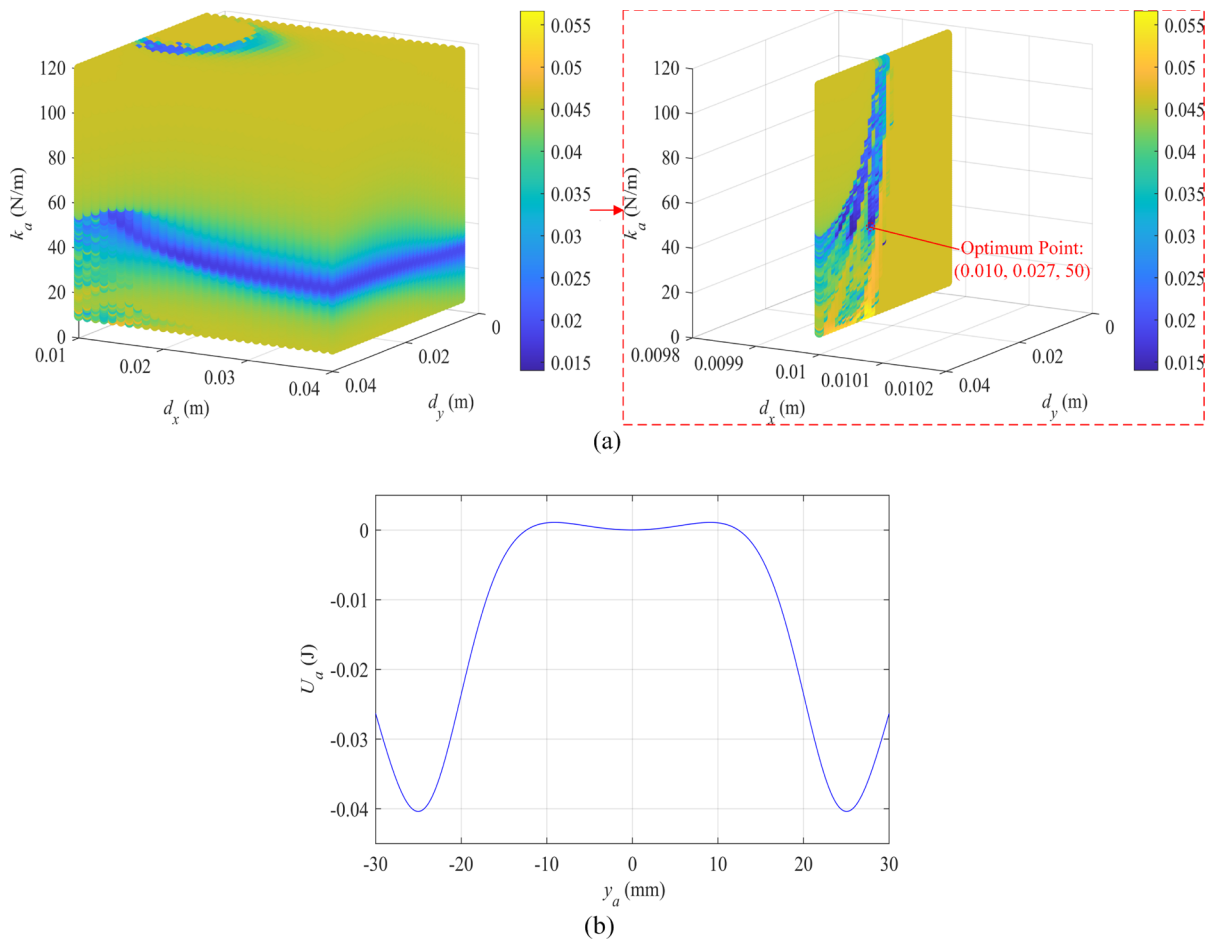


Fig. 21 Optimization results under $q_p = 6$ mm and potential energy of 3AMNVA: **a** contour of P value of 3AMNVA, **b** potential energy of the optimal 3AMNVA

The trend of the variation of vibration suppression performance of the 3AMNVA is similar to that under the intermediate-level excitation. As seen in Fig. 30, when d_x is in the interval $[0.010, 0.019)$, the effective vibration suppression area (blue area) predominantly exists at the high value of d_y (Fig. 30a) and the optimum point is obtained in this domain (Fig. 29a). When d_x increases in the interval $[0.019, 0.028)$, the effective vibration suppression area appears at the low value of d_y (e.g., the slice plot in Fig. 30b), spreads across the different values of d_y and merges (Fig. 30b, c). When d_x is in the interval $[0.028, 0.040]$, for

different values of d_y , the preferred k_a stabilizes at about 38 N/m (Fig. 30d).

According to the above analysis of the optimization results of NVAs with different magnet arrangements, it can be noted that the preferred k_a under different values of d_x (2RMNVA and 2AMNVA) and d_y (3RMNVA and 3AMNVA) remains nearly constant when d_x is at a high value. This result is similar to the observation in the optimization results under intermediate-level excitation.

Figure 31 shows the comparison of vibration suppression performance of the optimal NVAs with

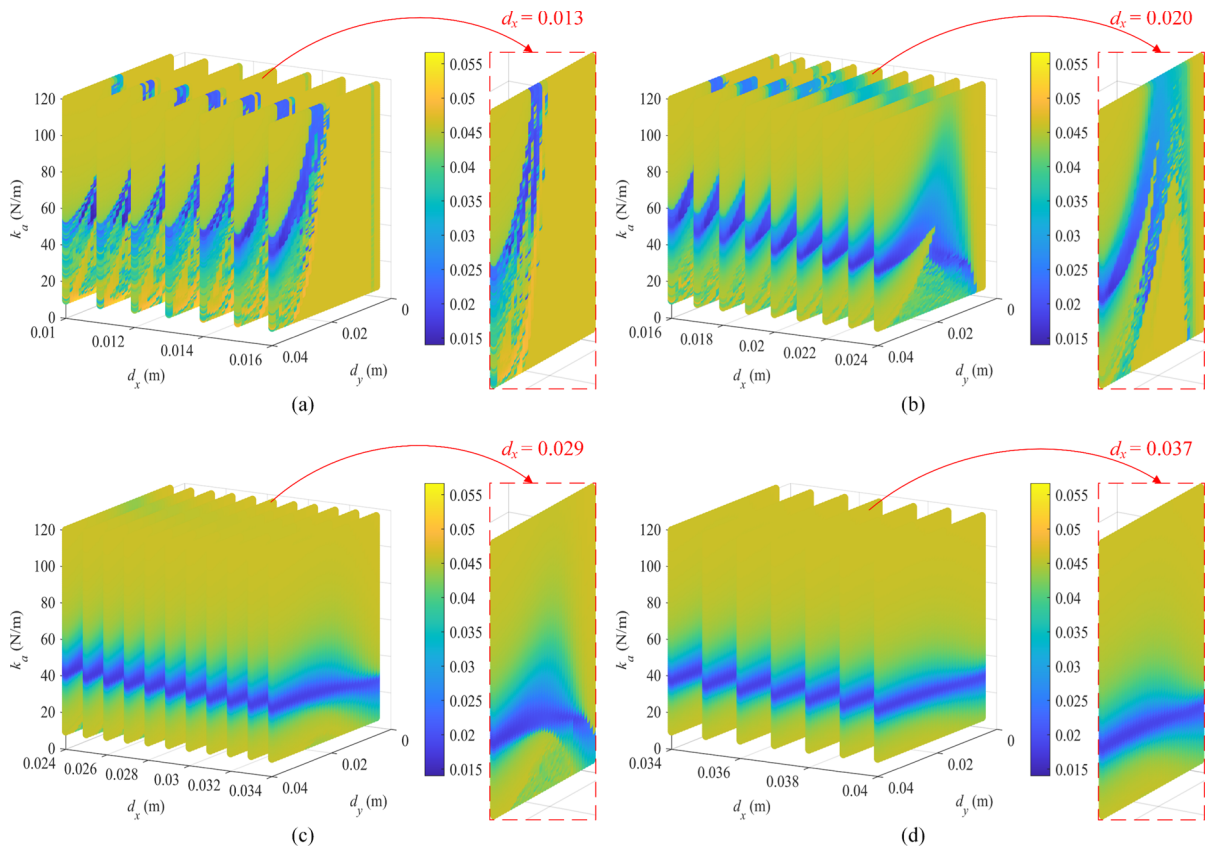


Fig. 22 Contour of P value of 3AMNVA under $q_p = 6$ mm: $d_x \in$ **a** [0.010, 0.016], **b** [0.016, 0.024], **c** [0.024, 0.034], **d** [0.034, 0.040]

different magnet arrangements and LVA under the high-level excitation ($q_p = 12$ mm). As seen in Fig. 31a and d, 3RMNVA and 3AMNVA provide outstanding vibration suppression performance. Also, from the total energy curve (Fig. 31c), it can be found that the total energy of the primary structure and optimized 3RMNVA/3AMNVA decrease more quickly than others due to the vibration suppression performance of 3RMNVA/3AMNVA. Finally, the total energy of primary structure and optimized 2RMNVA/3RMNVA/3AMNVA stays at the negative potential position because 2RMNVA/3RMNVA/3AMNVA stabilizes at the lowest point of potential well (Fig. 25b, 27b and 29b). As shown in Fig. 31b, 2RMNVA, 3RMNVA and 3AMNVA all experience strong cross-well oscillations before settling in one

stable equilibrium, improving their vibration suppression performance as compared to 2AMNVA and LVA.

The wavelet transform (WT) spectra of displacement of the primary structure and the optimal magnetic NVAs under $q_p = 12$ mm are shown in Fig. 32. It is noted that the dominant frequency of the primary structure and the optimal magnetic NVAs are both around 12 Hz (close to the natural frequency of the primary structure), indicating that the primary structure and the optimal magnetic NVAs are in the 1:1 resonance around a frequency close to the natural frequency of the primary structure. By comparing Fig. 32a, c, e and g, it is noted that the primary structure with 3AMNVA has the fastest energy dissipation rate, and 2AMNVA has the worst performance.

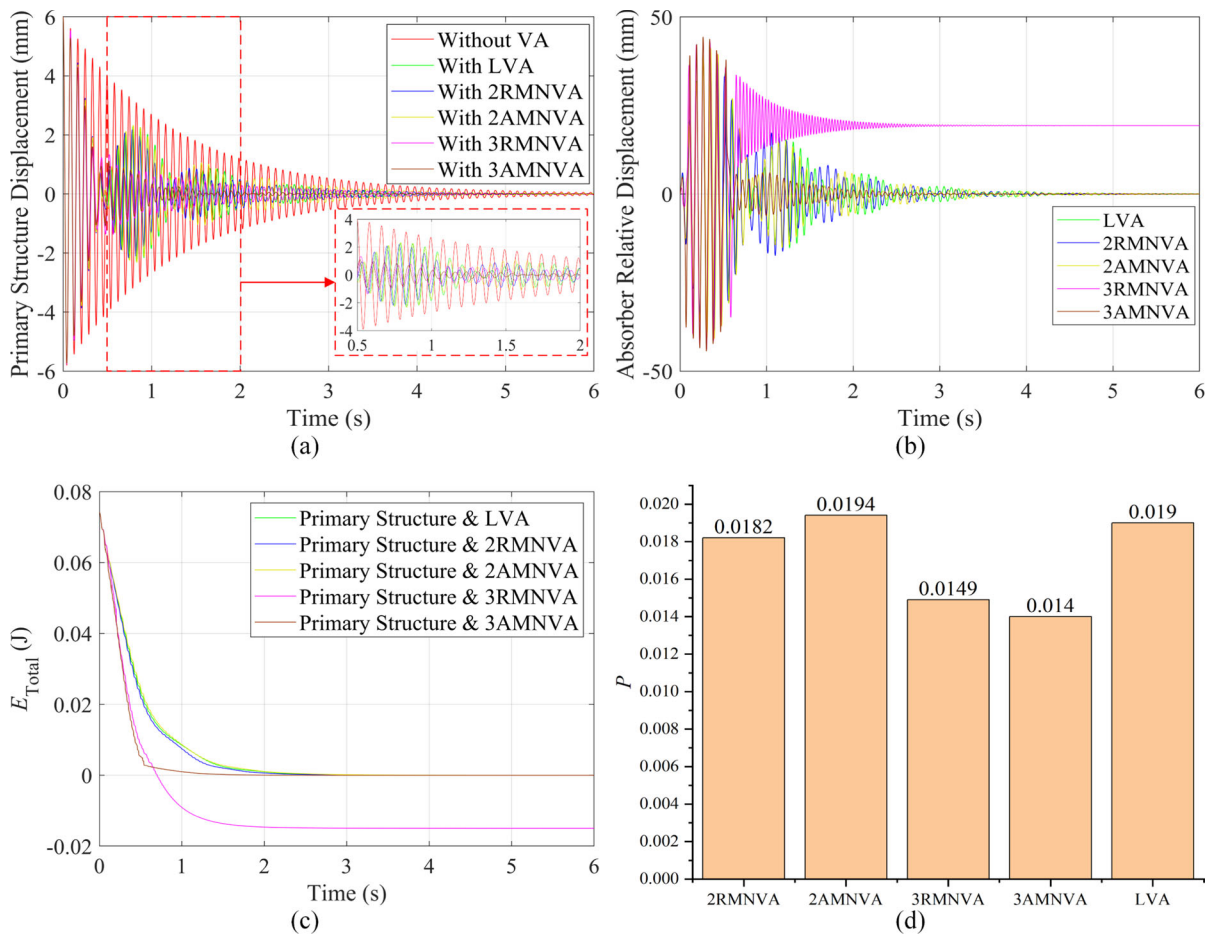


Fig. 23 **a** Displacement of primary structure with optimal LVA and different magnetic NVAs, **b** displacements of optimal LVA and different magnetic NVAs relative to the primary structure,

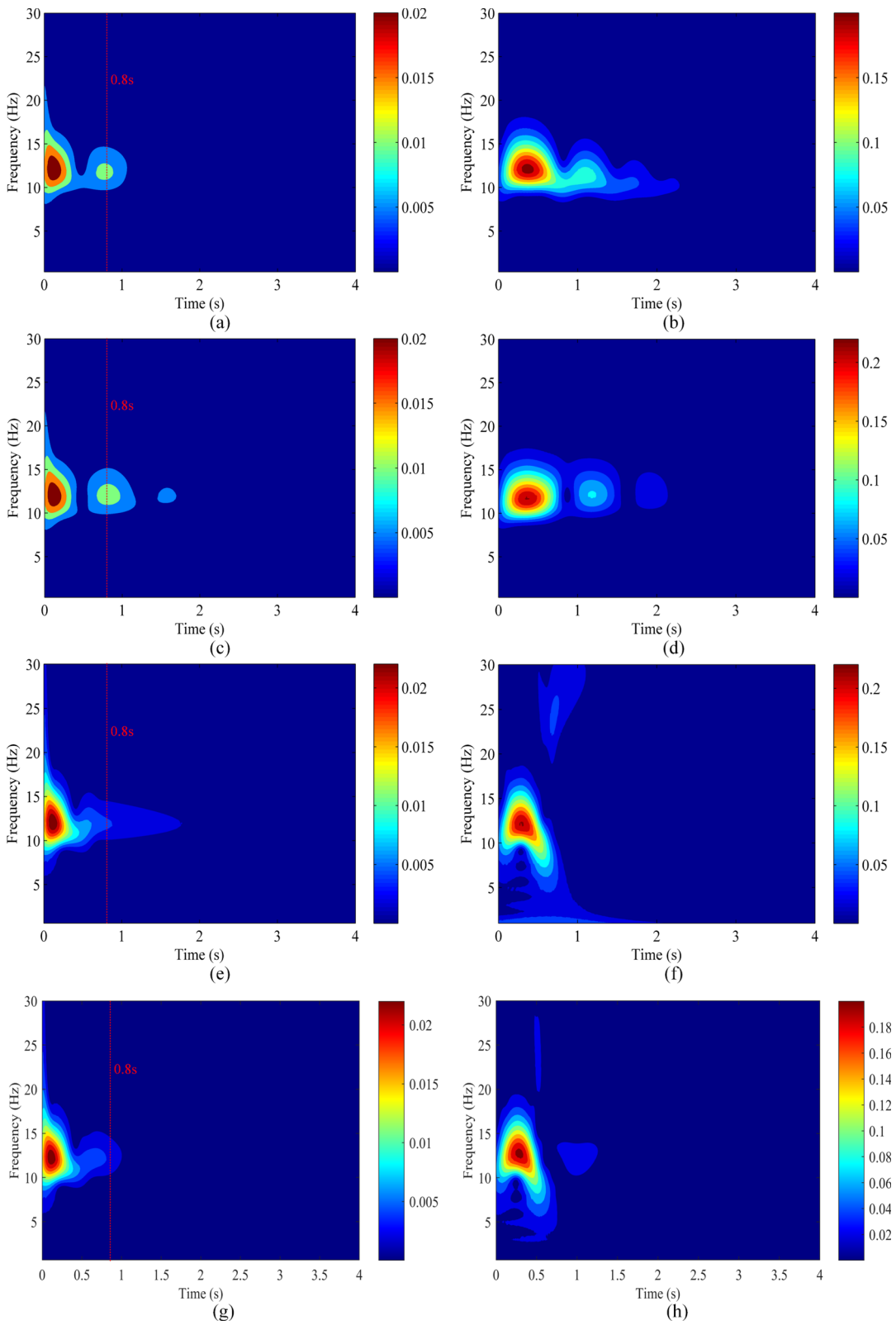
c total energy of primary structure with optimal magnetic NVAs and **d** P of optimal LVA and different magnetic NVAs under $q_p = 6$ mm

It is worth noting that although the optimal 3RMNVA has the lower value of P than the optimal 2RMNVA, the optimal 2RMNVA dissipates the energy in a shorter time than the optimal 3RMNVA (shorter tail in Fig. 32a as compared to Fig. 32e). The reason is that the metric P evaluate the vibration performance of NVA in the whole process rather than the energy level at a moment. This result can be explained in Fig. 33. When $t \in [0.55, 1.04]$, the primary structure with the optimal 3RMNVA has the lower amplitude than that with the optimal 2RMNVA, and then when $t \in (1.04, 2.00]$, the primary structure with the optimal 2RMNVA shows the lower amplitude

than that with the optimal 3RMNVA, reflecting that 3RMNVA perform better in the initial state of vibration with large amplitude but 2RMNVA suppresses vibration more rapidly in the following state of vibration with small amplitude.

4 Verification and comparison with reported designs

To verify the effectiveness of optimization results and method in this paper, in this section, we first use our approach to optimize the key parameters of magnetic



◀ **Fig. 24** WT spectra of displacement of primary structure with four optimal magnetic NVAs and the optimal magnetic NVAs under $q_p = 6$ mm: **a, b** 2RMNVA, **c, d** 2AMNVA, **e, f** 3RMNVA, **g, h** 3AMNVA

NVAs in Refs. [23–25] to improve their vibration suppression performances, which verify the effectiveness of our optimization approach. Subsequently, to compare our optimized magnetic NVAs with other reported designs, the magnetic NVAs in Refs. [23–25] are used to suppress the vibration of the primary structure in this paper and their performances are optimized to ensure the fair comparison.

4.1 Verification of optimization method

In Sect. 3, exhaustion method is used to optimize the key parameters of magnetic NVAs. We further use this method to optimize their performance of the magnetic NVAs in Refs. [23–25] to verify its effectiveness. As shown in Fig. 34, the magnetic NVAs are a bistable magneto-piezoelectric absorber (Refs. [23, 24]) and a tristable magneto-piezoelectric absorber (Ref. [25]), which consist of a cantilever beam with a tip magnet and piezoelectric bimorph.

The parameters of the absorber and primary structure are shown in Table 3.

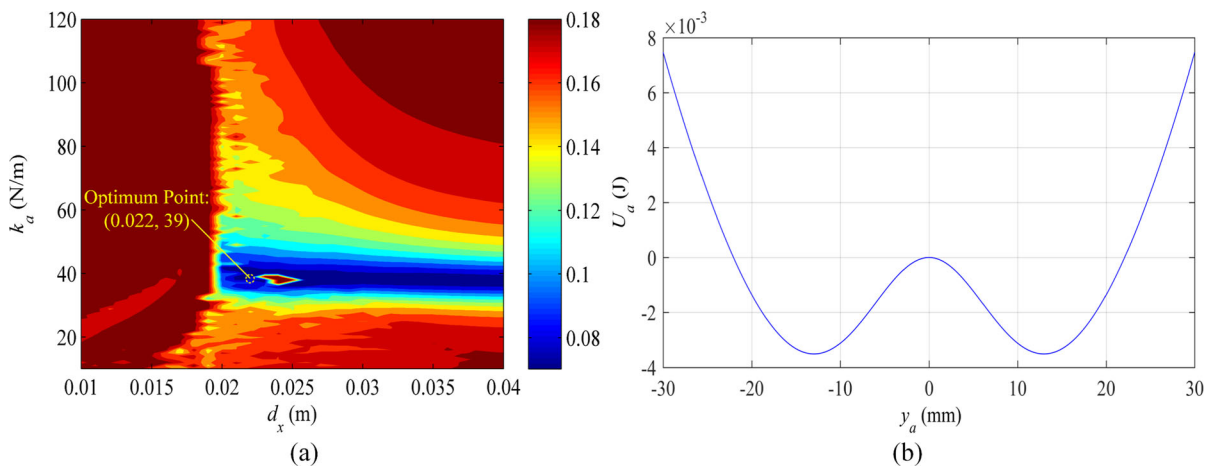


Fig. 25 Optimization results under $q_p = 12$ mm and potential energy of 2RMNVA: **a** contour of P value of 2RMNVA, **b** potential energy of the optimal 2RMNVA

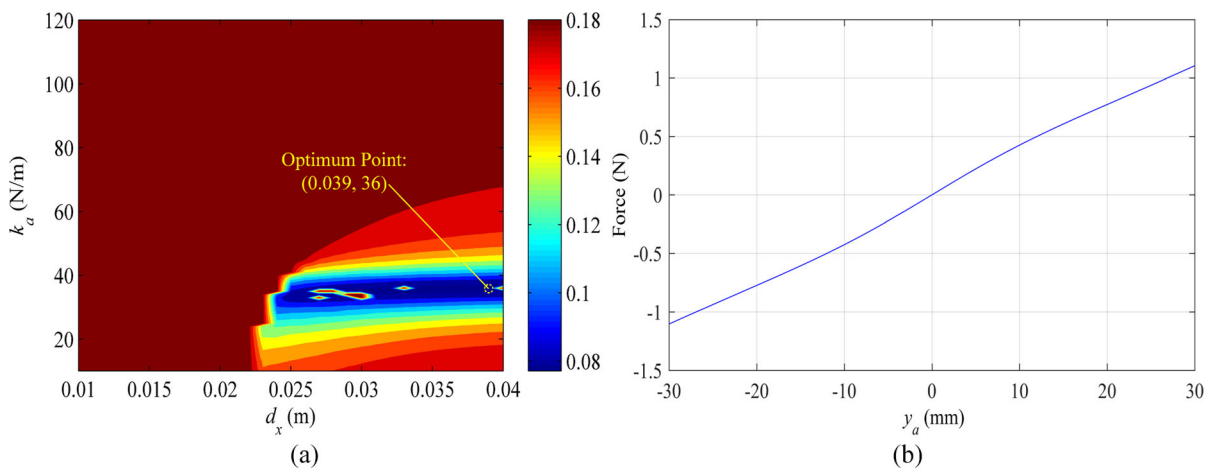


Fig. 26 Optimization results under $q_p = 12$ mm and restoring force of 2AMNVA: **a** contour of P value of 2AMNVA, **b** restoring force of the optimal 2AMNVA

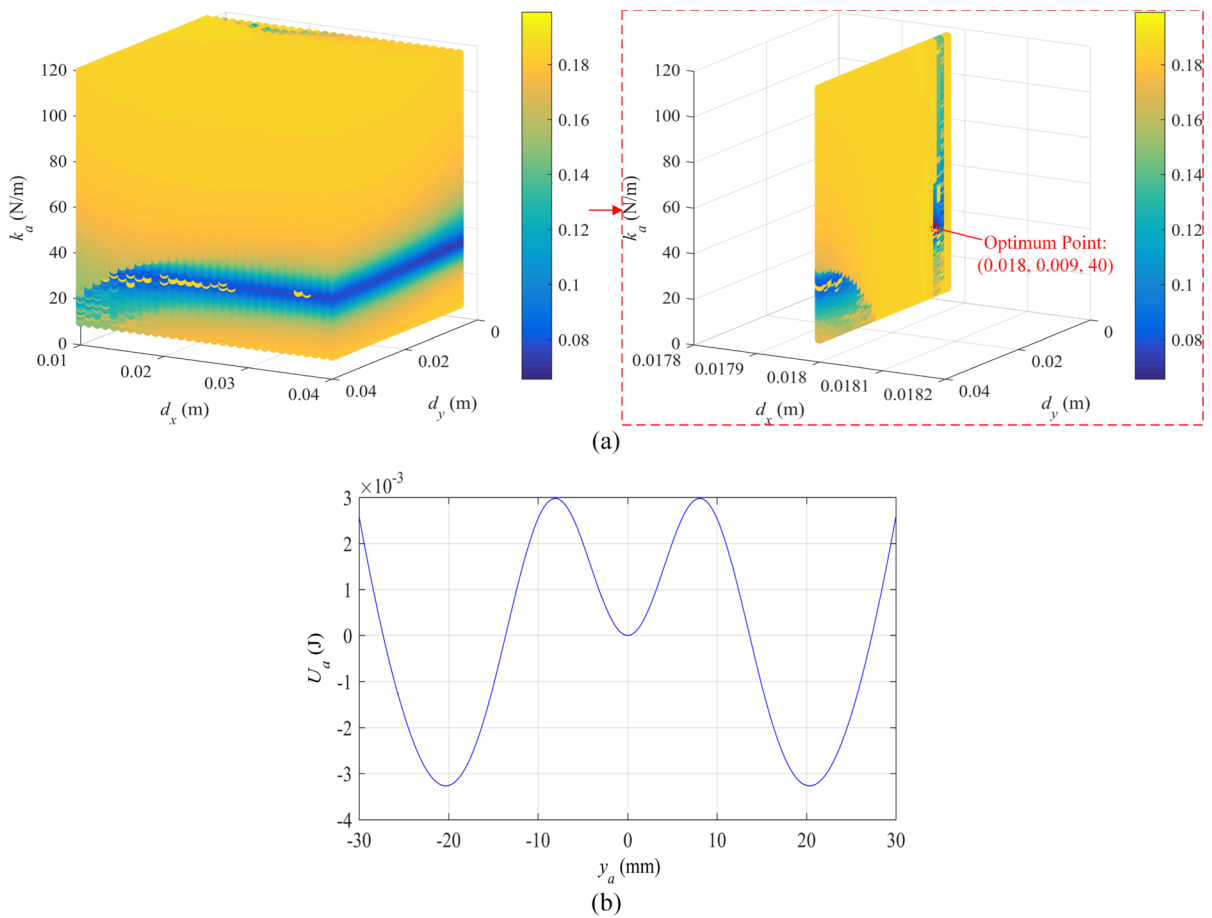


Fig. 27 Optimization results under $q_p = 12$ mm and potential energy of 3RMNVA: **a** contour of P value of 3RMNVA, **b** potential energy of the optimal 3RMNVA

To optimize the vibration suppression performance of the bistable and tristable absorbers, the lumped parameter model is built for fair comparison with our model, as shown in Fig. 35

The governing equations of such a system are:

$$\begin{cases} m_p \ddot{y}_p + c_p \dot{y}_p + k_p y_p - c_a \dot{y}_a - k_a y_a + F_y - \theta v = 0 \\ m_a (\ddot{y}_a + \ddot{y}_p) + c_a \dot{y}_a + k_a y_a - F_y + \theta v = 0 \\ v/R + C\dot{v} - \theta \dot{y}_a = 0 \end{cases} \quad (23)$$

Equation (23) is then written in the state space form for numerical simulation with ode45 function in MATLAB. According to Refs. [23–25], the initial

conditions are set to be $(q_p, 0, q_a, 0)$. $q_p = 0.0024$ m is the initial displacement of the primary structure, q_a is the stable equilibrium position of NVA. Based on the metric P in Eq. (21), the cantilever beam stiffness and magnet distances of the bistable magneto-piezoelectric absorber and tristable magneto-piezoelectric absorber are optimized through exhaustion method. The lower and upper bounds to search optimal parameters are shown in Table 4.

The optimization and comparison results are shown in Figs. 36 and 37, where 2RMNVA (Masoud et al. [23, 24]) and 3RMNVA (Masoud et al. [25]) represent the bistable magneto-piezoelectric absorber and

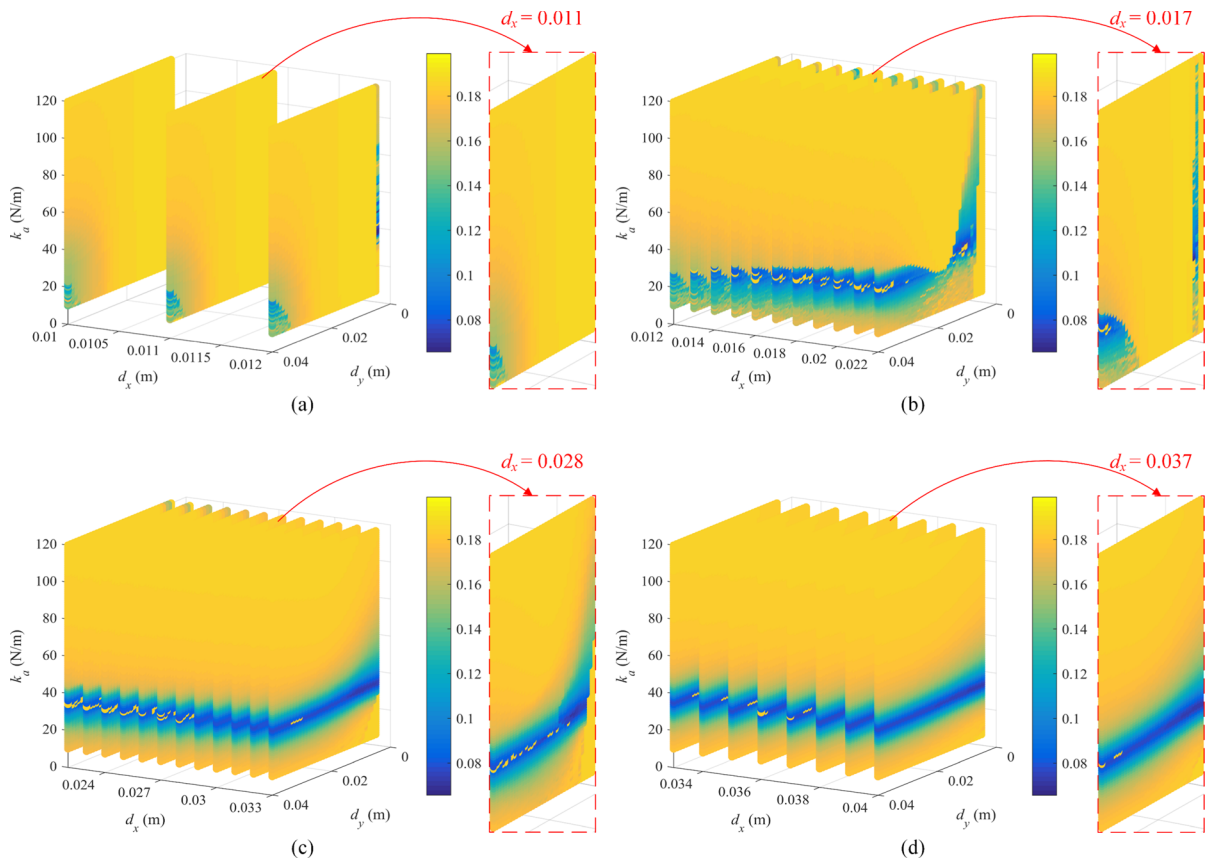


Fig. 28 Contour of P value of 3RMNVA under $q_p = 12$ mm: $d_x \in$ **a** [0.010, 0.012], **b** [0.012, 0.022], **c** [0.022, 0.033], **d** [0.033, 0.040]

tristable magneto-piezoelectric absorber in Refs. [23–25], respectively.

Based on the optimization results, the optimal parameters, stable equilibrium and metric of 2RMNVA of the system in Masoud et al. [23, 24] are $d_x = 0.019$ m, $k_a = 87$ N/m, $q_a = 0.0064$ m and $P = 0.00067353$. The optimized bistable 2RMNVA has the better vibration suppression performance than the original system (Fig. 36c and e) due to the larger oscillations crossing outmost wells (Fig. 36d) thanks to the shallow outmost well depth facilitating barrier crossing after optimization (Fig. 36b).

Based on the optimization results, the optimal parameters, stable equilibrium and metric of 3RMNVA in Masoud et al. [25] are $d_x = 0.015$ m, $d_y = 0.006$ m, $k_a = 85$ N/m, $q_a = 0$ m and $P = 0.00075066$. The optimized tristable 3RMNVA

has the better vibration suppression performance than the original system (Fig. 37c and e) due to the larger oscillation amplitude crossing outmost wells at the beginning state (Fig. 37d). The reason for the larger oscillation amplitude is the shallow middle well depth facilitating barrier crossing (Fig. 37b).

The improved performance of 2RMNVA and 3RMNVA in Ref. [23–25] verifies the effectiveness of the exhaustion method used in this paper.

4.2 Comparison with reported designs

To compare the performance of the designed magnetic NVAs in this paper with the existing designs, the bistable magneto-piezoelectric absorber (2RMNVA (Masoud et al. [23, 24])) and tristable magneto-piezoelectric absorber (3RMNVA (Masoud et al. [25]))

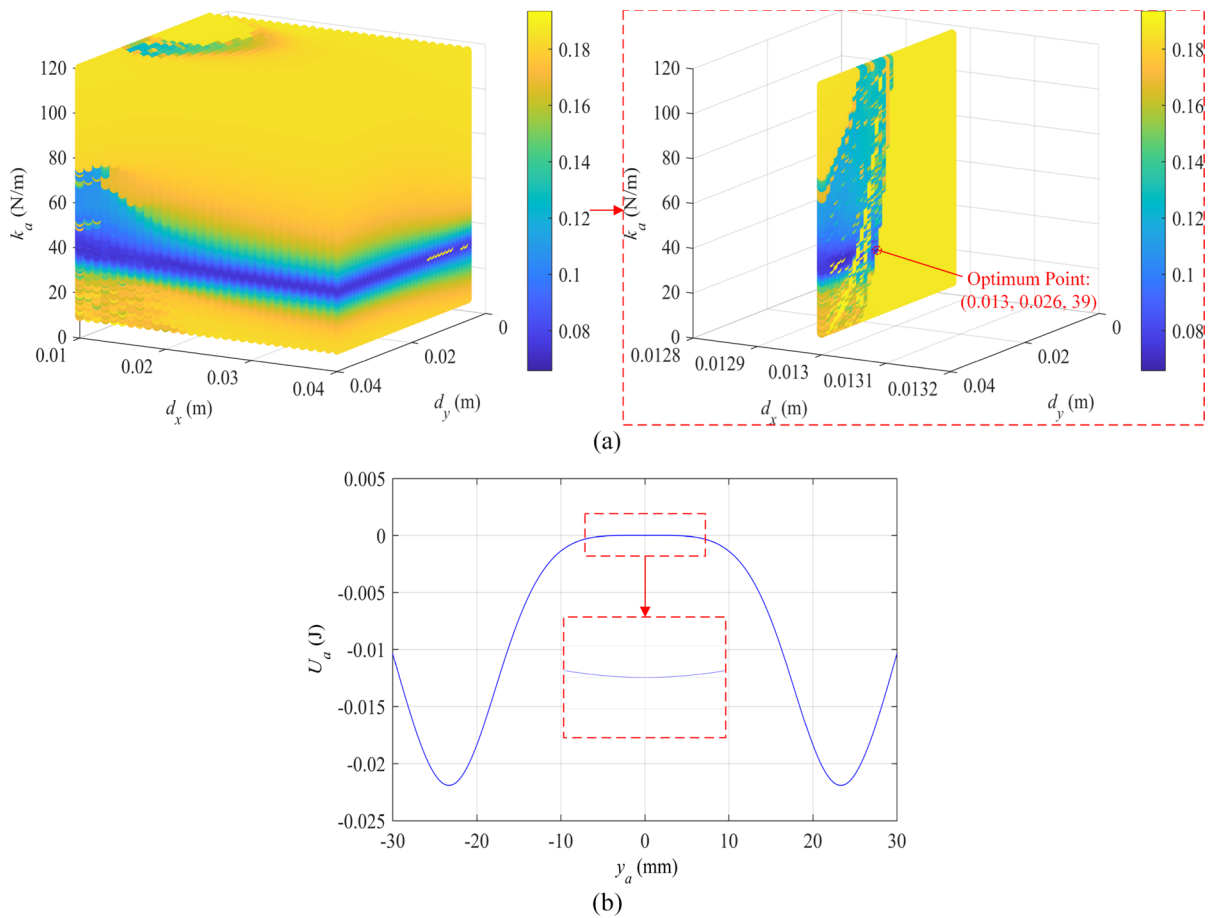


Fig. 29 Optimization results under $q_p = 12$ mm and potential energy of 3AMNVA: **a** contour of P value of 3AMNVA, **b** potential energy of the optimal 3AMNVA

are attached to the primary structure in this paper. To ensure fair comparison, the parameters of 2RMNVA (Masoud et al. [23, 24]) and 3RMNVA (Masoud et al. [25]) are optimized under different excitation levels through exhaustion method. The lower and upper bounds to search optimal parameters are the same as those in Table 4.

The optimization results of 2RMNVA (Masoud et al. [23, 24]) are shown in Fig. 38. Under low-level excitation, the optimal parameters, stable equilibrium and metric of 2RMNVA (Masoud et al. [23, 24]) are $d_x = 0.020$ m, $k_a = 74$ N/m, $q_a = 0.0061$ m and $P = 0.0023$; under intermediate-level excitation, the optimal parameters, stable equilibrium and metric of

2RMNVA (Masoud et al. [23, 24]) are $d_x = 0.022$ m, $k_a = 33$ N/m, $q_a = 0.0091$ m and $P = 0.0232$; under high-level excitation, the optimal parameters, stable equilibrium and metric of 2RMNVA (Masoud et al. [23, 24]) are $d_x = 0.017$ m, $k_a = 34$ N/m, $q_a = 0.0127$ m and $P = 0.1304$. It is worth noting that with the increase of excitation level, the optimized 2RMNVA (Masoud et al. [23, 24]) has outmost two wells with the larger separation and larger depth (Fig. 38d–f).

As shown in Fig. 39, through optimization, the vibration suppression performance of 2RMNVA (Masoud et al. [23, 24]) is improved (Fig. 39a–c and g–i) due to larger inter-well oscillations (Fig. 39d–f).

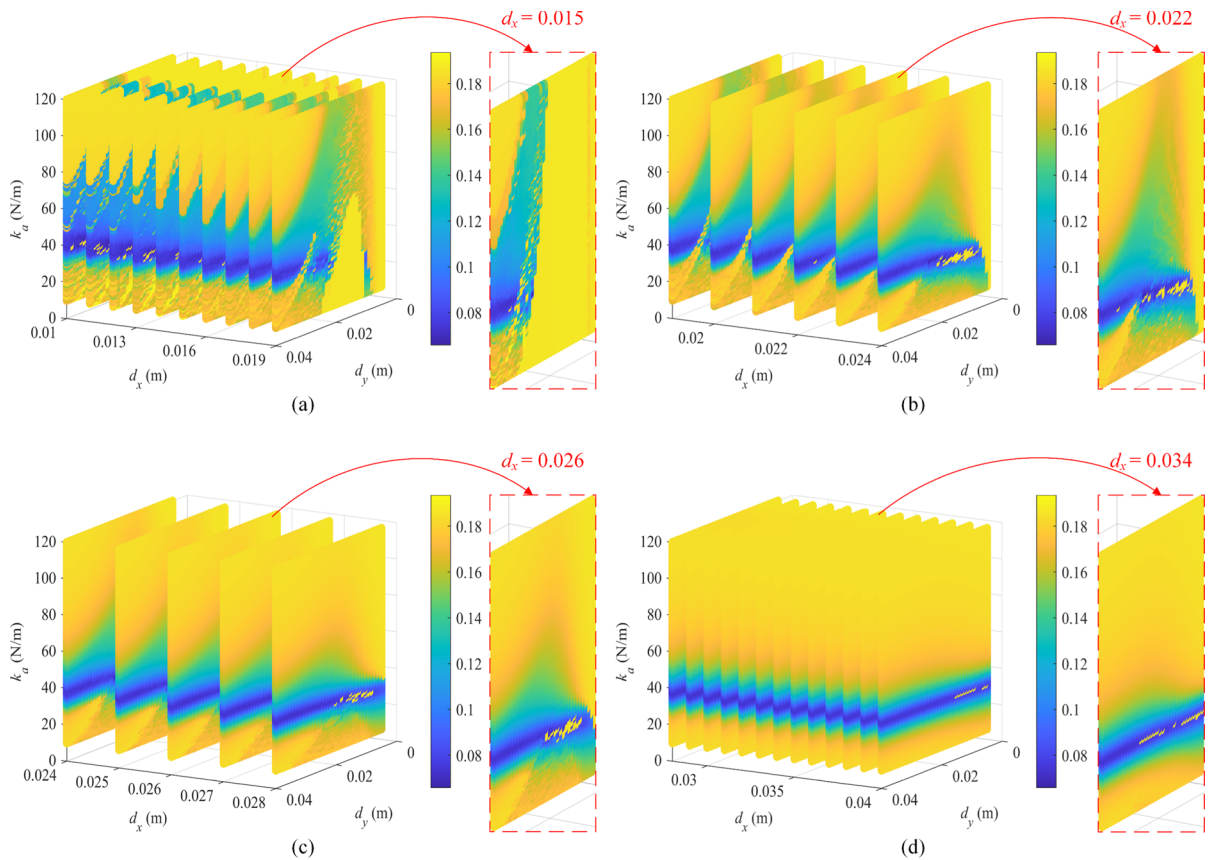


Fig. 30 Contour of P value of 3AMNVA under $q_p = 12$ mm: $d_x \in$ **a** [0.010, 0.019], **b** [0.019, 0.024], **c** [0.024, 0.028], **d** [0.028, 0.040]

The optimization results of 3RMNVA (Masoud et al. [25]) are shown in Fig. 40. Under low-level excitation, the optimal parameters, stable equilibrium and metric of 3RMNVA (Masoud et al. [25]) are $d_x = 0.003$ m, $d_y = 0.025$ m, $k_a = 95$ N/m, $q_a = 0$ m and $P = 0.0021$; under intermediate-level excitation, the optimal parameters, stable equilibrium and metric of 3RMNVA (Masoud et al. [25]) are $d_x = 0.012$ m, $d_y = 0.005$ m, $k_a = 37$ N/m, $q_a = 0$ m and $P = 0.0175$; under high-level excitation, the optimal parameters, stable equilibrium and metric of 3RMNVA (Masoud et al. [25]) are $d_x = 0.012$ m, $d_y = 0.005$ m, $k_a = 46$ N/m, $q_a = 0$ m and $P = 0.1192$. It is worth noting that under the low-excitation level, the optimized 3RMNVA (Masoud et al. [25]) has the middle well with the large depth (Fig. 40d); under the intermediate- and high-level

excitation, the optimized 3RMNVA (Masoud et al. [25]) has the middle well with the small depth and outmost two wells with the large depth (Fig. 40e and f).

As shown in Fig. 41, through optimization, the vibration suppression performance of 3RMNVA (Masoud et al. [25]) improved (Fig. 41a–c and g–i) due to frequent intra-well oscillations (Fig. 41d) and inter-well oscillations with larger amplitude (Fig. 41e, f).

In addition, as shown in Figs. 39a–c, g–i and 41a–c, g–i, the 2RMNVA and 3RMNVA designed in this paper could achieve better vibration suppression than those in Refs. [23–25], particularly under high-level excitation. However, it should be noted that the masses of 2RMNVAs and 3RMNVAs in this paper and Refs.

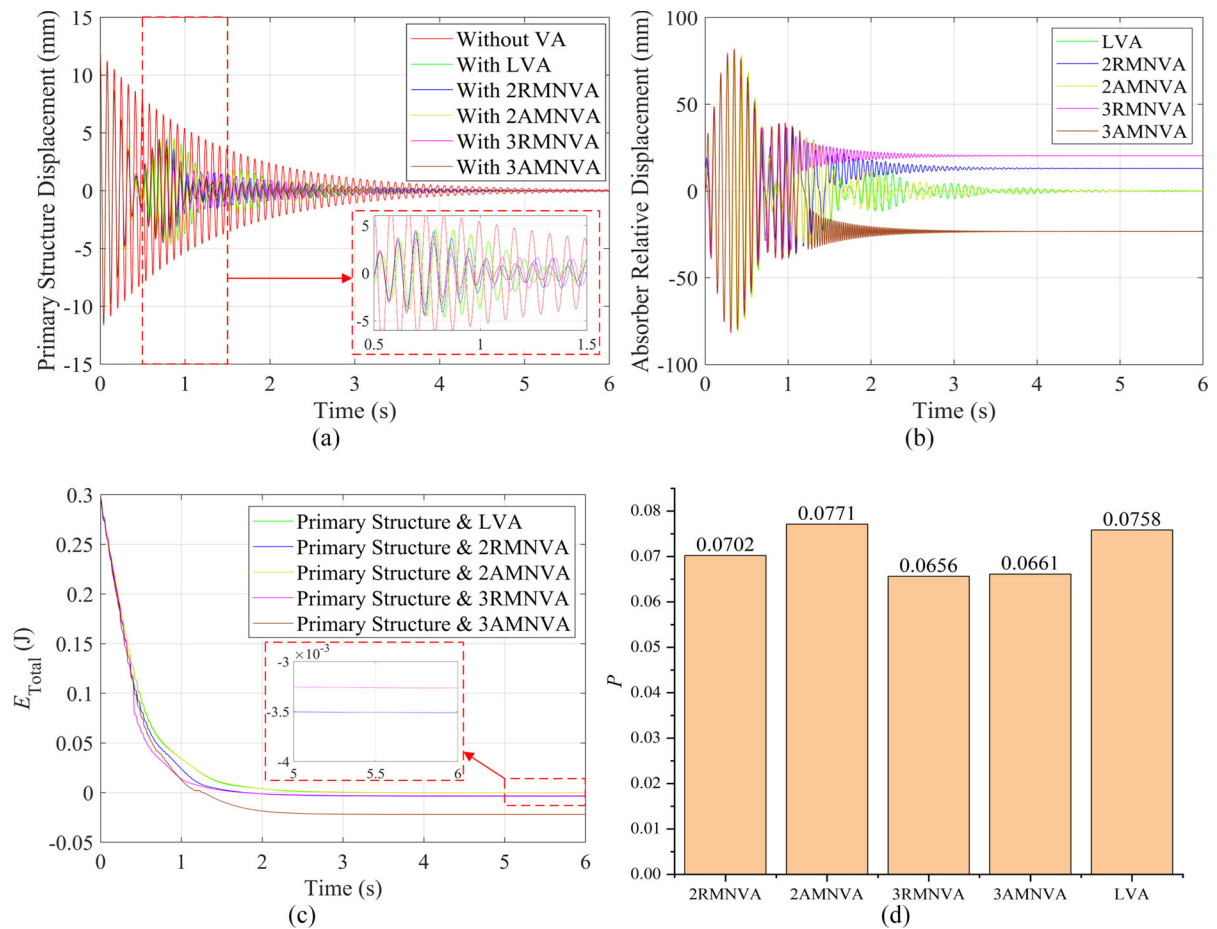


Fig. 31 **a** Displacement of primary structure with optimal LVA and different magnetic NVAs, **b** displacements of optimal LVA and different magnetic NVAs relative to the primary structure, **c**

total energy of primary structure with optimal magnetic NVAs and **d** P of optimal LVA and different magnetic NVAs under $q_p = 12$ mm

[23–25] are different and 2RMNVA and 3RMNVA in Refs. [23–25] possess the piezoelectric transducer.

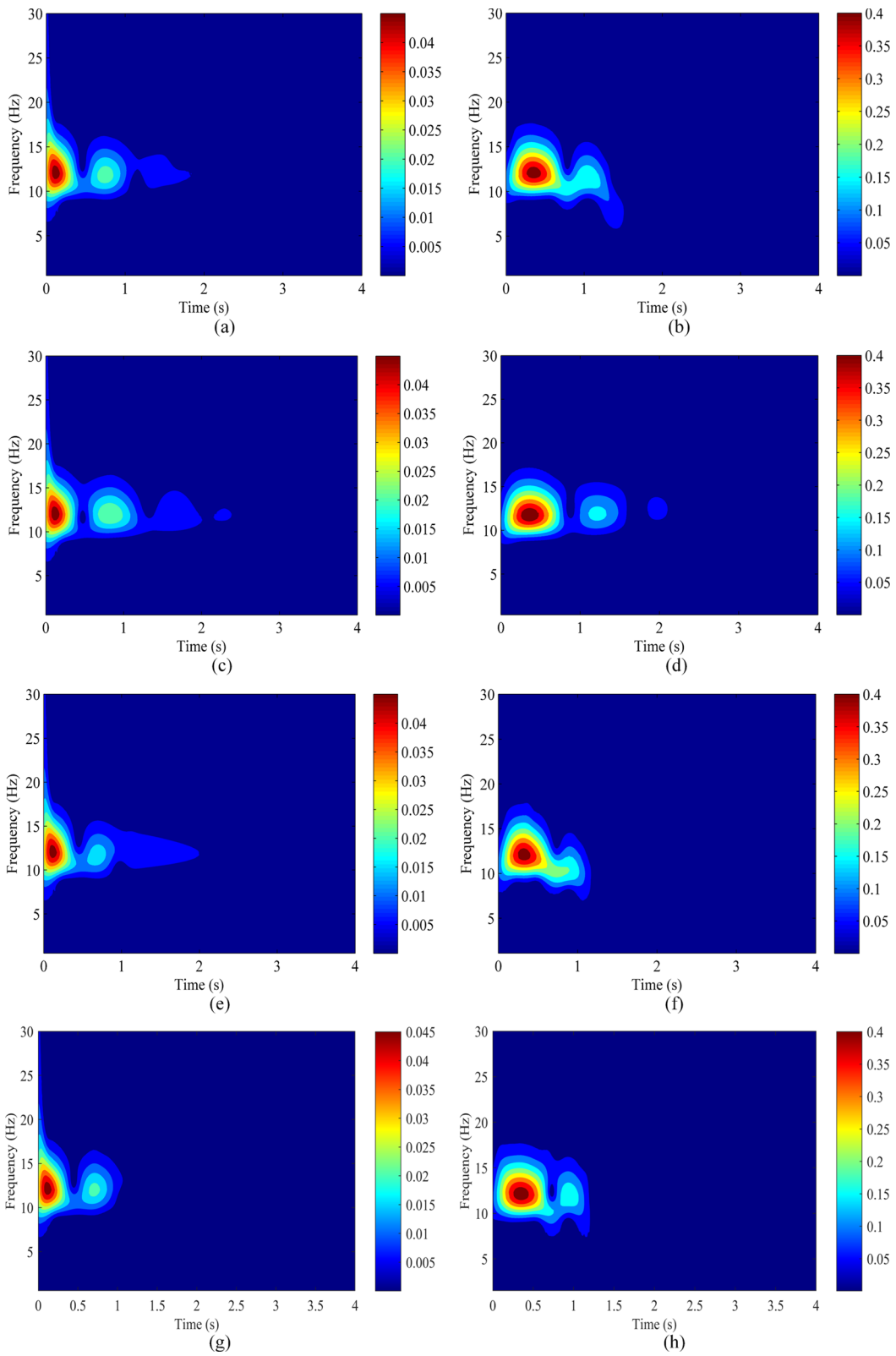
5 Discussions

5.1 Influence of initial position

To explore the influence of initial position, we choose the optimized 3RMNVA and 3AMNVA with tristability obtained under the condition of zero initial position and then perform the simulations by setting

the initial position at a non-zero equilibrium position (for short, non-zero initial position).

As shown in Fig. 42a and d, with the non-zero initial position, the previously optimized 3RMNVA and 3AMNVA can not influence the behavior of the primary structure. According to Fig. 42b, c and e, f, the reason for their worse performance is because they can only execute intra-well oscillations due to the deep outside potential well. To improve their performance, we optimize the 3RMNVA and 3AMNVA again. Different from the previous optimization, in the case of tristable configuration, the 3RMNVA and



◀ **Fig. 32** WT spectra of displacement of primary structure with four optimal magnetic NVAs and the optimal magnetic NVAs under $q_p = 12$ mm: **a, b** 2RMNVA, **c, d** 2AMNVA, **e, f** 3RMNVA, **g, h** 3AMNVA

3AMNVA are initially placed at the non-zero equilibrium position.

The optimization results of 3RMNVA are shown in Fig. 43. The optimal parameters, stable equilibrium and metric of the 3RMNVA are $d_x = 0.010$ m, $d_y = 0.031$ m, $k_a = 49$ N/m, $q_a = 0.03549$ m and $P = 0.0117$ for intermediate-level excitation and $d_x = 0.010$ m, $d_y = 0.032$ m, $k_a = 41$ N/m, $q_a = 0.03688$ m and $P = 0.0610$ for high-level excitation. The optimal 3RMNVAs are the tristable structure

with the deep middle potential well and shallow outside potential well.

The optimization results of 3AMNVA are shown in Fig. 44. The optimal parameters, stable equilibrium and metric of the 3AMNVA are $d_x = 0.010$ m, $d_y = 0.040$ m, $k_a = 74$ N/m, $q_a = 0.03026$ m and $P = 0.0135$ for intermediate-level excitation and $d_x = 0.018$ m, $d_y = 0.033$ m, $k_a = 39$ N/m, $q_a = 0.01990$ m and $P = 0.0669$ for high-level excitation. The optimal 3AMNVAs are the tristable structure with the shallow outside potential well.

The vibration suppression performances of optimized 3RMNVA and 3AMNVA under intermediate- and high-level excitations are shown in Fig. 45. All the optimized 3RMNVAs and 3AMNVAs show the good vibration suppression performance (Fig. 45a, b,

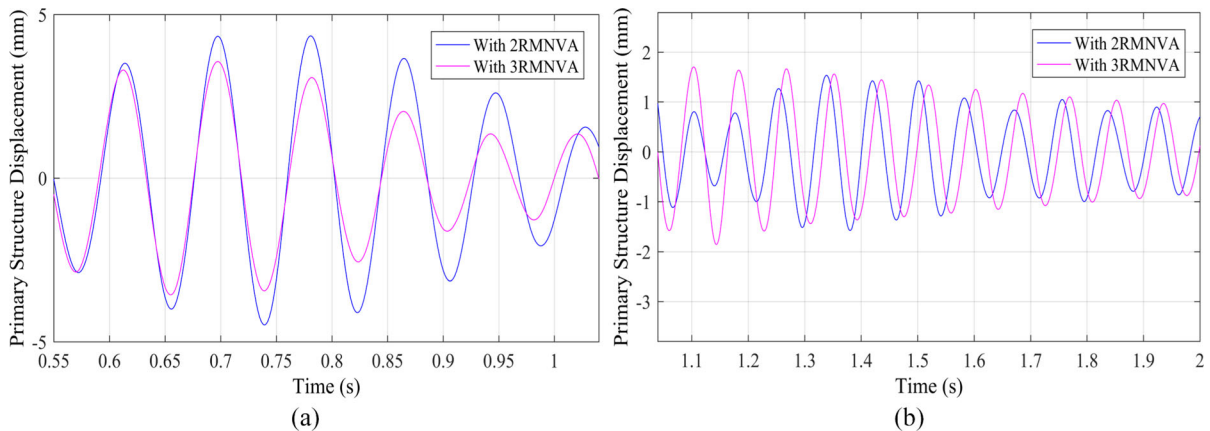


Fig. 33 Displacement of primary structure with the optimal 2RMNVA and 3RMNVA under $q_p = 12$ mm: $t \in$ **a** [0.55, 1.04] and **b** (1.04, 2.00]

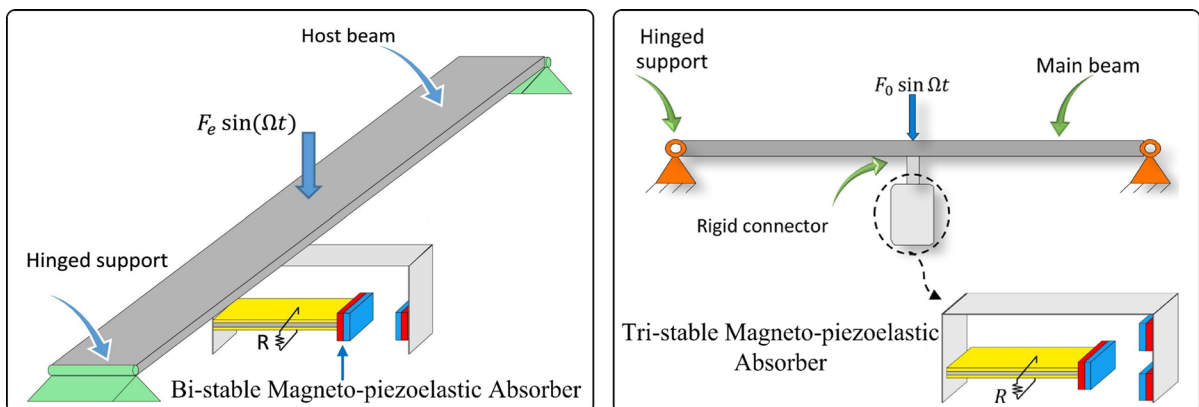


Fig. 34 Schematic of a coupled system composed of a main simply-supported beam and a magneto-piezoelectric absorber (left: bistable absorber; right: tristable absorber). (Figures are adapted from Refs [23–25].)

Table 3 System parameters of the primary structure and the magnetic NVAs in Refs. [23–25]

Parameter	Value
Mass of the primary structure m_p	0.1794 kg
Stiffness of the primary structure k_p	1341.8599 N/m
Damping ratio of the primary structure ζ_p	0.010
Mass of the magnetic NVA m_a	0.0051 kg
Stiffness of the primary structure k_a	50.0825 N/m
Damping ratio of the magnetic NVA ζ_a	0.010
Length of the absorber beam L	0.07 m
Magnet length a	0.00275 m
Magnet area S	0.0002 m ²
Horizontal magnet separation distance d_x of bistable absorber	0.02275 m
Horizontal magnet separation distance d_x of tristable absorber	0.01925 m
Half value of vertical magnet separation distance d_y of tristable absorber	0.007 m
Electromechanical coupling coefficient θ	1.5655e-4 N/V
Capacitance of piezoelectric transducer C	5.2938e-8 F
Load resistance R	1 M Ω

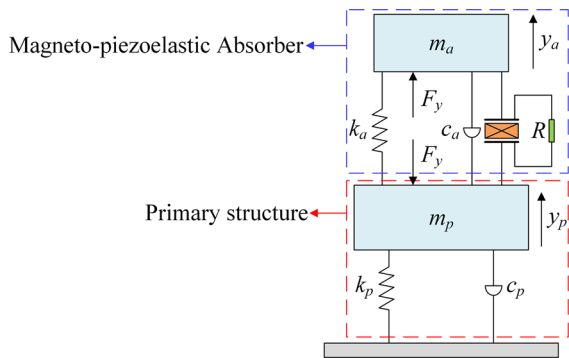


Fig. 35 Lumped parameter 2DOF model of the system with the bistable/tristable absorber in Refs. [23–25]

e, f) due to the strong cross-well oscillations (Fig. 45c and d). The reason for the strong cross-well oscillations is because the swallow outside potential wells (Figs. 43c, d and 44c, d) are beneficial for the optimized 3RMNVA and 3AMNVA to escape from the initial potential well.

According to the simulation results above, the initial position set at zero or non-zero equilibrium position can affect the performance and optimization

Table 4 Lower and upper bounds for searching optimal parameters of magnetic NVAs in Refs. [23–25]

Optimization bounds	Value
$[d_{x_min}, d_{x_max}]$	[0.003, 0.040] m
$[d_{y_min}, d_{y_max}]$	[0.005, 0.040] m
$[k_{a_min}, k_{a_max}]$	[10, 120] N/m

results of tristable magnetic NVAs. Because the cross-well oscillations are conducive for vibration suppression, the parameter optimization should provide the potential energy curve that eases the multistable magnetic NVA to overcome the potential well barrier.

5.2 Magnetic NVA configuration preference

Based on the simulation results under different levels of transient excitations in Sect. 3, some principles for magnetic NVA can be obtained to design and optimize such absorbers. Here, the bounds for optimization are $d_x \in [0.010, 0.040]$ (m), $d_y \in [0.005, 0.040]$ (m),

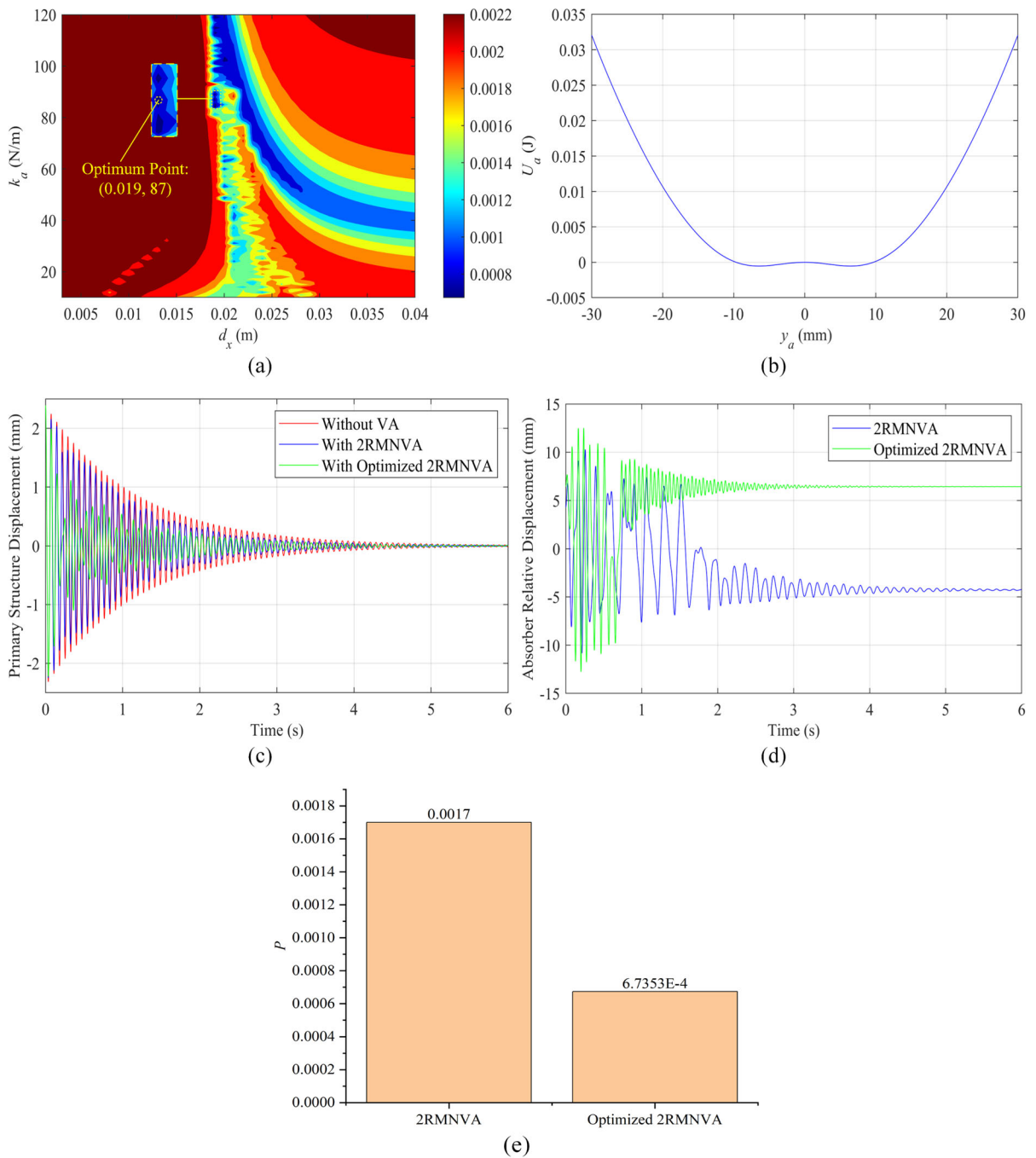


Fig. 36 Optimization results for the system in Masoud et al. [23, 24] under $q_p = 2.4$ mm: **a** Contour of P value of 2RMNVA, **b** potential energy of the optimal 2RMNVA, **c** comparison of the

primary structure displacement **d** comparison of the absorber displacement relative to the primary structure and **e** comparison of P values of 2RMNVA and optimized 2RMNVA

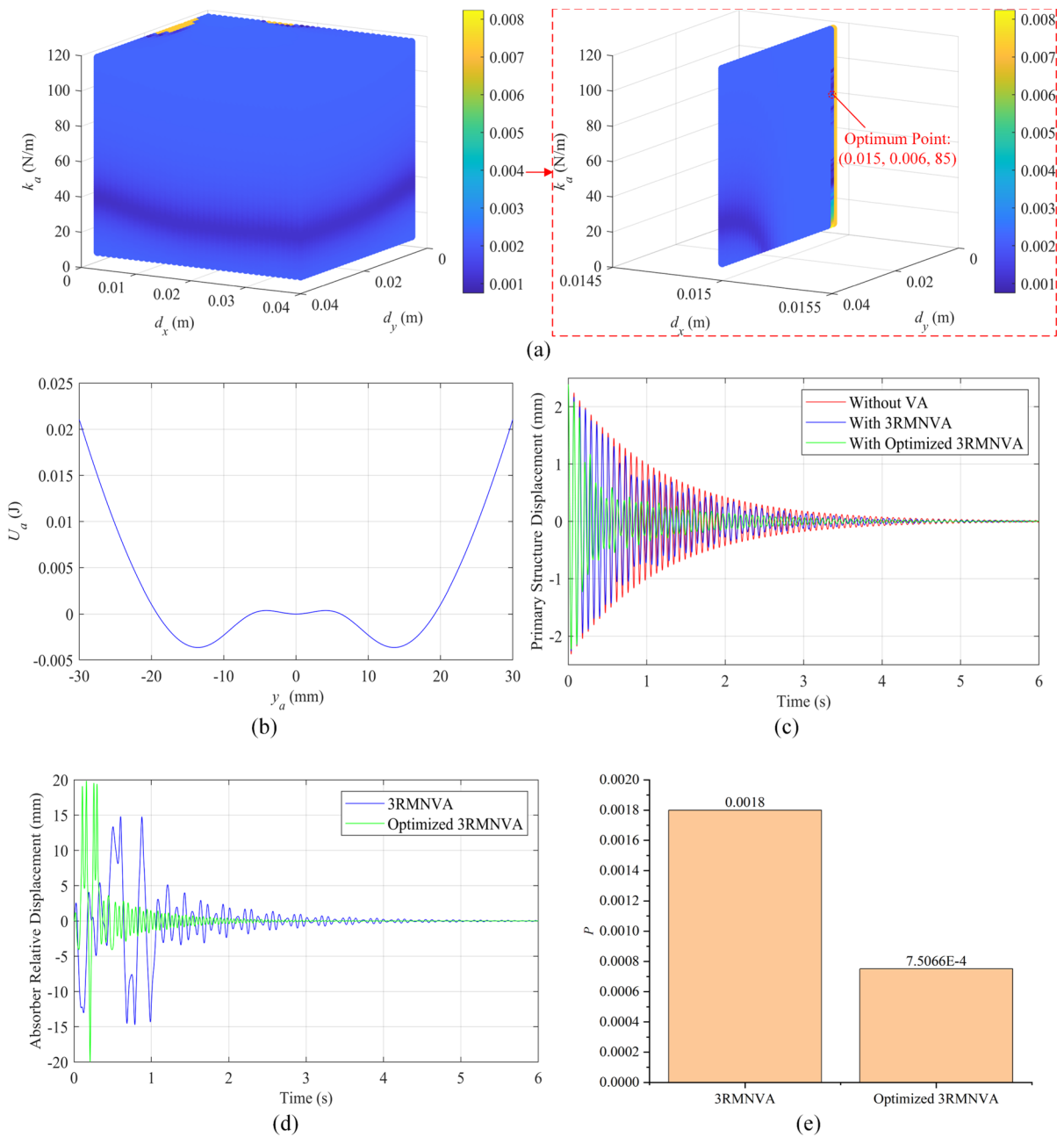


Fig. 37 Optimization results for the system in Masoud et al. [25] under $q_p = 2.4$ mm: **a** Contour of P value of 3RMNVA, **b** potential energy of the optimal 3RMNVA, **c** comparison of the

primary structure displacement **d** comparison of the absorber displacement relative to the primary structure and **e** Comparison of P values of 3RMNVA and optimized 3RMNVA

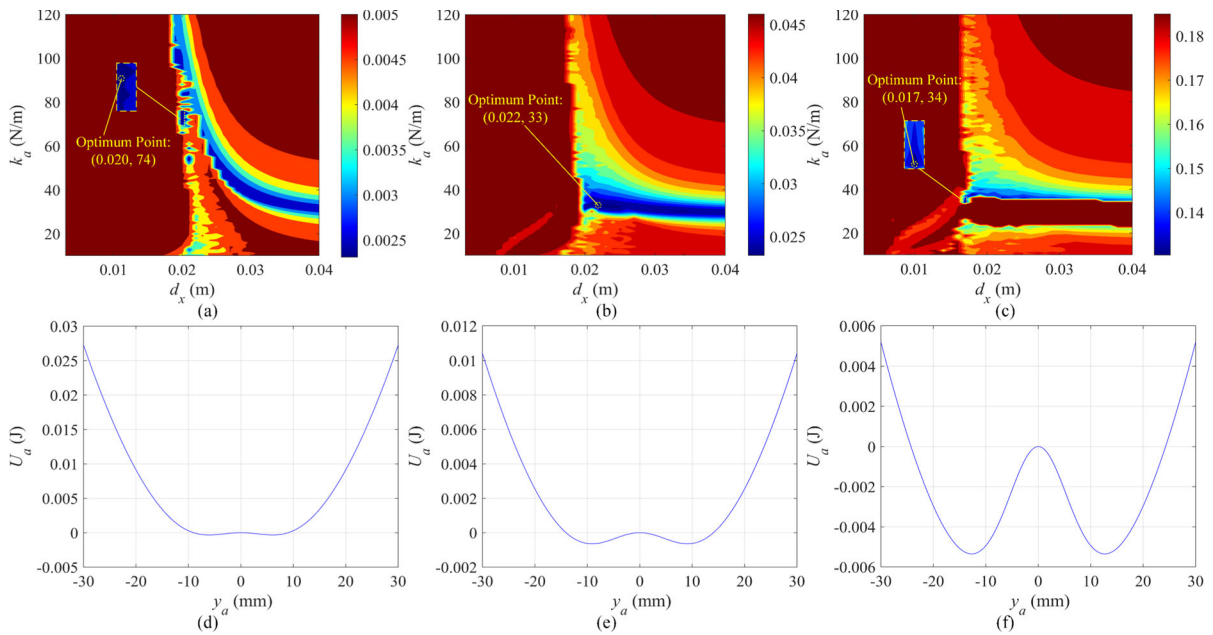


Fig. 38 Optimization results of 2RMNVA (Masoud et al. [23, 24]) under different excitation levels: Contour of P value of 2RMNVA (Masoud et al. [23, 24]) under **a** low-level excitation, **b** intermediate-level excitation, **c** high-level excitation;

Potential energy of the optimized 2RMNVA (Masoud et al. [23, 24]) under **d** low-level excitation, **e** intermediate-level excitation, **f** high-level excitation

$k_a \in [10, 120]$ (N/m). For 2RMNVA, under low-level excitation, the magnet separation distance should be intermediate and the cantilever stiffness should be high ($d_x = 0.022$ m, $k_a = 109$ N/m); under intermediate-level excitation, the magnet separation distance should be high and the cantilever stiffness should be slightly lower than intermediate stiffness ($d_x = 0.036$ m, $k_a = 40$ N/m); under high-level excitation, the magnet separation distance should be intermediate and the cantilever stiffness should be slightly lower than intermediate stiffness ($d_x = 0.022$ m, $k_a = 39$ N/m). For 2AMNVA, because its characteristics and performance are similar to LVA or even worse under different levels of initial conditions, the horizontal magnet separation distance should be as high as possible to reduce the effects of nonlinear magnetic force and the value of cantilever stiffness should let the nature frequency of 2AMNVA be close to that of primary structure. Hence, there is no

need to use 2AMNVA if we have to choose one from 2AMNVA and LVA. For 3RMNVA, under low-level excitation, the horizontal separation distance between two fixed magnets should be intermediate, the vertical magnet separation distance should be low and the cantilever stiffness should be high ($d_x = 0.024$ m, $d_y = 0.007$ m, $k_a = 98$ N/m); under intermediate- and high-level excitations, the horizontal magnet separation distance should be slightly lower than the intermediate horizontal distance, the vertical magnet separation distance should be low and the cantilever stiffness should be slightly lower than intermediate stiffness ($d_x = 0.016$ m, $d_y = 0.007$ m, $k_a = 51$ N/m for intermediate-level and $d_x = 0.018$ m, $d_y = 0.009$ m, $k_a = 40$ N/m for high-level). For 3AMNVA, under low-level excitation, the horizontal magnet separation distance should be intermediate, the vertical magnet separation distance should be slightly higher than low vertical distance and the cantilever

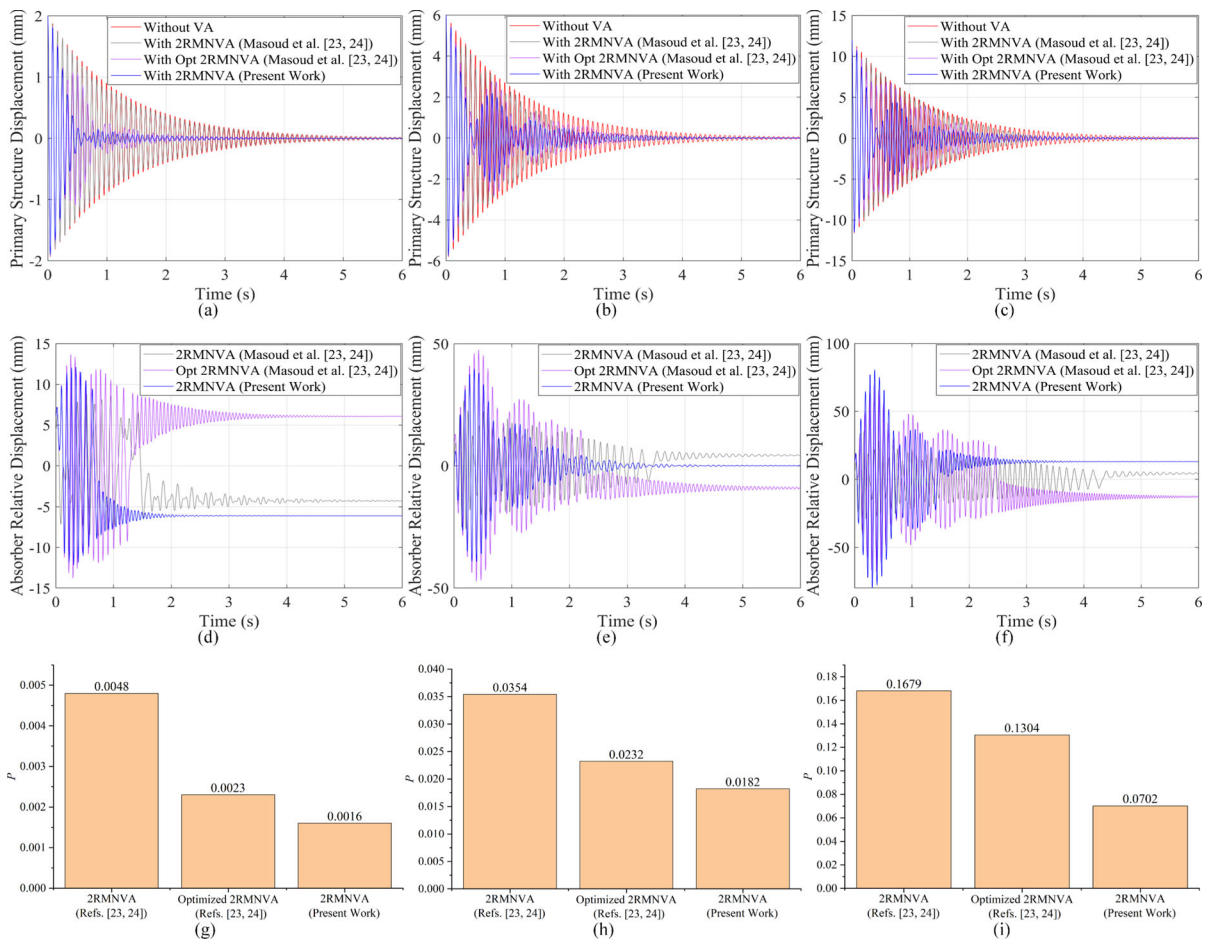


Fig. 39 Vibration performance comparison of 2RMNVA under different excitation levels: Displacement of primary structure with 2RMNVA under **a** low-level excitation, **b** intermediate-level excitation, **c** high-level excitation; Displacement of 2RMNVA relative to the primary structure under **d** low-level

excitation, **e** intermediate-level excitation, **f** high-level excitation; Comparison of P values of different 2RMNVA under **g** low-level excitation, **h** intermediate-level excitation, **i** high-level excitation

stiffness should be intermediate ($d_x = 0.022$ m, $d_y = 0.014$ m, $k_a = 62$ N/m); under intermediate- and high-level excitation, the horizontal magnet separation distance should be low, the vertical magnet separation distance should be intermediate and the cantilever stiffness should be slightly lower than intermediate stiffness ($d_x = 0.010$ m, $d_y = 0.027$ m, $k_a = 50$ N/m for intermediate-level and $d_x = 0.013$ m, $d_y = 0.026$ m, $k_a = 39$ N/m for high-level).

Under low-level excitation, the optimized 2RMNVA (weak bistability), 3RMNVA (monostability) and 3AMNVA (weak bistability) show similar performance. As shown in Fig. 46, the advantage of the tristability becomes obvious with the increase of excitation level (when q_p reaches 4 mm), under which, cross-well oscillations with the further separation distance and further depth of the outmost two wells in 3RMNVA and 3AMNVA can significantly help

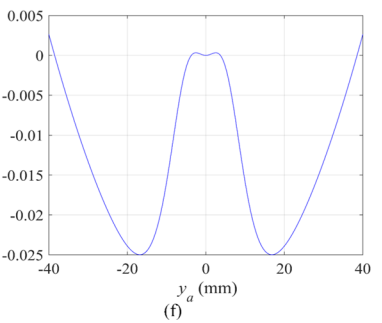
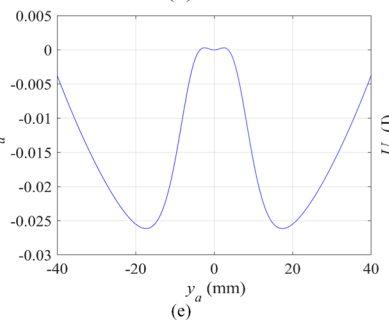
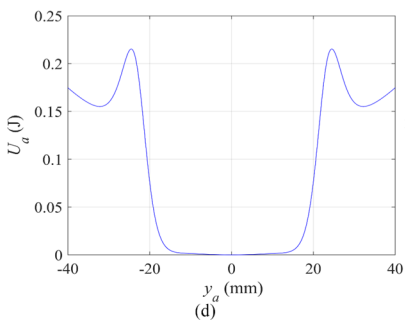
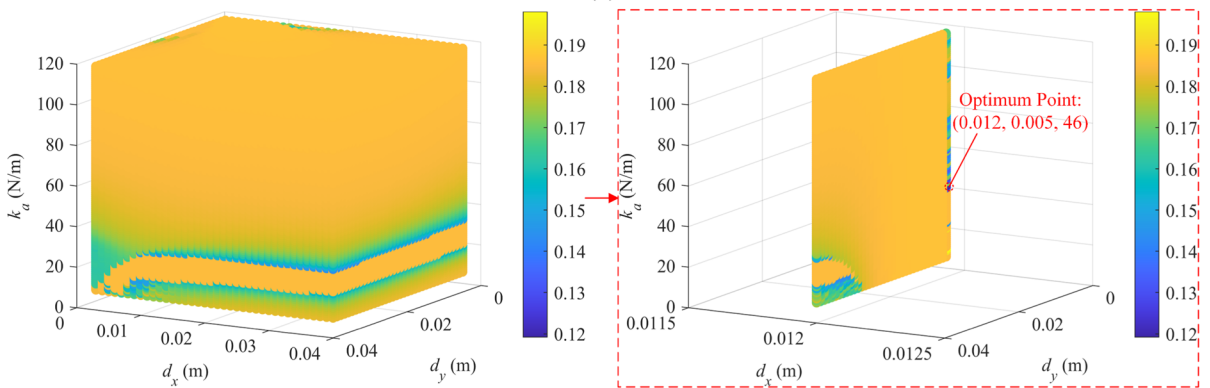
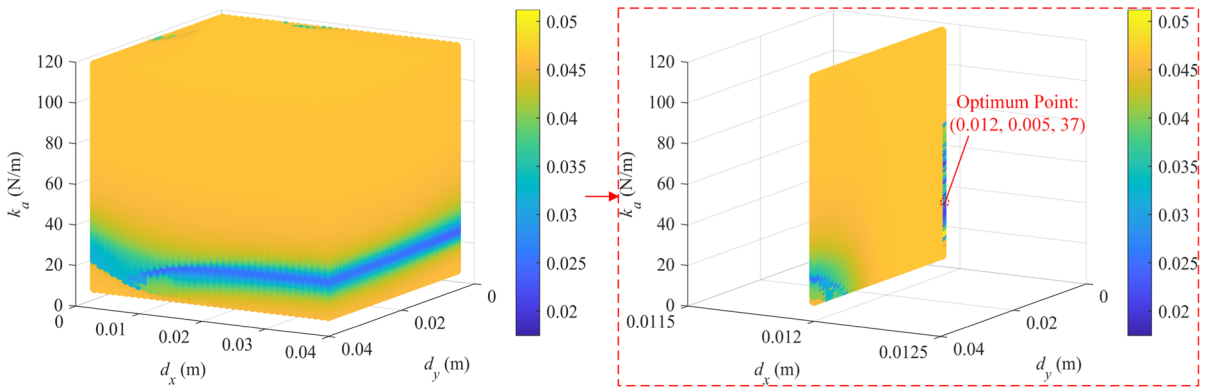
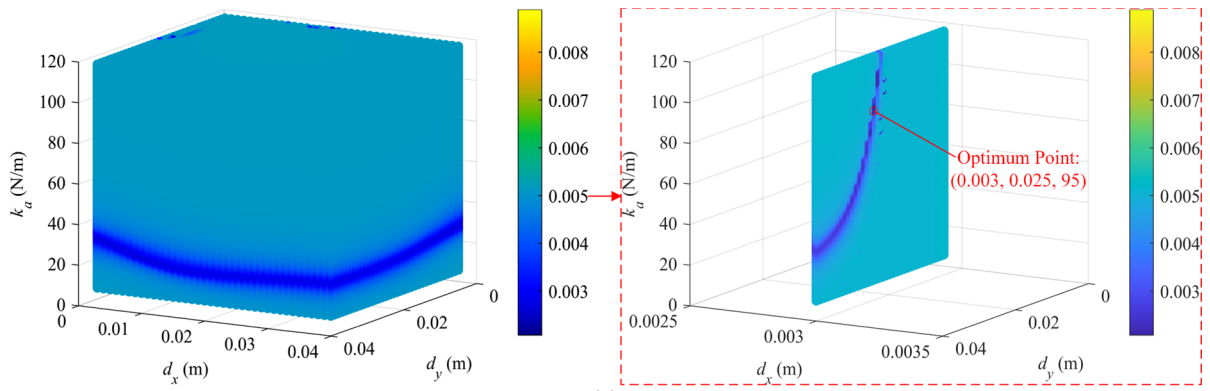


Fig. 40 Optimization results of 3RMNVA (Masoud et al. [25]) under different excitation levels: Contour of P value of 3RMNVA (Masoud et al. [25]) under **a** low-level excitation, **b** intermediate-level excitation, **c** high-level excitation; Potential energy of the optimized 3RMNVA (Masoud et al. [25]) under **d** low-level excitation, **e** intermediate-level excitation, **f** high-level excitation

reduce vibrations. Under intermediate- and high-level excitation, the advantage of 3RMNVA and 3AMNVA with tristability is evident. To ensure the good performance of a magnetic NVA under different excitation levels, it is determined that the 3RMNVA and 3AMNVA with the optimized multi-stability are the preferred option.

6 Conclusions

In this paper, the transient vibration suppression performance of nonlinear vibration absorber (NVA) with two repulsive magnets (2RMNVA), two attractive magnets (2AMNVA), three repulsive magnets (3RMNVA) and three attractive magnets (3AMNVA) and linear vibration absorber (LVA) are compared. Based on the dipole-dipole model of magnets, the dynamic models of system containing different NVAs under different transient excitation levels are established, and the cantilever beam stiffness and the distance between magnets of NVAs are optimized and transient performance and the rate of energy

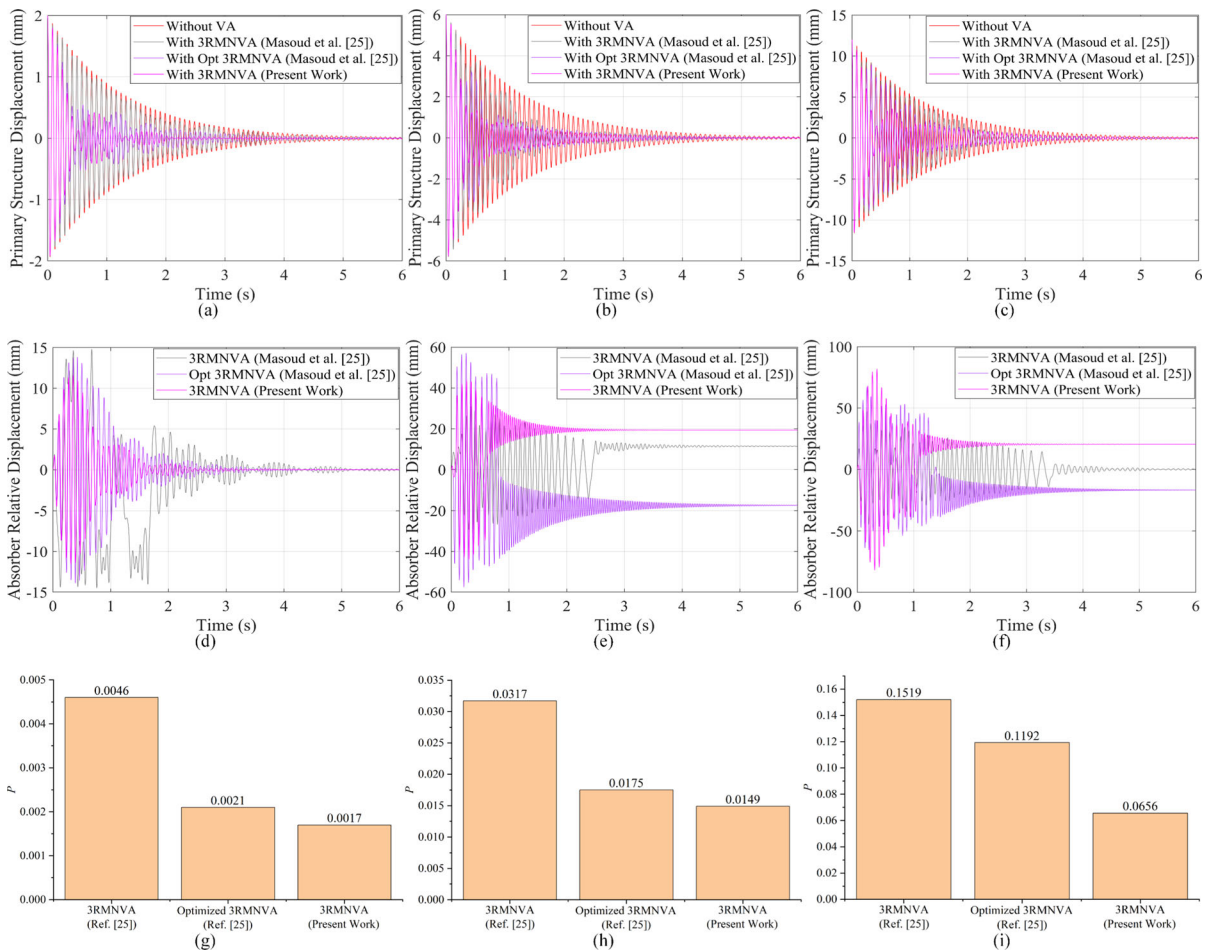


Fig. 41 Vibration performance comparison of 3RMNVA under different excitation levels: Displacement of primary structure with 3RMNVA under **a** low-level excitation, **b** intermediate-level excitation, **c** high-level excitation; Displacement of 3RMNVA relative to the primary structure under **d** low-level

excitation, **e** intermediate-level excitation, **f** high-level excitation; Comparison of P different 3RMNVA under **g** low-level excitation, **h** intermediate-level excitation, **i** high-level excitation

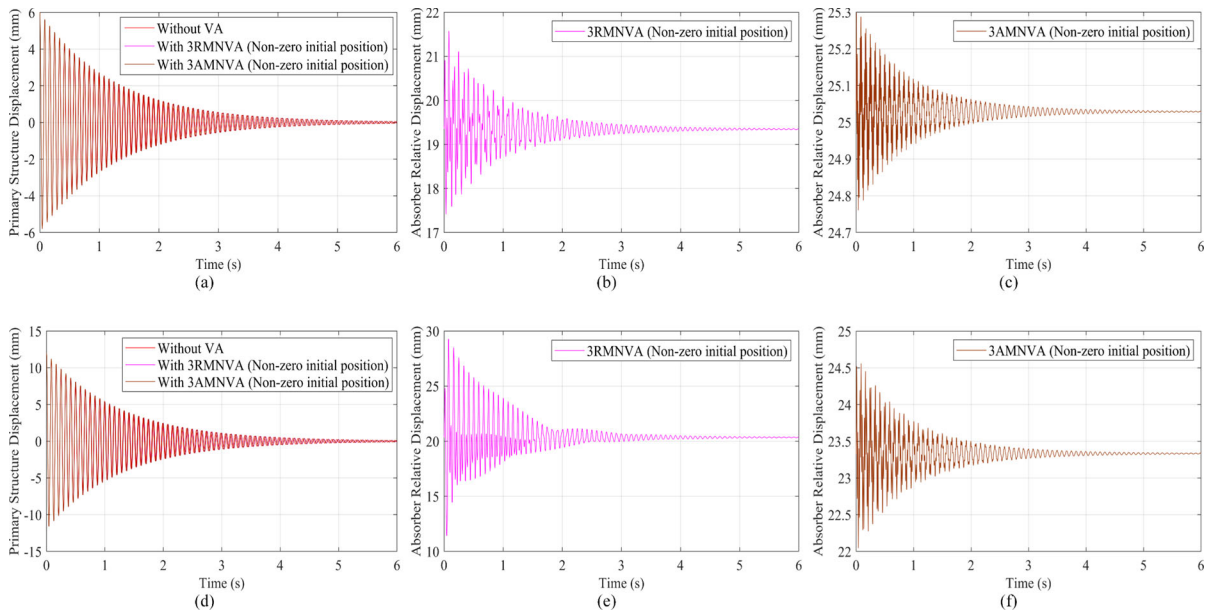


Fig. 42 Performance of previously optimized tristable 3RMNVA/3AMNVA placed at non-zero initial position. Intermediate-level excitation: **a** displacement of primary structure with 3RMNVA/3AMNVA, displacements of

b 3RMNVA and **c** 3AMNVA relative to the primary structure. High-level excitation: **d** displacement of primary structure with 3RMNVA/3AMNVA, displacements of **e** 3RMNVA and **f** 3AMNVA relative to the primary structure

dissipation are also demonstrated by wavelet transform. The main findings are summarized as follows:

- (1) According to the optimization results under different excitation levels, for different magnetic NVAs, the strong vibration performance only exists in limited parameter sets, indicating that selecting the appropriate parameters is crucial to achieve efficient transient vibration suppression performance.
- (2) Under different excitation levels, the characteristics and vibration performance of the optimal 2AMNVA are similar to or even worse than that of LVA, indicating that the arrangement of two attractive magnets should be avoided in the design of magnetic NVA.
- (3) Under different excitation levels, the optimal 2RMNVA, 2AMNVA, 3RMNVA and 3AMNVA all produce 1:1 resonance with the primary structure near its natural frequency.
- (4) According to the optimized results and wavelet transform of the transient responses of different magnetic NVAs, it is found that the bistable 2RMNVA, monostable 3RMNVA and bistable 3AMNVA have similar performance under low-level excitation but the tristable 3RMNVA and 3AMNVA outperform its counterparts with the increase of excitation. The outstanding vibration performance of the optimal magnetic NVAs is due to their oscillations of crossing the outmost two wells with the further separation distance and further depth. To account for the performance under different excitation levels, 3RMNVA and 3AMNVA are the preferred configurations for magnetic NVA.
- (5) The verification and comparison with reported literature demonstrate that the optimization through exhaustion method improves the vibration suppression performance of other reported designs and can be applied to other types of

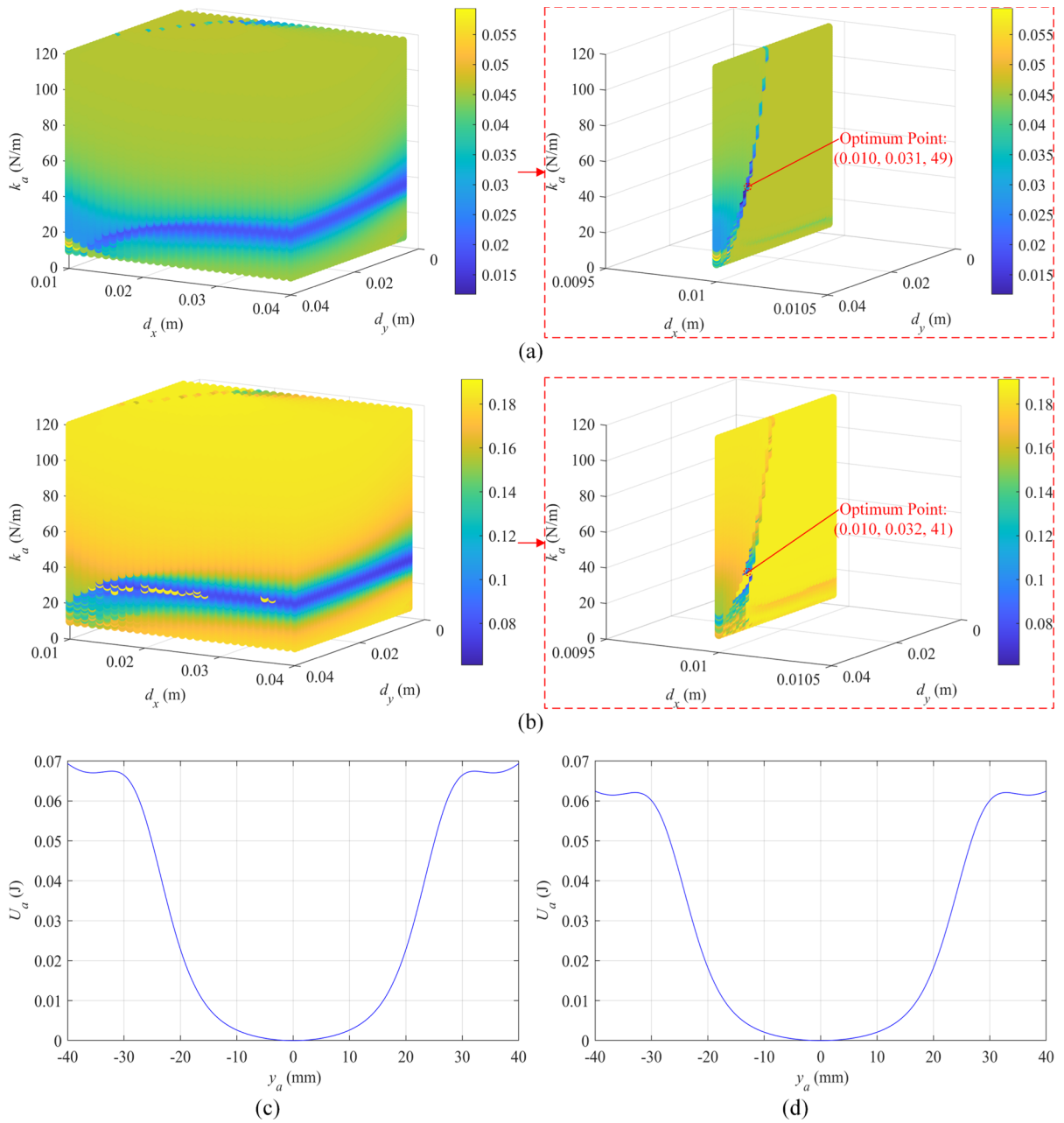


Fig. 43 Optimization results of 3RMNVA under **a** intermediate-level and **b** high-level excitations. Potential energy of the optimal 3RMNVA under **c** intermediate-level and **d** high-level excitations

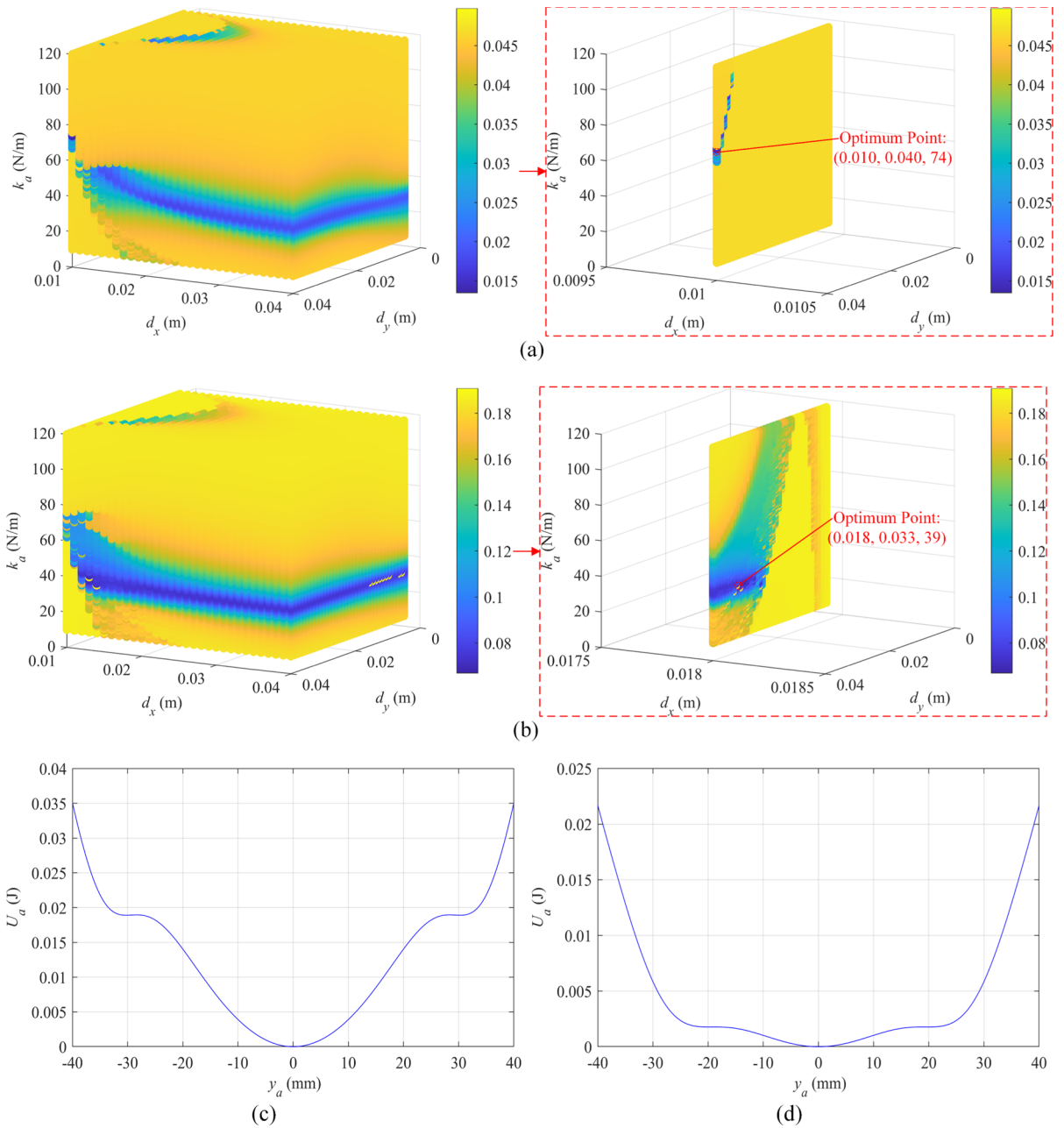


Fig. 44 Optimization results of 3AMNVA under **a** intermediate-level and **b** high-level excitations. Potential energy of the optimal 3AMNVA under **c** intermediate-level and **d** high-level excitations

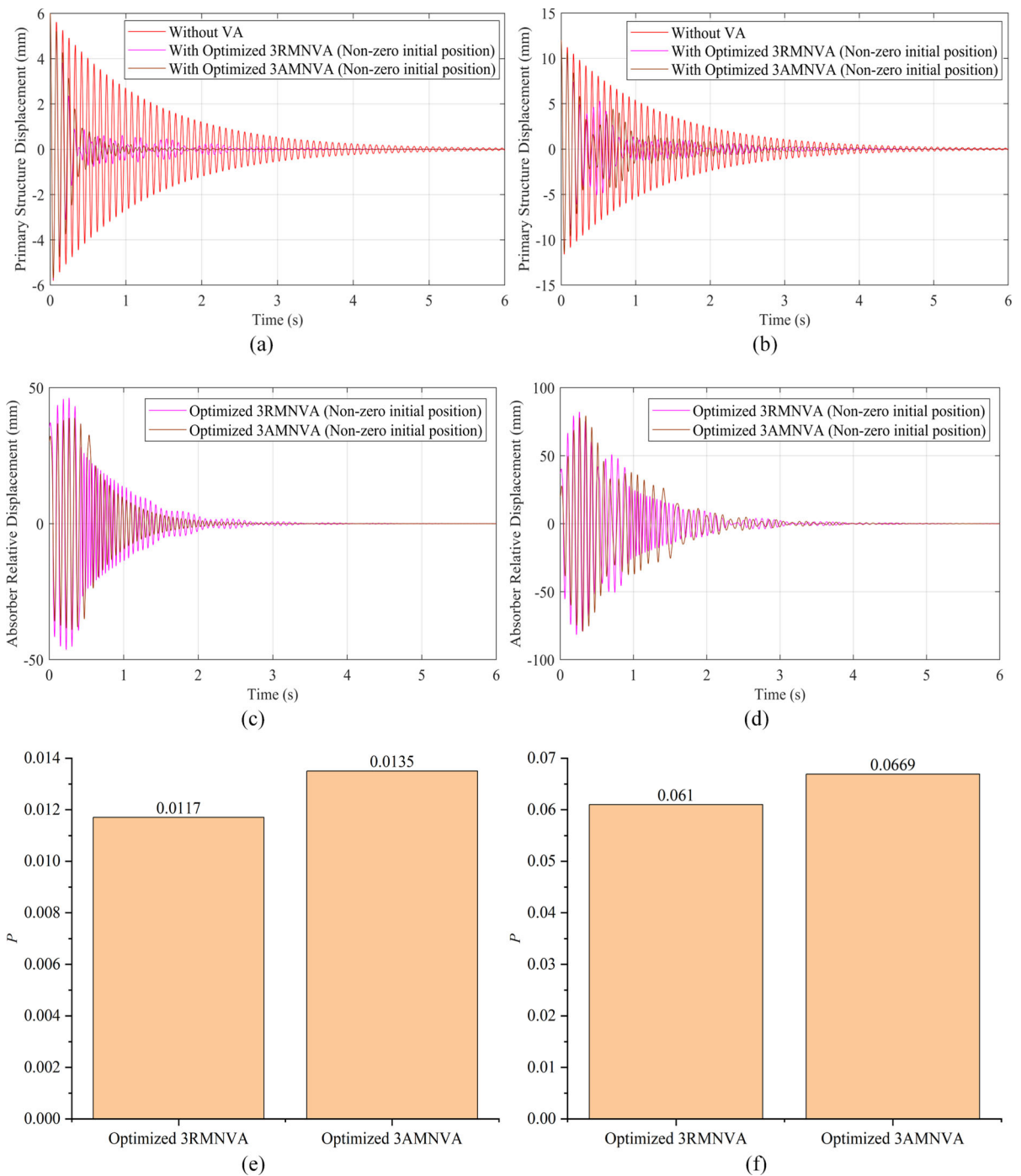


Fig. 45 Vibration performances of optimized 3RMNVA and 3AMNVA under different excitation levels: displacement of primary structure with optimized 3RMNVA and 3AMNVA under **a** intermediate-level and **b** high-level excitations; displacement of optimized 3RMNVA and 3AMNVA relative

to the primary structure under **c** intermediate-level and **d** high-level excitations; comparison of P values of optimized 3RMNVA and 3AMNVA under **e** intermediate-level and **f** high-level excitations

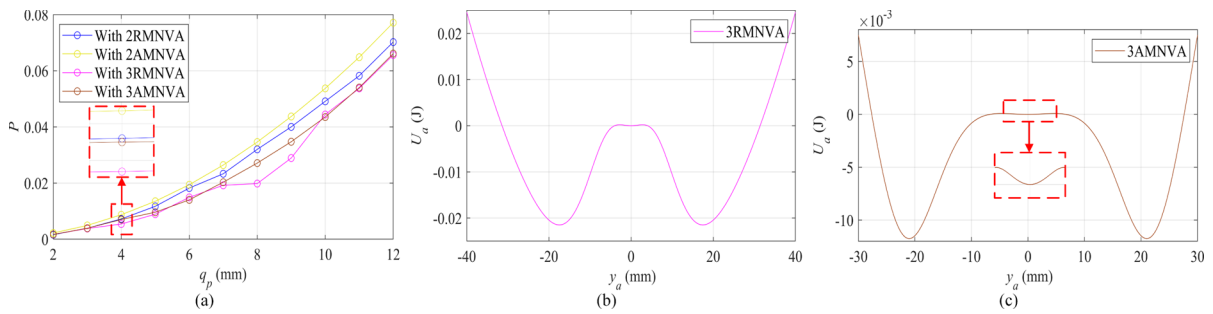


Fig. 46 **a** P value of primary structure with optimal magnetic NVAs under different excitation levels; Potential energy of optimal **b** 3RMNVA and **c** 3AMNVA under $q_p = 4$ mm

nonlinear absorbers with linear and nonlinear stiffnesses.

The comprehensive comparative study in this work provides the optimization approach and guidelines to design the nonlinear vibration absorbers for efficient transient vibration suppression.

Acknowledgements This work was financially supported by a PhD scholarship from the China Scholarship Council (No. 202106080017).

Funding Open Access funding enabled and organized by CAUL and its Member Institutions. The authors have not disclosed any funding.

Data availability The data supporting the findings of this paper are available from the corresponding author on request.

Declarations

Conflict of interest None.

Open Access This article is licensed under a Creative Commons Attribution 4.0 International License, which permits use, sharing, adaptation, distribution and reproduction in any medium or format, as long as you give appropriate credit to the original author(s) and the source, provide a link to the Creative Commons licence, and indicate if changes were made. The images or other third party material in this article are included in the article’s Creative Commons licence, unless indicated otherwise in a credit line to the material. If material is not included in the article’s Creative Commons licence and your

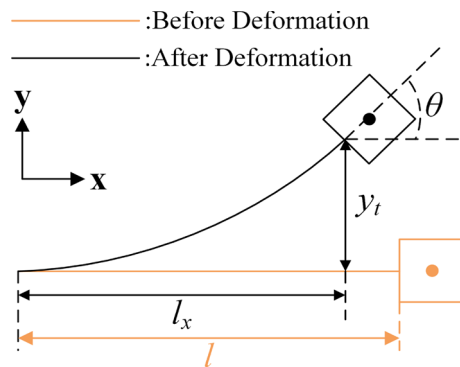


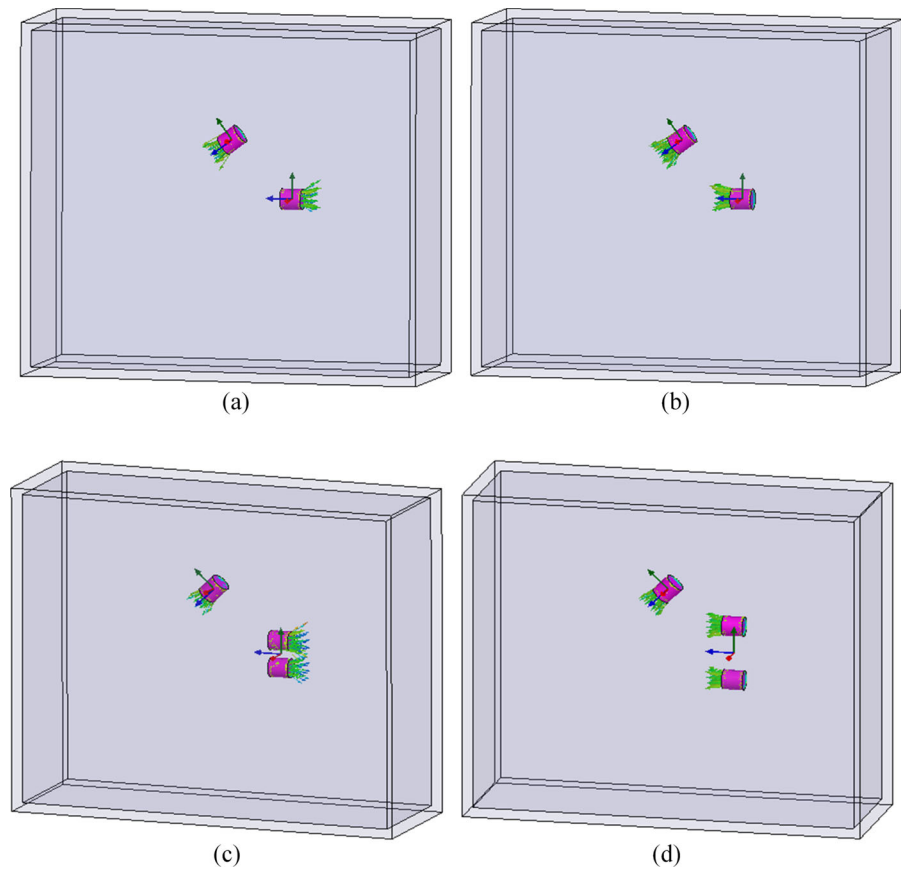
Fig. 47 Motion trajectory of cantilever beam

intended use is not permitted by statutory regulation or exceeds the permitted use, you will need to obtain permission directly from the copyright holder. To view a copy of this licence, visit <http://creativecommons.org/licenses/by/4.0/>.

Appendix 1

In this paper, the dipole–dipole model was used to calculate the magnetic force with the assumption of small displacement and rotation, which has been reported in Refs. [26, 29, 34, 38]. Under the assumption of small displacement and rotation, the proposed model of the beam is a simplified model of a fixed-free beam which does not account for the exact tip rotation.

Fig. 48 Finite element models: **a** 2RMNVA, **b** 2AMNVA, **c** 3RMNVA and **d** 3AMNVA



It is worth noting that although the magnetic force is calculated with the assumption of small displacement and rotation, it is also applied to the high displacement scenarios in some Refs. [26, 29]. To verify the effectiveness of the magnetic force model used in this paper, the finite element analysis using ANSYS Maxwell is carried out.

Considering the beam deformation, as shown in the Fig. 47, the trajectory method from the Refs. [32, 33] is used to get the position and rotation at the tip of the cantilever beam with the magnet:

$$l_x = \frac{l}{\frac{\pi^2 y_t^2}{12l^2} + 1} \tag{A1}$$

$$\theta = \arcsin\left(\frac{\pi y_t}{2l(1 - \cos\frac{\pi l_x}{2l})} \sin\left(\frac{\pi l_x}{2l}\right)\right) \tag{A2}$$

where l_x is the length of cantilever beam in x direction, l is the original length of cantilever beam, y_t is the displacement of the free end of the cantilever beam in the y direction, θ is the rotational angle of the free end of the cantilever beam.

Based on the results from Eqs. (A1) and (A2), the position and rotation angle of tip magnet corresponding to displacement in the y direction are obtained. Then, as shown in Fig. 48, the 3D models of 2RMNVA, 2AMNVA, 3RMNVA and 3AMNVA magnet arrangements are built in ANSYS Maxwell to calculate their magnetic forces. The magnets length is $a = 0.010$ m, diameter $D_m = 0.010$ m and residual flux density $B_r = 1.26$ T.

The results of ANSYS Maxwell are shown in Fig. 49. From Fig. 49, it is noted that the discrepancy between the magnetic force calculated using our

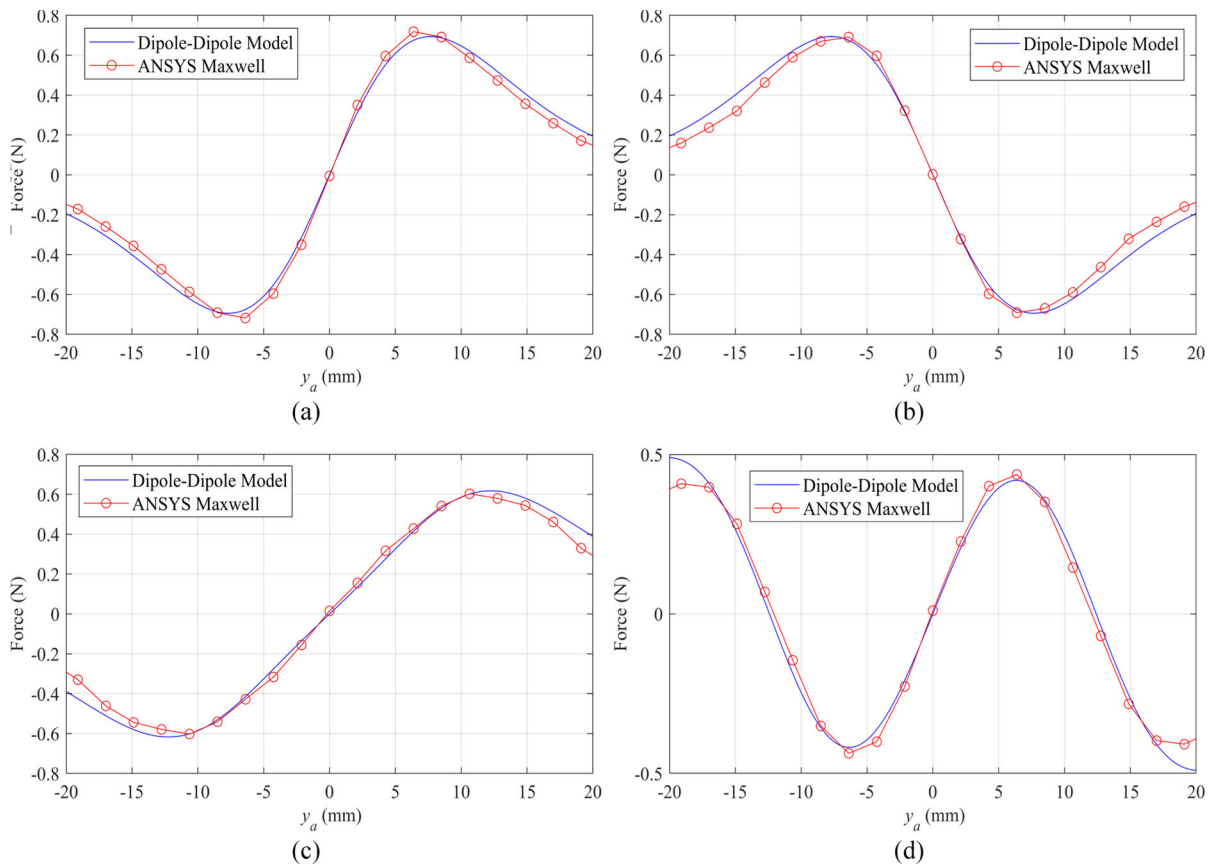


Fig. 49 Comparison of the magnetic force calculated by dipole–dipole model and ANSYS Maxwell: **a** 2RMNVA ($d_x = 0.022$ m), **b** 2AMNVA ($d_x = 0.022$ m), **c** 3RMNVA ($d_x = 0.024$ m, $d_y = 0.007$ m) and **d** 3AMNVA ($d_x = 0.022$ m, $d_y = 0.014$ m)

model and that from ANSYS Maxwell are not significant for the displacement range concerned. It can be also found that with the increase of y_a , the discrepancy become larger due to the assumption of small displacement and rotation used in the calculation of the magnetic force with dipole–dipole method. However, considering the amplitude of magnetic force will gradually decrease to almost zero with the increase of y_a after reaching the maximum value, the discrepancy under high y_a is not of importance.

Therefore, based on the above simulation results, the dipole–dipole model with the approximate rotation at tip is adopted for the magnetic force calculation in this paper.

References

1. Rana, R., Soong, T.T.: Parametric study and simplified design of tuned mass dampers. *Eng. Struct.* **20**(3), 193–204 (1998). [https://doi.org/10.1016/S0141-0296\(97\)00078-3](https://doi.org/10.1016/S0141-0296(97)00078-3)
2. Anubi, O.M., Crane, C.D.: A new active variable stiffness suspension system using a nonlinear energy sink-based controller. *Vehicle Syst. Dyn.* **51**(10), 1588–1602 (2013). <https://doi.org/10.1080/00423114.2013.815358>
3. Kremer, D., Liu, K.: A nonlinear energy sink with an energy harvester: transient responses. *J. Sound. Vib.* **333**(20), 4859–4880 (2014). <https://doi.org/10.1016/j.jsv.2014.05.010>
4. Frank Pai, P., Schulz, M.J.: A refined nonlinear vibration absorber. *Int. J. Mech. Sci.* **42**(3), 537–560 (2000). [https://doi.org/10.1016/S0020-7403\(98\)00135-](https://doi.org/10.1016/S0020-7403(98)00135-)
5. Zhang, Y.-W., Lu, Y.-N., Zhang, W., Teng, Y.-Y., Yang, H.-X., Yang, T.-Z., Chen, L.-Q.: Nonlinear energy sink with

- inert. Mech. Syst. Signal Pr. **125**, 52–64 (2019). <https://doi.org/10.1016/j.ymsp.2018.08.026>
6. Wang, J., Sun, S., Tang, L., Hu, G., Liang, J.: On the use of metasurface for Vortex-Induced vibration suppression or energy harvesting. *Energ. Convers. Manage.* (2021). <https://doi.org/10.1016/j.enconman.2021.113991>
 7. Lee, Y.S., Vakakis, A.F., Bergman, L.A., McFarland, D.M., Kerschen, G., Nucera, F., Tsakirtzis, S., Panagopoulos, P.N.: Passive non-linear targeted energy transfer and its applications to vibration absorption: a review. *P. I. Mech. Eng. K-J. Mul.* **222**(2), 77–134 (2008). <https://doi.org/10.1243/14644193jmbd118>
 8. Lu, Z., Wang, Z., Zhou, Y., Lu, X.: Nonlinear dissipative devices in structural vibration control: A review. *J. Sound. Vib.* **423**, 18–49 (2018). <https://doi.org/10.1016/j.jsv.2018.02.052>
 9. Huang, X., Yang, B.: Towards novel energy shunt inspired vibration suppression techniques: principles, designs and applications. *Mech. Syst. Signal Pr.* (2023). <https://doi.org/10.1016/j.ymsp.2022.109496>
 10. Silva, T.M.P., Clementino, M.A., De Marqui, C., Erturk, A.: An experimentally validated piezoelectric nonlinear energy sink for wideband vibration attenuation. *J. Sound. Vib.* **437**, 68–78 (2018). <https://doi.org/10.1016/j.jsv.2018.08.038>
 11. Yao, H., Wang, Y., Xie, L., Wen, B.: Bi-stable buckled beam nonlinear energy sink applied to rotor system. *Mech. Syst. Signal Pr.* (2020). <https://doi.org/10.1016/j.ymsp.2019.106546>
 12. Wang, J., Zhang, C., Li, H., Liu, Z.: Experimental and numerical studies of a novel track bistable nonlinear energy sink with improved energy robustness for structural response mitigation. *Eng. Struct.* (2021). <https://doi.org/10.1016/j.engstruct.2021.112184>
 13. Zou, D., Liu, G., Rao, Z., Tan, T., Zhang, W., Liao, W.-H.: A device capable of customizing nonlinear forces for vibration energy harvesting, vibration isolation, and nonlinear energy sink. *Mech. Syst. Signal Pr.* (2021). <https://doi.org/10.1016/j.ymsp.2020.107101>
 14. Dekemele, K., Habib, G., Loccufer, M.: The periodically extended stiffness nonlinear energy sink. *Mech. Syst. Signal Pr.* (2022). <https://doi.org/10.1016/j.ymsp.2021.108706>
 15. Geng, X.-F., Ding, H.: Theoretical and experimental study of an enhanced nonlinear energy sink. *Nonlinear Dynam.* **104**(4), 3269–3291 (2021). <https://doi.org/10.1007/s11071-021-06553-6>
 16. Li, S., Wu, H., Chen, J.: Global dynamics and performance of vibration reduction for a new vibro-impact bistable nonlinear energy sink. *Int. J. Nonlin. Mech.* (2022). <https://doi.org/10.1016/j.ijnonlinmec.2021.103891>
 17. Pennisi, G., Stephan, C., Gourc, E., Michon, G.: Experimental investigation and analytical description of a vibro-impact NES coupled to a single-degree-of-freedom linear oscillator harmonically forced. *Nonlinear Dynam.* **88**(3), 1769–1784 (2017). <https://doi.org/10.1007/s11071-017-3344-1>
 18. Gourc, E., Seguy, S., Michon, G., Berlioz, A., Mann, B.P.: Quenching chatter instability in turning process with a vibro-impact nonlinear energy sink. *J. Sound. Vib.* **355**, 392–406 (2015). <https://doi.org/10.1016/j.jsv.2015.06.025>
 19. Al-Shudeifat, M.A.: Asymmetric magnet-based nonlinear energy sink. *J. Comput. Nonlin. Dyn.* (2015). <https://doi.org/10.1115/1.4027462>
 20. Fang, X., Wen, J., Yin, J., Yu, D.: Highly efficient continuous bistable nonlinear energy sink composed of a cantilever beam with partial constrained layer damping. *Nonlinear Dynam.* **87**(4), 2677–2695 (2016). <https://doi.org/10.1007/s11071-016-3220-4>
 21. Chen, Y.-Y., Qian, Z.-C., Zhao, W., Chang, C.-M.: A magnetic Bi-stable nonlinear energy sink for structural seismic control. *J. Sound. Vib.* (2020). <https://doi.org/10.1016/j.jsv.2020.115233>
 22. Zhang, Y., Tang, L., Liu, K.: Piezoelectric energy harvesting with a nonlinear energy sink. *J. Intel. Mat. Syst. Str.* **28**(3), 307–322 (2016). <https://doi.org/10.1177/1045389x16642301>
 23. Rezaei, M., Talebitooti, R., Liao, W.-H.: Exploiting bistable magneto-piezoelectric absorber for simultaneous energy harvesting and vibration mitigation. *Int. J. Mech. Sci.* (2021). <https://doi.org/10.1016/j.ijmecsci.2021.106618>
 24. Rezaei, M., Talebitooti, R., Liao, W.-H.: Investigations on magnetic bistable PZT-based absorber for concurrent energy harvesting and vibration mitigation: Numerical and analytical approaches. *Energy* (2022). <https://doi.org/10.1016/j.energy.2021.122376>
 25. Rezaei, M., Talebitooti, R.: Investigating the performance of tri-stable magneto-piezoelectric absorber in simultaneous energy harvesting and vibration isolation. *Appl. Math. Model.* **102**, 661–693 (2022). <https://doi.org/10.1016/j.apm.2021.09.044>
 26. Fang, S., Chen, K., Xing, J., Zhou, S., Liao, W.-H.: Tuned bistable nonlinear energy sink for simultaneously improved vibration suppression and energy harvesting. *Int. J. Mech. Sci.* (2021). <https://doi.org/10.1016/j.ijmecsci.2021.106838>
 27. Benacchio, S., Malher, A., Boisson, J., Touzé, C.: Design of a magnetic vibration absorber with tunable stiffnesses. *Nonlinear Dynam.* **85**, 893–911 (2016). <https://doi.org/10.1007/s11071-016-2731-3>
 28. Chen, X., Leng, Y., Sun, F., Su, X., Sun, S., Xu, J.: A novel triple-magnet magnetic suspension dynamic vibration absorber. *J. Sound. Vib.* **546**, 117483 (2023). <https://doi.org/10.1016/j.jsv.2022.117483>
 29. Zhou, S., Cao, J., Wang, W., Liu, S., Lin, J.: Modeling and experimental verification of doubly nonlinear magnet-coupled piezoelectric energy harvesting from ambient vibration. *Smart Mater. Struct.* (2015). <https://doi.org/10.1088/0964-1726/24/5/055008>
 30. Xiong, L., Tang, L., Liu, K., Mace, B.R.: Broadband piezoelectric vibration energy harvesting using a nonlinear energy sink. *J. Phys. D. Appl. Phys.* (2018). <https://doi.org/10.1088/1361-6463/aab9e3>
 31. Yan, B., Yu, N., Wu, C.: A state-of-the-art review on low-frequency nonlinear vibration isolation with electromagnetic mechanisms. *Appl. Math. Mech.* **43**(7), 1045–1062 (2022). <https://doi.org/10.1007/s10483-022-2868-5>
 32. Zhang, Y., Liao, W.H., Bowen, C., Wang, W., Cao, J.: Applicability of magnetic force models for multi-stable energy harvesters. *J. Intel. Mat. Syst. Str.* (2022). <https://doi.org/10.1177/1045389X221131807>

33. Zhang, Y., Cao, J., Wang, W., Liao, W.H.: Enhanced modeling of nonlinear restoring force in multi-stable energy harvesters. *J. Sound. Vib.* **494**, 115890 (2021). <https://doi.org/10.1016/j.jsv.2020.115890>
34. Tan, D., Leng, Y.G., Gao, Y.J.: Magnetic force of piezoelectric cantilever energy harvesters with external magnetic field. *Eur. Phys. J-Spec. Top.* **224**(14–15), 2839–2853 (2015). <https://doi.org/10.1140/epjst/e2015-02592-6>
35. Yamada, K., Asami, T.: Passive vibration suppression using 2-degree-of-freedom vibration absorber consisting of a beam and piezoelectric elements. *J. Sound. Vib.* (2022). <https://doi.org/10.1016/j.jsv.2022.116997>
36. Ouled Chtiba, M., Choura, S., Nayfeh, A.H., El-Borgi, S.: Vibration confinement and energy harvesting in flexible structures using collocated absorbers and piezoelectric devices. *J. Sound. Vib.* **329**(3), 261–276 (2010). <https://doi.org/10.1016/j.jsv.2009.09.028>
37. Nili Ahmadabadi, Z., Khadem, S.E.: Nonlinear vibration control and energy harvesting of a beam using a nonlinear energy sink and a piezoelectric device. *J. Sound. Vib.* **333**(19), 4444–4457 (2014). <https://doi.org/10.1016/j.jsv.2014.04.033>
38. Fang, S., Fu, X., Liao, W.H.: Asymmetric plucking bistable energy harvester: modeling and experimental validation. *J. Sound. Vib.* **459**, 114852 (2019)

Publisher's Note Springer Nature remains neutral with regard to jurisdictional claims in published maps and institutional affiliations.